



On-line X-ray fluorescence analysis applied to industrial processes and environmental monitoring

by

Knut Ingvald Dietzel

A dissertation submitted in partial fulfilment of
the requirements for the degree of Candidatus Scientiarum.

Applied Physics and Technology Section,
Department of Physics,
The University of Bergen,
Norway

October 2000

Contents

Contents	v
Preface	vii
List of abbreviations, acronyms and symbols	ix
Abstract	xi
I Introduction and theory	1
1 Introduction	3
1.1 Motivation	3
1.2 Previous work	4
1.3 Objectives	4
2 Radiation sources and physics	7
2.1 Radiation sources	7
2.1.1 Nuclear radiation	7
2.1.2 X-ray emission (X-ray sources)	7
2.1.3 Gamma-ray sources	8
2.2 Radiation physics	8
2.2.1 Interaction of radiation with matter	8
2.2.2 Emission of characteristic X-rays	14
3 On-line X- or gamma-ray fluorescence analysis	19
3.1 Measurement principle	19
3.2 Fluorescence yield calculation	21
3.2.1 Excitation by monochromatic radiation	21
3.2.2 Excitation by polychromatic radiation	24
3.3 Limits of detection	24
3.3.1 The differential limit of detection	24
3.3.2 The absolute and practical detection limits	26

II	Experimental arrangement and measurement results	29
4	Equipment used in the experimental setup	31
4.1	Radiation detection system	31
4.1.1	Radiation detectors	32
4.1.2	Amplifiers	33
4.2	Data acquisition system	33
4.2.1	Multi channel analyzer	34
4.2.2	Software	34
4.3	Radiation sources	35
4.3.1	Radioactive isotopes	35
4.3.2	X-ray tubes	36
4.4	Shielding	41
4.4.1	Detector shielding	41
4.4.2	X-ray tube shielding	44
4.5	Samples	45
5	Gamma-ray stimulated fluorescence	47
5.1	Fluorescence yield	47
5.1.1	Experimental arrangement	47
5.1.2	Measurement results	48
5.2	Surface measurements	50
5.2.1	Source above surface	50
5.2.2	Source submerged	55
6	X-ray stimulated fluorescence	59
6.1	Experimental arrangement	59
6.2	Measurement results	59
6.2.1	Liquid host	60
6.2.2	“Gaseous” host	64
6.2.3	Voxel position within the sample	65
7	Discussion	69
7.1	Radiation sources	69
7.2	Radiation detection	70
7.3	X-ray fluorescence measurements	71
8	Conclusions	73
9	Suggestions for further work	75
	Bibliography	77

III Appendix	79
A Pictures of components in the measurement system	81
A.1 Collimators	81
A.2 Radiation shields	83
B Technical specifications	85
B.1 Scionix scintillation detector	85
B.2 eV semiconductor detector	89
B.3 eV 550 preamplifier, with eV-5093 hybrid circuit	90
C LabVIEW Virtual Instruments	93
C.1 PHA.vi	93
C.2 Initialisation.vi	109
C.3 Reset.vi	115
C.4 Region of interest.vi	119
C.5 Noise calculation.vi	123
C.6 Save data.vi	129
C.7 Load data.vi	135
C.8 Print.vi	143
C.9 Smoothing and peak search.vi	149
C.10 Save or print info.vi	153
C.11 Info string.vi	157
C.12 Info dialogue.vi	163
C.13 Elapsed time.vi	167
C.14 Acquisition.vi	171
C.15 Stop test.vi	175
C.16 Dead time.vi	181
D Radiation sources	185
D.1 ²⁴¹ Am gamma sources	185
D.1.1 Disk source	185
D.1.2 Point source	186

Preface

This work was initiated in April 1999 at the Applied Physics and Technology Section, Department of Physics, University of Bergen (UoB). The project is a joint venture between UoB and University of Manchester, Institute of Science and Technology (UMIST).

This thesis is a report on the feasibility of an on-line X-ray fluorescence system for continuous and direct analysis of industrial and environmental processes. It is organized in three parts, which contain:

- **Part I:** Chapters 1, 2 and 3, contain the introduction, underlying theory of the measurement principle and mathematical models.
- **Part II:** Chapters 4, 5, 6, 7, 8 and 9, contain design and equipment details, experiments, results, conclusions and suggestions for further work.
- **Part III:** Contains appendices.

During the nineteen months that I have spent working on this project, I have acquired new insight into the process of research and development, and received benefits from the environment around me of academic and research staff, and fellow students. I want to thank several people for their contributions:

Assoc. Prof. Geir Anton Johansen: My supervisor during this project, for giving me guidance and help through the entire project.

Prof. Hugh McCann: My external supervisor, for giving me guidance and help during my stay at UMIST. Also, for making the facilities of the Process Tomography Group available to me.

Assoc. Prof. Rune W. Time: At Stavanger College, for making the facilities of the Petroleum Technology Department available to me.

Mechanical workshops: The employees of both the mechanical workshops at UoB and UMIST deserve acknowledgement for their excellent service and workmanship.

Asbjørn Spilde: For taking time to proof read my thesis.

Fellow students, friends and family: For discussions, help and moral support.

Bergen, October 2000

Knut Ingvald Dietzel

List of abbreviations, acronyms and symbols

Table 1 List of abbreviations and acronyms.

Abbreviation	Meaning
Am	Americium
ASIC	Application Specific Integrated Circuit
Cd	Cadmium
Cs	Caesium
CT	Computer Tomography
GPIB	General Purpose Interface Bus (IEEE 488)
LabVIEW	Laboratory Virtual Instrument Engineering Workbench (© National Instruments)
MCA	Multiple Channel Analyser
NDT	Non-Destructive Testing
PHA	Pulse Height Analyser
PMT	Photo Multiplier Tube
Pb	Lead
ppm	Parts Per Million
Pt	Platinum
SI	Système International d'Unités
UMIST	University of Manchester, Institute of Science and Technology
UoB	University of Bergen
VI	Virtual Instrument
X-FAPT	X-ray Fluorescence Autoprojection Tomography

Table 2 List of symbols.

Symbol	Meaning
B	Build-up factor
C	Concentration
c	Speed of light in vacuum [m/s]
f_i	Excitation factor
h	Planck's constant
I	Intensity
j	Total quantum number
l	Angular momentum number
m	Magnetic quantum number
N	Number of counts
n	Principal quantum number or count rate
r	Absorption jump ratio
s	Spin quantum number
Z	Atomic number
κ	Pair production coefficient
λ	Wavelength
μ	Linear attenuation coefficient
μ/ρ	Mass attenuation coefficient
ν	Photon frequency
ρ	Density of the medium
σ	Compton scattering coefficient
σ_r	Rayleigh scattering coefficient
τ	Photoelectric attenuation coefficient
ω	Fluorescence yield

Abstract

X-ray stimulated fluorescence analysis is a powerful and widely used tool for determining the concentration of chemical species in materials. Presently, this is done by taking and preparing samples for off-line laboratory measurements. This project is a feasibility study of an on-line X-ray fluorescence system for continuous and direct analysis of industrial and environmental processes.

The feasibility of this measurement principle depend on the accuracy with which the concentration can be measured within a given response time. Therefore this project has been focused on investigating the fundamental properties, such as fluorescence yield, X-ray source emission spectrum and stability of X-ray source intensity.

Mathematical models to calculate X-ray fluorescence intensities and detection limits have been developed. Further, four different experimental arrangements were designed to measure absolute and relative fluorescence yield from samples with liquid and “gaseous” hosts containing a specie. In these experimental set-ups ionizing radiation from both X-ray tubes and gamma-ray sources (^{241}Am) were used. Comparison of the experimental results to the results predicted by the mathematical model were carried out where possible.

Gamma-ray stimulated fluorescence measurements were carried out in three different controlled experimental setups. Firstly, absolute fluorescence yield measurements were conducted on a liquid sample in a closed vessel. This proved not to be feasible due to intensity limitations of the ^{241}Am source, which resulted in too low intensities of fluorescent radiation to be detected. Secondly, relative fluorescence yield measurements were conducted on the surface of a liquid sample contained in an open vessel with the radioactive source above the sample surface. This also proved not to be feasible again due to intensity limitations of the ^{241}Am source, which resulted in very low intensities of fluorescent radiation. Thirdly, relative fluorescence yield measurements were conducted on the surface of a liquid sample in an open vessel with the radioactive source submerged into the sample. This resulted in detectable fluorescence peaks, but in a very limited concentration range.

Characterization of the X-ray tubes and X-ray stimulated fluorescence measurements have been investigated in a fourth experimental arrangement. The characterization of the X-ray tubes consisted of measuring stability of radiation intensity, emission spectra and total or integrated intensity. Measurements of X-ray stimulated fluorescence were performed on different specie types and concentrations in liquid and “gaseous” hosts. The results from these measurements confirm that the highest potential lies in measurements on species in a gaseous host, due to its lower density. Effects of different penetration and escape depths for incident and fluorescent

ABSTRACT

radiation were also investigated for a liquid host. The results from these measurements confirm that for an optimized system it is more important to reduce the escape depth for fluorescent radiation than the penetration depth for ionizing radiation.

The mathematical model was applied to the results from X-ray stimulated fluorescence generated in a liquid host. Calculations obtained from the two models regarding fluorescence intensities and detection limits support the trends observed in the experimental results. Though, the theoretical results underestimate the fluorescence yield and overestimates the detection limits compared to the experimental results. These deviations can be explained by examining the experimental arrangements and the uncertainties in the measured characteristics of the X-ray tube.

Part I

Introduction and theory

Chapter 1

Introduction

This thesis is a feasibility study of an on-line X-ray fluorescence system for continuous and direct analysis of industrial processes and environmental monitoring.

1.1 Motivation

The uses of X- and gamma-rays have many applications. Its application within medicine, such as radiography and computer tomography (CT), is probably the best known. X- and gamma-rays also have application within industrial processes, such as single and multiphase density meters, thickness and level gauges, non-destructive testing and industrial tomography. Also, X-ray spectroscopy is a highly versatile and accurate method of instrumental elemental quantitative analysis. Further, X-rays have application within security controls, e.g. the screening of passenger luggage for weaponry and explosives.

X- and gamma-ray systems have the advantage of not being in direct contact with a patient or intruding into an industrial process. This is an important feature with both medical and industrial instrumentation.

In industrial systems today many measurement principles are in use. None of these principles yield any information regarding the concentration of chemical species in these systems. In addition, current applications of X-ray fluorescence is based on taking samples for laboratory analysis (off-line) using cryogenic cooled detector systems. An example of an X-ray fluorescence analysis spectrum, recorded using a cryogenic cooled detector system is presented in Figure 1.1.

The motivation for this work was the prospect of being able to use room temperature radiation detectors to measure X- and gamma-ray stimulated fluorescence. Further, by analyzing the energy and intensity of the fluorescent radiation be able to determine the concentration of chemical species in industrial and environmental processes. The monitoring of metals in dilute hosts is a natural activity in environmental protection, both in aqueous and gaseous systems. Similarly, processing of food products and toiletries require careful control or rejection of unwanted metals.

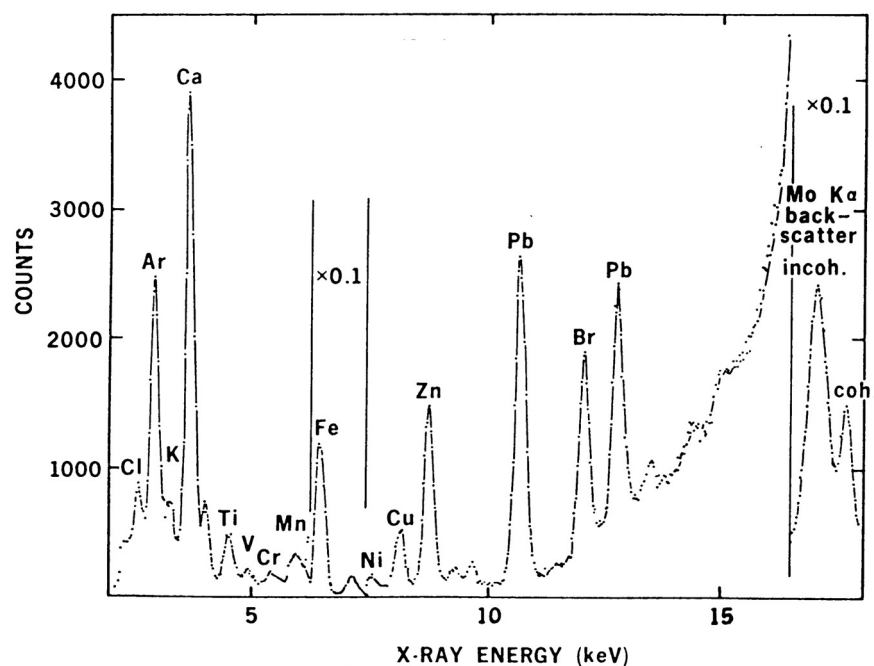


Figure 1.1 Typical X-ray fluorescence analysis spectrum of aerosols. Recorded using a cryogenic cooled detector system [1].

1.2 Previous work

A preliminary study on X-ray Fluorescence Autoprojection Tomography (X-FAPT) has been carried out as a co-operation between the University of Manchester, Institute of Science and Technology (UMIST) and the University of Bergen (UoB) [2].

The conclusion of this study reveals that there is a considerable interest for a non-tomographic on-line instrument for X-ray fluorescence analysis. It also points out the most critical factors for the non-tomographic instrument:

- Vessel type and size.
- Host type (e.g. liquid or gas).
- Element(s) to detect.

Such an instrument can also be used on processes where there is open access to the process, such as the surface of an open flow or the surface of a liquid in a vessel.

1.3 Objectives

Feasibility of this measurement principle depends on the accuracy with which the concentration can be determined within a given response time. Therefore the project has been focused on investigating the following fundamental properties:

- Absolute fluorescence yield.
- Relative fluorescence yield.
- X-ray source intensity and stability.
- X-ray source emission spectrum.

The fluorescence yield have been investigated in controlled set-ups with one specie in a liquid or “gaseous” host.

Chapter 2

Radiation sources and physics

In order to understand the measurement principle which is studied in this thesis, it is necessary to have some knowledge of X- and gamma-ray sources and interaction mechanisms between radiation and matter.

2.1 Radiation sources

2.1.1 Nuclear radiation

Radioactive decay is a spontaneous change within the nucleus of an atom, which results in the emission of particles or electromagnetic waves. Radioactive elements may disintegrate through three principal modes: alpha, beta and gamma decay. In *alpha decay* a ${}^4_2\text{He}^{2+}$ nucleus, which is called *α-particle*, is emitted from the nucleus. Second, when neutrons in the nucleus are changing to protons, or protons are changing to neutrons the nucleus emits electrons or positrons respectively. These decay modes are called *beta-minus* (β^-) and *beta-plus decay* (β^+) correspondingly. The third decay process is *electron capture*, in which an orbital electron of the atom is captured by the nucleus. In doing so changes a proton to a neutron and the loss of an electron from one of the orbital shells leaves a vacancy there. An electron dropping in from a higher less tightly bound shell fills this vacancy. The energy released in this process often appears as an *X-ray*.

2.1.2 X-ray emission (X-ray sources)

X-rays, which were discovered by Wilhelm Conrad von Roentgen in 1895, are produced when high-energy particles, e.g. electrons, are decelerated in the field of the atom's electrons or nucleus. These are called *Bremsstrahlung* and *characteristic X-rays* respectively. The energy spectrum of Bremsstrahlung X-rays is continuous, ranging from zero and up to the particles initial energies. Discrete energy X-rays are produced when excited electrons de-excite, their energies are characteristic of the energy levels of the atomic electrons, see Subsection 2.2.2. The characteristic X-ray lines are superimposed on the continuous Bremsstrahlung X-ray spectrum.

2.1.3 Gamma-ray sources

Gamma-rays can originate from different processes:

1. Gamma-rays following alpha, beta decay or electron capture.
2. Gamma-rays following nuclear reactions.

In case 1 the gamma radiation is emitted by an excited nuclei when it returns to a lower-lying nuclear level. De-excitation takes place through emission of a gamma-ray photon whose energy essentially is equal to the difference in energy between the two nuclear states. In case 2 a nuclear reaction leaves the product nucleus in an excited state. Its decay gives rise to a gamma-ray photon, with higher energy than those available from beta-active isotopes.

In addition an indirect result of 1 or 2 appears when the nucleus undergoes β^+ -decay. Positrons generally only travel a few millimeters before losing their kinetic energy. Near the end of their range, they combine with negative electrons in the absorbing material through the process of annihilation. The original positron and electron disappear and are replaced by two oppositely directed 511 keV photons. These photons are not gamma-rays because they do not originate from the nucleus.

2.2 Radiation physics

2.2.1 Interaction of radiation with matter

The attenuation coefficient and the build-up factor

When a beam of monoenergetic photons of energy E_0 and intensity I_0 penetrates a homogeneous material, a number of photons will be removed from the beam through interactions within the sample. The intensity of the emerging beam is given by

$$\frac{dI}{dx} = -\mu I \Rightarrow \int_{I_0}^I \frac{dI}{I} = -\mu dx \Rightarrow I = I_0 e^{-\mu x} \quad (2.1)$$

where μ [cm^{-1}] is the *linear attenuation coefficient* of the material. It is sometimes more convenient to define the mass attenuation coefficient μ/ρ [cm^2/g] which is independent on the density of the material. The linear attenuation coefficient express the photon interaction probability per unit path length, and the mass attenuation coefficient is related to the probability that radiation will interact with matter. The latter probability is a measure of the atomic area involved in the interaction.

The linear and mass attenuation coefficients are the sum of the respective attenuation coefficients for each mode of interaction, i.e. the *photoelectric effect*, *Compton scattering*, *Rayleigh scattering* and *pair production*.

The relationship in Equation 2.1 is only valid under “good geometry” conditions meaning a thin absorber and collimated detector and gamma- or X-ray source, ref. Figure 2.1.

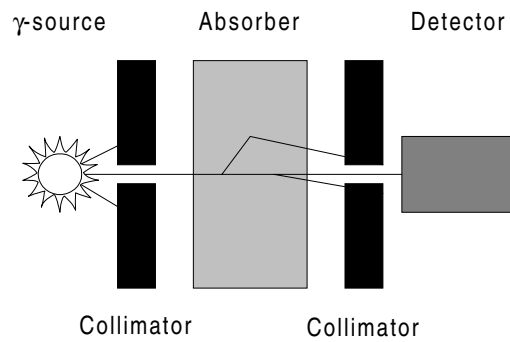


Figure 2.1 Attenuation of a beam of gamma-rays. The “good geometry” conditions contribute to reduce build-up [3].

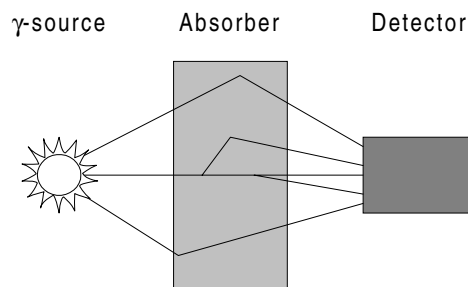


Figure 2.2 Attenuation of a beam of gamma-rays. The open geometry conditions gives rise to build-up [3].

Otherwise scattered radiation will affect on the measurement of the linear attenuation coefficient, as illustrated in Figure 2.2.

The practical influence of scattered radiation, also referred to as build-up, can be accounted for with a correction to Equation 2.1

$$I = I_0 B e^{-\mu x} \quad (2.2)$$

where B is the ratio of the total photons at a point to the number arriving there without being scattered. Under “good geometry” conditions the build-up factor, B , is unity.

The photoelectric effect

In this absorption process, an incident photon undergoes an interaction with one of the electrons of an atom in which the photon completely disappears. As a result the electron is ejected from its shell and the atom, which is left in an excited state, will shortly after return to a stable state through one of two possible mechanisms: *fluorescence* or *Auger effect*. In the first effect a characteristic X-ray is emitted when an outer electron, in shell i , takes the empty place left by the ejected electron in shell j . The ejected electron will have a kinetic energy of

$$E_{kin} = E_\gamma - E_{bj} \quad (2.3)$$

where E_γ is the energy of the incident photon and E_{bj} is the binding energy of the j^{th} shell. In the case of fluorescence the X-ray photon will have energy of

$$E_X = E_{bj} - E_{bi} \quad (2.4)$$

where E_{bi} is the binding energy of the i^{th} shell. The probability of fluorescence to occur is expressed by the *fluorescence yield*.

The photoelectric attenuation coefficient, τ , is dependent on both the Z -number of the absorber and energy of the gamma- or X-rays. A rough approximation is

$$\tau = C \frac{Z^n}{E_\gamma^{3.5}} \quad (2.5)$$

where C is a constant, E_γ the energy of the interacting photon, Z the atomic number of the absorber and n varies between 4 and 5 over the energy region of interest [4]. Photoelectric absorption is the dominant mode of interaction for gamma or X-rays of relatively low energies, and the process is also enhanced for absorber material of high atomic number Z . A plot of the energy dependence of the photoelectric linear coefficient is shown in Figure 2.3.

Compton scattering

The Compton scattering process takes place between the incident gamma-ray photon and an electron of an atom in the absorber. In this interaction mechanism the incident photon is deflected through an angle, θ , with respect to its original direction. Part of the photon’s energy is transferred to the electron which is ejected from the atom at an angle, ϕ . Compton scattering is an

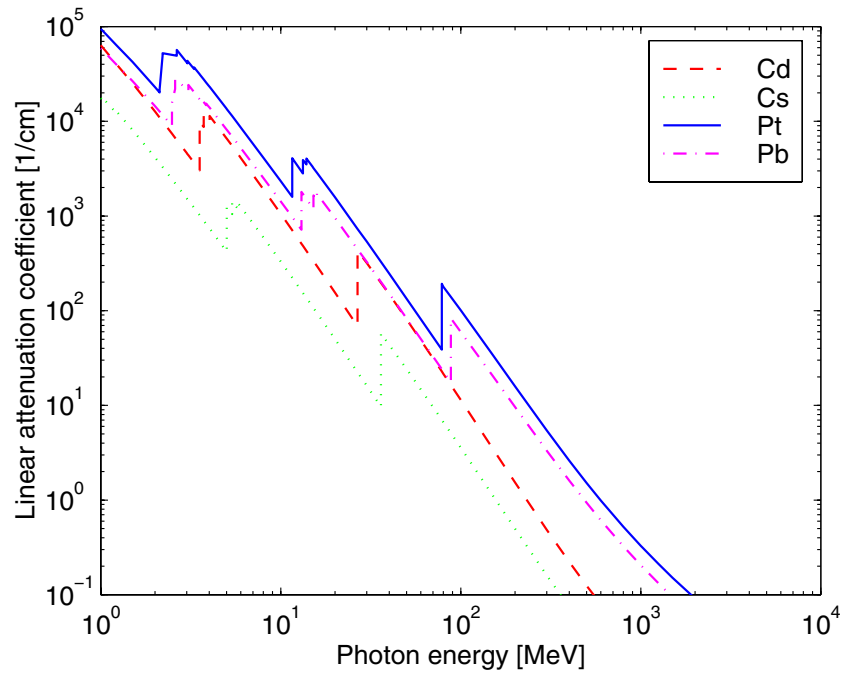


Figure 2.3 Energy dependence of the Photoelectric attenuation coefficient, τ , in cadmium ($Z = 48$), caesium ($Z = 55$), platinum ($Z = 78$) and lead ($Z = 82$). The data is taken from the program PhotCoef [5].

inelastic (in-coherent) process, the photon must overcome the electron to atom binding energy which is a criteria for the electron to be ejected. The ejected electron is referred to as the *recoil electron*. The process is shown schematically in Figure 2.4.

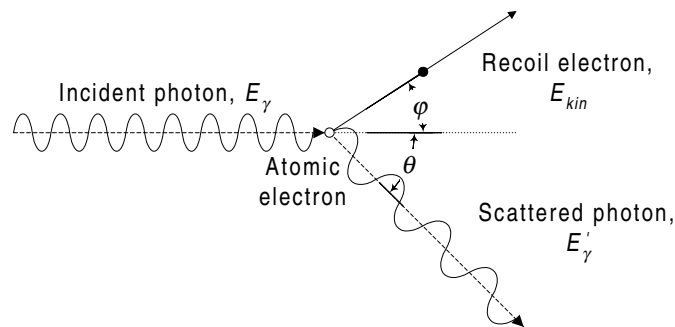


Figure 2.4 The Compton scattering process [3].

An expression relating the energy transfer and scattering angles can be derived using the conservation of energy principle, and the assumption that the electron's binding energy is negligible

$$E'_\gamma = \frac{E_\gamma}{1 + \frac{E_\gamma}{m_e c^2} (1 - \cos\theta)} \quad (2.6)$$

where $m_e c^2$ is the rest-mass of the electron (511 keV) [4]. The kinetic energy of the electron is then given as

$$E_{kin} = E_\gamma - E'_\gamma = \frac{E_\gamma}{1 + \frac{m_e c^2}{E_\gamma(1 - \cos\theta)}} \quad (2.7)$$

The probability of Compton scattering, σ , is roughly proportional to the atomic number Z and the inverse of the photon energy

$$\sigma = C \frac{Z}{A} \rho \frac{1}{E_\gamma} \quad (2.8)$$

where C is a constant and ρ the density of the material. The angular distribution of scattered gamma-rays can be predicted by the *Klein-Nishina formula* for the differential scattering cross section $d\sigma/d\Omega$

$$\frac{d\sigma}{d\Omega} = Z r_0^2 \left(\frac{1}{1 + \alpha(1 - \cos\theta)} \right)^2 \left(\frac{1 + \cos^2\theta}{2} \right) \left(1 + \frac{\alpha^2(1 - \cos\theta)^2}{(1 + \cos^2\theta)[1 + \alpha(1 - \cos\theta)]} \right) \quad (2.9)$$

where $\alpha \equiv h\nu/m_e c^2$ and r_0 is the classical electron radius. The distribution is illustrated graphically in Figure 2.5.

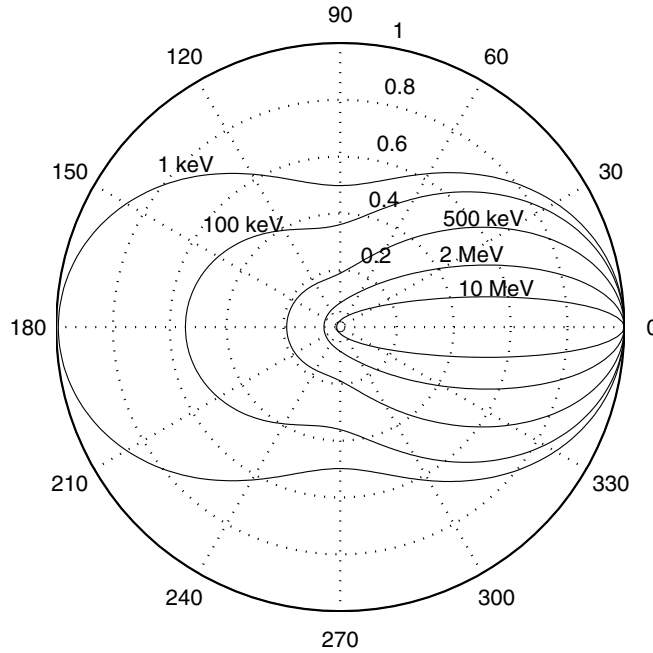


Figure 2.5 Polar plot of the angular distribution of Compton scattering, for different initial energies as indicated. The photons are incident from the left, i.e. 180° .

From the figure the strong tendency of forward scattering at high values of the gamma-ray energy is evident.

Rayleigh scattering

Gamma radiation can also interact by Rayleigh scattering, which is an elastic scattering process. In this process there is only a negligible energy transfer between the photon and the electron with which it interacts. The electron will not leave its shell and therefore the atom is not excited or ionized. Rayleigh scattering therefore involves a re-emission of the gamma-ray after absorption with a negligible change in energy, but different direction. The energy dependence of the Rayleigh interaction coefficient, σ_r , is roughly proportional to the square of the atomic Z -number.

Pair production

Unlike photoelectric absorption, Compton and Rayleigh scattering pair production is a nuclear interaction process. The incident photon interacts with the nucleus of the atom and an electron-positron pair is created. In order to create the electron-positron pair the gamma-ray must have an energy exceeding twice the rest-mass energy of an electron, $2m_e c^2 = 1,022$ keV. The excess energy of the gamma-ray are shared equally as kinetic energy between the electron and the positron

$$E_\gamma = E_{kin}^- + E_{kin}^+ + 2m_e c^2 \quad (2.10)$$

When the energy of the positron is reduced to near thermal energies it will interact with an atomic electron, releasing two 511 keV annihilation photons with opposite directions. This radiation is referred to as *annihilation radiation*.

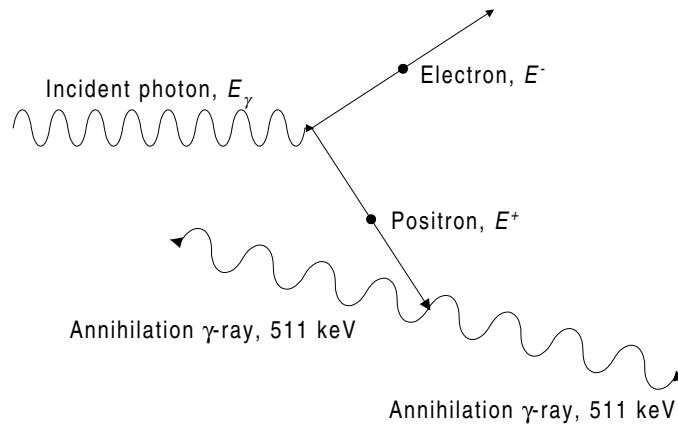


Figure 2.6 The mechanism of pair production [3].

The pair production coefficient, κ , is roughly proportional to the square of the atomic Z -number and the natural logarithm of the photon energy.

Total attenuation coefficient

The total attenuation coefficient is the sum of all the interaction coefficients discussed. At lower energies the photoelectric effect is dominant, Compton scattering at medium energies and pair

production at the highest energies, see Figure 2.7.

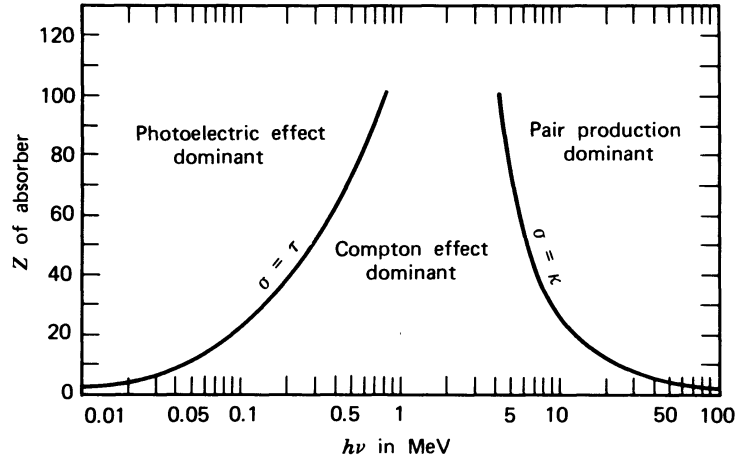


Figure 2.7 Relative importance of the three major interaction types concerning gamma radiation. Solid lines show the boundary where the two neighbouring effects are equal [6].

The contribution from Rayleigh scattering is often neglected because it is negligible compared to the photoelectric effect at lower energies, and Compton scattering at higher energies, see Figure 2.8.

Contribution from one of the attenuation mechanisms to the total attenuation is given by

$$I_{\chi} = \frac{\chi}{\mu} I_0 B e^{-\mu x} \quad (2.11)$$

where χ is one of the attenuation coefficients.

The linear attenuation coefficient of homogeneous mixtures

The total attenuation coefficient of a homogeneous mixture can be estimated as

$$\mu_{mix} = \alpha_1 \mu_1 + \alpha_2 \mu_2 + \dots + \alpha_n \mu_n = \sum_{i=1}^n \alpha_i \mu_i \quad (2.12)$$

when the volume fractions, α_i , and the attenuation coefficients, μ_i , of the different components in the mixture are known.

2.2.2 Emission of characteristic X-rays

In an interaction between a sufficiently energetic X-ray and the electrons of an atom, several phenomena can take place, as discussed in Section 2.2.1. The photoelectric effect involves the transfer of the photon energy to an atomic electron, resulting in its ejection from the atom. The ionized atom's distribution of electrons is then out of equilibrium. By transitions of electrons

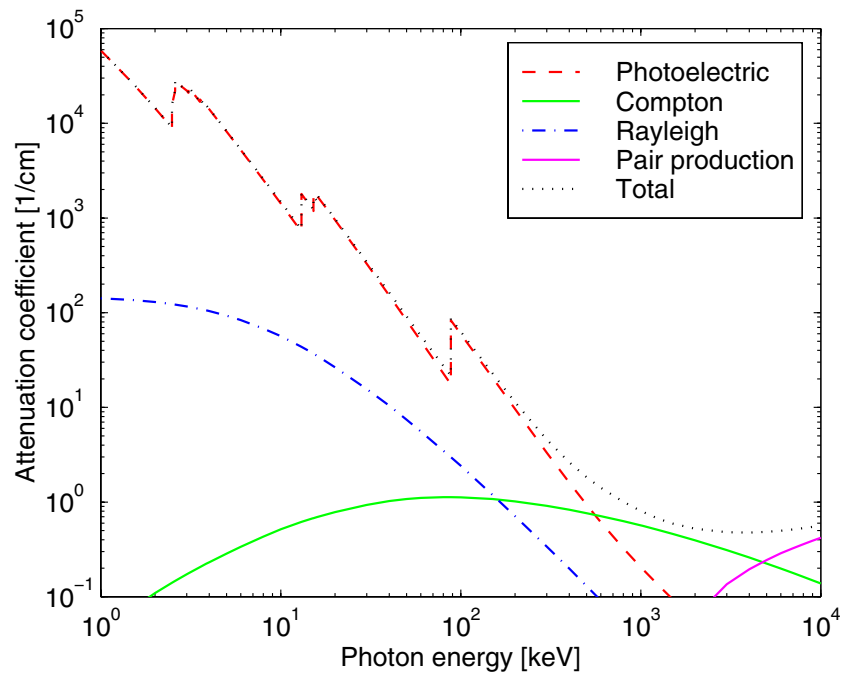


Figure 2.8 Total and individual linear attenuation coefficients for lead ($Z = 82$). The data is taken from the program PhotCoef [5].

from outer shells to inner shells the atom will return to the normal state. In such electron transitions the loss of potential energy of the atom reappears as a photon. The emitted radiation follows a number of rules that can be explained by referring to the atomic structure theory.

Electronic states

A highly simplified schematic representation of the atom is presented in Figure 2.9.

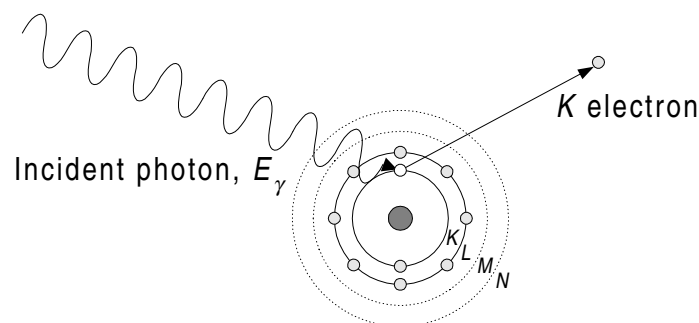


Figure 2.9 Simplified illustration of ionization of the K -shell by an incident X-ray photon [7].

The number of electrons and energy levels assigned to each shell are governed by quantum theory. Outlines of this theory state that every electron in an atom moves on an orbital that is

characterized four quantum numbers.

Table 2.1 The principal quantum numbers [7].

Symbol	Meaning
n	the principal quantum number, is associated with successive orbitals; n is a positive integer 1, 2, 3, ... that designate the $K, L, M, N,$ shells respectively.
l	the angular momentum number, is a measure of the orbital angular moment, which account for the existence of circular ($l = 0$) and elliptic orbitals; l can take all the integer values between 0 and $(n - 1)$.
m	the magnetic quantum number, can take all the integer values between $-l$ and $+l$.
s	the spin quantum number, can take only two possible values $+1/2$ and $-1/2$.

The array of all the possible electronic states is obtained by considering all possible combinations of the quantum numbers. Furthermore, there is a restriction that there can only be one electron with a given state in any given atom, this is the “Pauli principle”. Different electronic states are usually designated by symbols containing a number and a letter, see Table 2.1. The number designates the principle quantum number n while the letters s, p, d, f and g represent the angular momentum values 0, 1, 2, 3 and 4 respectively. Further, upper index after the number indicates the number of electrons that have these two quantum numbers. Thus the symbol $3d^6$ means that there are six electrons with $n = 3$ and $l = 2$. These electrons differ between each other by the values of the two other quantum numbers m and s .

Different electrons within the same shell do not all have exactly the same energy. Their energy is also dependent on a fifth quantum number j , the total quantum number. The total quantum number represents the total angular moment (angular plus spin)

$$j = l \pm 1/2 \quad (2.13)$$

with the restriction that it cannot be negative.

Critical excitation energies

To eject an electron from an atom, the incident photon must overcome the binding energy, E_b , between the nucleus and the electron. Therefore the incident photon must have energy equal to or larger than E_b .

$$E_\gamma = h\nu \geq E_b \quad (2.14)$$

where h is Planck’s constant and ν is the photon frequency. The relation between energy and wavelength is given by

$$\lambda = \frac{c}{\nu} = \frac{hc}{E} = \frac{12.398}{E} \quad (2.15)$$

where λ is in Å units and E is in keV.

Characteristic lines and selection rules

The quantum mechanical criteria described in the previous paragraph governs electron configuration of atoms. In addition quantum mechanics impose further restrictions when it comes to transfer of electrons from higher to lower energy levels. Any transition must obey the following *selection rules*

$$\begin{aligned} \Delta n &\geq 1 \\ \Delta l &= \pm 1 \\ \Delta j &= \pm 1 \text{ or } 0 \end{aligned} \quad (2.16)$$

The transitions that are “allowed” by the selection rules are shown in Figure 2.10 which contains the main lines in the K and L spectra.

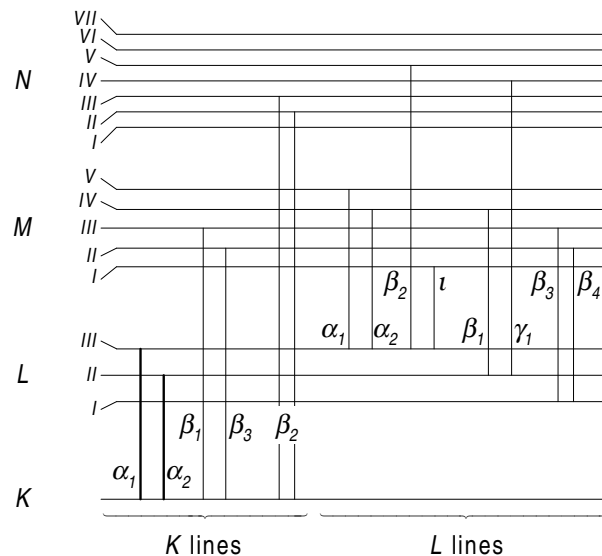


Figure 2.10 Energy level diagram of the main lines in the K and L spectra [7].

Occasionally the last two rules are not obeyed and “forbidden” transitions can be observed.

The various lines are named by a capital letter indicating the final level of the transition involved. Alternatively, each line can be differentiated, after Siegbahn by adding a Greek letter and a subscript after the capital letter. Subscripts usually reflect the relative intensities of the lines, α_1 being the strongest line in a given spectrum. It is preferable to describe a line by the final and initial level of electron transition, for example KL_{III} .

Fluorescence yield and line intensities

The fluorescence of an atomic shell or sub shell is defined as the probability that a characteristic X-ray is emitted when one of the outer electrons fills the vacancy in an inner shell. It is defined as

$$\omega = \frac{n_f}{n} \quad (2.17)$$

where n is either the number of primary photons that have induced the ionization in a given level or the number of secondary photons that are subsequently emitted, n_f is the number of these secondary photons that effectively leave the atom. The difference $n - n_f$ is the number of secondary photons that are absorbed within the atom on their way out (the *Auger effect*).

Chapter 3

On-line X- or gamma-ray fluorescence analysis

Chapter 2 covered the physical concepts needed in order to calculate theoretical fluorescence intensity. In this chapter mathematical models related to experimental setup and parameters will be derived.

3.1 Measurement principle

The probability of photoelectric attenuation of X-rays in matter is given by the photoelectric attenuation coefficient, τ . The fluorescence yield, ω_a , expresses the probability of fluorescence to occur. Two properties of the fluorescent X-rays are that their energy is characteristic and the intensity is related to the concentration. By analysing the characteristic X-ray emanating from irradiated matter a chemical sensitivity is obtained. Figure 3.1 illustrates how the average K -edge X-ray fluorescence energy, E_K , and the fluorescence yield increase with the atomic number Z . The plot also demonstrates how the photoelectric mass attenuation coefficient, $(\tau/\rho)_K$ at the K -edge energy drops off as Z increase.

The probability to get a fluorescence X-ray at any emission angle is expressed by the product $\omega_a(\tau/\rho)_K$. This product has its maximum around elements with atomic number just below 20. Regrettably, the X-ray fluorescence energy is only about 10 keV in this region. This presents a disadvantage, low energy photons are more likely to be attenuated and absorbed in the vessel and vessel walls before they reach the radiation detector. The atomic number of the main constituent in the vessel and vessel walls and the dimension of these will govern the degree of attenuation. In order to maximize the measurement system's speed of response and sensitivity to chemical elements, the following criteria are important factors for the system's performance:

- Low attenuation of the stimulation radiation in the vessel wall and host material.
- High photoelectric attenuation coefficient by the element in interest in order to engage as many as possible of the element atoms in the attenuation process.

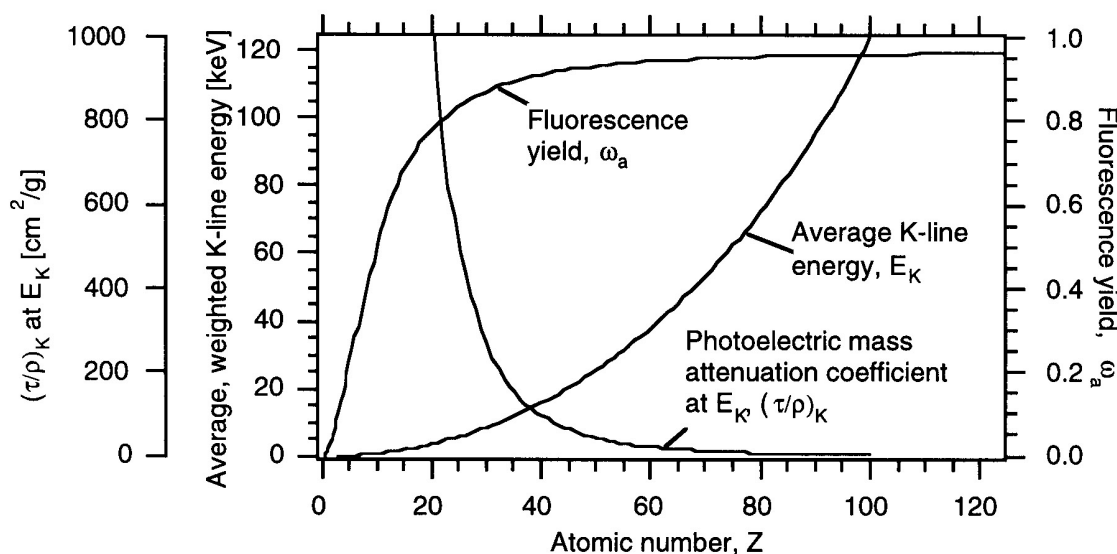


Figure 3.1 The photoelectric mass attenuation coefficient just above the elements' K -shell energy plotted versus the atomic number of the elements. Also shown are the average K -shell energy and the fluorescence yield of the elements [2].

- Fluorescence yield close to unity to optimize the number of characteristic X-rays that escape the atom.
- Low attenuation of the fluorescent radiation in the vessel wall and host material.

The ideal application would be detection of heavy elements in a light element host. For instance metal particles in gas, give low attenuation of both the stimulating and fluorescent radiation. In addition heavy elements generate fluorescent radiation with higher energy, which is less attenuated. The vessel wall should be made as thin as possible and have small linear attenuation coefficient.

The measurement principle is based on the detection of fluorescent X-rays emitted by a sample containing medium or high Z -number species. A collimated radiation source with high intensity is used to irradiate a volume element (voxel). Three different modes of the same measurement principle have been studied in this work, in order to obtain more information on the following properties:

- Absolute fluorescence yield.
- Relative fluorescence yield.
- Surface measurement.

3.2 Fluorescence yield calculation

Intensities calculated in this section are net intensities, free from influences such as background, overlap etc. Let us consider the characteristic radiation of an element i in an homogeneous sample with concentration C_i . The measurement principle is apparent from Figure 3.2. Its main components are an X- or gamma-ray source and a radiation detector, which are placed perpendicular to each other. Both the source and the detector are collimated and define a stimulation and detection line. The intersection point of the lines specify a small volume element, voxel. A fraction of the interactions by the stimulating radiation will be viewed by the detector. The sample may also be separated from the radiation source and detector by a vessel wall, and corrections to both the intensities of incident and fluorescent radiation are required.

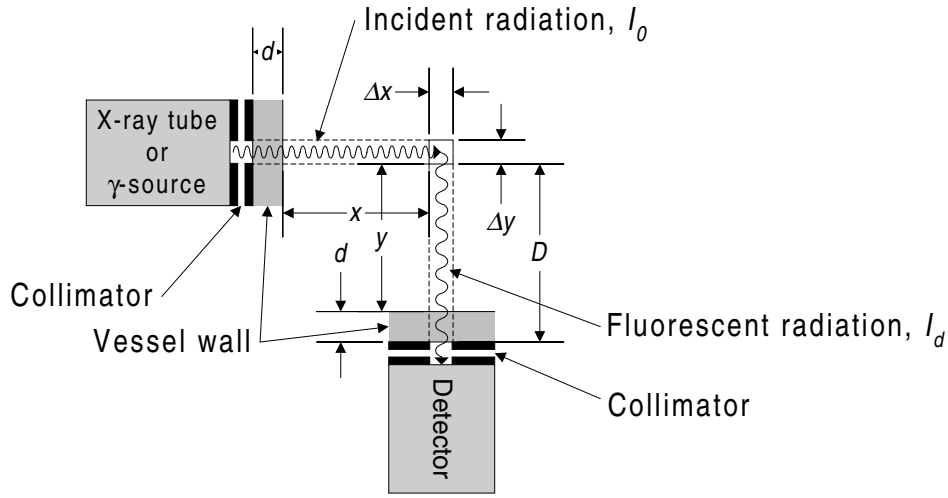


Figure 3.2 Components in the calculation of fluorescence.

In the following sections the absorption of radiation by the specie present in the sample will be ignored, under the assumption of low concentration.

3.2.1 Excitation by monochromatic radiation

The incident radiation is attenuated over the path length x , before reaching the voxel. Expressed by a ,

$$a = e^{-\mu_h(E_i)\rho_h x} \quad (3.1)$$

where $\mu_h(E_i)$ is the mass absorption coefficient of the host at energy E_i . The attenuation of incident and fluorescent radiation in the vessel walls is considered later in this section.

The fraction of the radiation that is absorbed in the volume element is

$$\left(1 - e^{-\mu_h(E_i)\rho_h \Delta x}\right) \quad (3.2)$$

Table 3.1 Definition of symbols used in intensity calculations.

Symbol	Meaning
D	Distance from voxel to detector collimator
d	Vessel wall thickness
E_f	Energy of fluorescent radiation
E_i	Energy of incident radiation
f_i	Excitation factor
$g_{K\alpha}$	Probability of $K\alpha$ emission in preference to other K lines
I_0	Intensity of radiation source
I_d	Intensity of fluorescent radiation that reach the detector
J_K	Absorption jump factor
r_k	Absorption jump
x	Path length incident radiation
y	Path length fluorescent radiation
Δx	Length of voxel in direction towards the radiation source
Δy	Length of voxel in direction towards the detector
ρ	Density
$\mu_h(E)$	Mass absorption coefficient of the host at energy E
$\mu_i(E)$	Mass absorption coefficient of the specie at energy E
Ω	Solid angle
ω_K	Fluorescence yield

where Δx is the length of the voxel along the stimulation beam. However, only the fraction

$$C_i \frac{\mu_i(E_i)}{\mu_h(E_i)} \quad (3.3)$$

is absorbed by the fluorescent element of mass coefficient $\mu_i(E_i)$, ref. Equation 2.12. Thus, the fractional absorption of element i in the voxel is represented by b ,

$$b = C_i \frac{\mu_i(E_i)}{\mu_h(E_i)} \left(1 - e^{-\mu_h(E_i)\rho_h\Delta x} \right) \quad (3.4)$$

The $K\alpha$ fluorescence emission is obtained by multiplying the number of absorbed photons by the excitation factor f_i

$$f_i = J_K \omega_K g_{K\alpha} \quad (3.5)$$

which is the product of three probabilities:

- J_K : *absorption jump factor*, fraction of the absorbed intensity by element i which leads to K ionization,

$$J_K = \frac{r_K - 1}{r_K} = \frac{\tau_K}{\tau_K + \tau_{L_I} + \tau_{L_{II}} + \tau_{L_{III}} + \dots} \quad (3.6)$$

where r_K is the *absorption jump* and τ_x is the photoelectric absorption coefficient for the different levels [7].

- $g_{K\alpha}$: probability of emission of a $K\alpha$ line in preference to other K lines.
- ω_K : fluorescence yield.

Relative attenuation by the host medium of the fluorescent radiation within the voxel can be represented by c

$$c = \int_0^{\Delta y} e^{-\mu_h(E_f)y} dy = \frac{1}{\mu_h(E_f)} \left(1 - e^{-\mu_h(E_f)\Delta y} \right) \quad (3.7)$$

where Δy is the length of the voxel viewed in direction towards the detector.

The fluorescent radiation, I_f , is emitted isotropically, and the fraction that enters the detector is defined by the solid angle subtended by the detector collimator at the voxel as a fraction of 4π . When the distance from the voxel to the detector is much larger than any of the linear dimensions of the detector collimator, the following approximation for the solid angle can be used

$$\Omega = \frac{A_{det}}{4\pi D^2} \quad (3.8)$$

where A_{det} is the area of the detector and D is the distance from voxel to detector [8].

Relative attenuation by the host medium of the fluorescent radiation leaving the voxel can be calculated as

$$h = e^{-\mu_h(E_f)\rho_h y} \quad (3.9)$$

where y is the path length in the host material, $\mu_h(E_f)$ is the mass absorption coefficient of the host at energy E_f .

The total characteristic intensity of element i is then given by

$$I_0 = e^{-\mu_h(E_i)\rho_h x} C_i \frac{\mu_i(E_i)}{\mu_h(E_i)} \left(1 - e^{-\mu_h(E_i)\rho_h \Delta x} \right) \frac{r_K - 1}{r_K} g_{K\alpha} \omega_K \frac{1}{\mu_h(E_f)} \left(1 - e^{-\mu_h(E_f)y} \right) \frac{A_{det}}{4\pi D^2} e^{-\mu_h(E_f)\rho_h y} \quad (3.10)$$

In the case where the sample is confined within a vessel; a correction of both I_0 and I_f is necessary. These corrections can be calculated by

$$F_{w,I_0} = e^{-\mu_w(E_i)\rho_w d} \quad (3.11)$$

and

$$F_{w,I_f} = e^{-\mu_w(E_f)\rho_w d} \quad (3.12)$$

where ρ_w refers to the density of the wall and μ_{w,E_i} and μ_{w,E_f} refer to the mass absorption coefficients of the wall for stimulating and fluorescent radiation, respectively.

The intensity of the fluorescent radiation reaching the detector is the product of the factors in the above equations

$$I_d = I_0 e^{-\mu_w(E_i)\rho_w d} e^{-\mu_h(E_i)\rho_h x} C_i \frac{\mu_i(E_i)}{\mu_h(E_i)} \left(1 - e^{-\mu_h(E_i)\rho_h \Delta x}\right) \frac{r_K - 1}{r_K} g_{K\alpha} \omega_K \frac{1}{\mu_h(E_f)} \left(1 - e^{-\mu_h(E_f)\Delta y}\right) \frac{A_{det}}{4\pi D^2} e^{-\mu_h(E_f)\rho_h y} e^{-\mu_w(E_f)\rho_w d} \quad (3.13)$$

3.2.2 Excitation by polychromatic radiation

When the sample is irradiated with polychromatic radiation it is necessary to consider all of the primary energies in the useful range. That is from the binding energy of the electron, E_b , to the high energy of limit of the spectral distribution of the incident radiation E_{max} .

$$I_d = C_i \frac{r_K - 1}{r_K} g_{K\alpha} \omega_K \frac{1}{\mu_h(E_f)} \left(1 - e^{-\mu_h(E_f)\Delta y}\right) \frac{A_{det}}{4\pi D^2} e^{-\mu_h(E_f)\rho_h y} e^{-\mu_w(E_f)\rho_w d} \int_{E_b}^{E_{max}} I_0(E_i) e^{-\mu_w(E_i)\rho_w d} e^{-\mu_h(E_i)\rho_h x} \frac{\mu_i(E_i)}{\mu_h(E_i)} \left(1 - e^{-\mu_h(E_i)\rho_h \Delta x}\right) dE_i \quad (3.14)$$

Equation 3.14 requires knowledge of the spectral intensity distribution of the radiation emanating from the radiation source.

3.3 Limits of detection

This section is based on the treatment in [7, pages 349–353]. Two different cases must be considered depending on the concentration of the specimen:

- The *differential* limit of detection
- The *absolute* limit of detection

The differential limit of detection applies to concentrations C and $C \pm \Delta C$, and absolute and practical detection limits applies to concentrations 0 and $0 + \Delta C$

3.3.1 The differential limit of detection

Given a calibration line, ref. Figure 3.3, for a specimen with concentration C_1 of an element. The concentration need not be small. Then, consider a second specimen similar to the first, but with a slightly different concentration, say

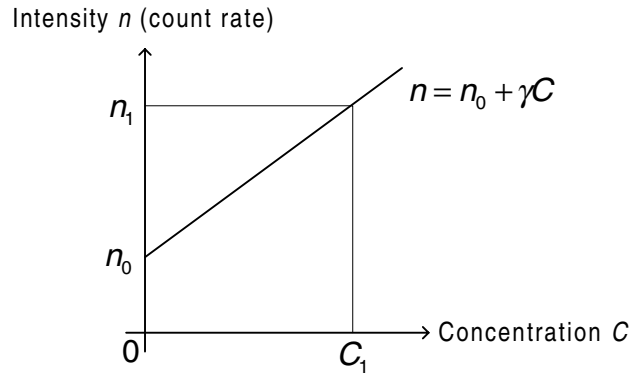


Figure 3.3 Calibration line [7].

$$C_2 = C_1(1 + e) \quad \text{with } e > 0 \quad (3.15)$$

By measuring the X-ray intensities for C_1 and C_2 several times for an interval t , reliable average values for the number of counts, \bar{N}_1 and \bar{N}_2 , can be obtained with $\bar{N}_2 > \bar{N}_1$. If only one measurement is made for each concentration there is a probability that N_1 can be measured to be greater than N_2 . By requiring the criteria

$$\bar{N}_2 - \bar{N}_1 \geq 4\sigma_1 \quad (3.16)$$

to be met, the risk of measuring $N_1 > N_2$ is practically eliminated, ref. Figure 3.4.

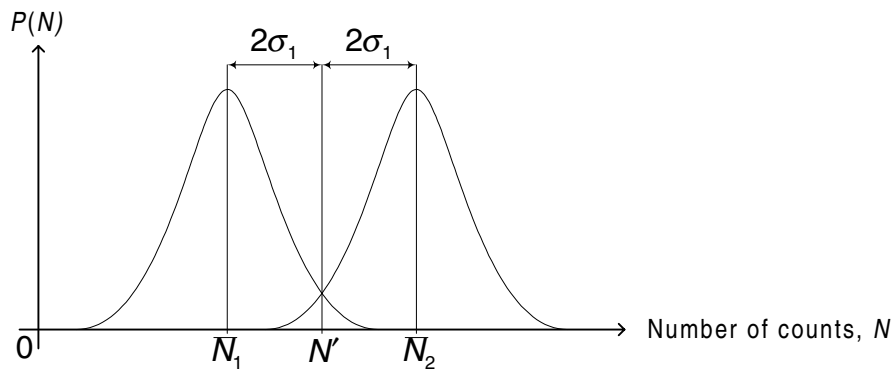


Figure 3.4 Defining the differential detection limit [7].

The slope of the calibration line in Figure 3.3 is

$$\gamma = \frac{n_1 - n_0}{C_1} \quad (3.17)$$

\bar{N} is defined as

$$\bar{N} = nt \quad (3.18)$$

Rearranging Equation 3.17 for n and inserting into Equation 3.18 yields

$$\begin{aligned}\bar{N}_1 &= n_1 t = (n_0 + \gamma C_1) t \\ \bar{N}_2 &= n_2 t = [n_0 + \gamma C_1 (1 + e)] t \\ \bar{N}_2 - \bar{N}_1 &= \gamma C_1 e t\end{aligned}\quad (3.19)$$

Provided that the assumed probability distribution function is Gaussian, the standard deviation is

$$\sigma_1 = \sqrt{\bar{N}_1} = \sqrt{n_1 t} \quad (3.20)$$

Substituting Equation 3.17 into Equation 3.19 and Equation 3.19 and 3.20 into Equation 3.16 gives the following relation

$$e \geq \frac{4}{\sqrt{t}} \cdot \frac{\sqrt{n_1}}{n_1 - n_0} \quad (3.21)$$

where the minimum value of e sets the differential detection limit. For lower values of e yields better possibility of distinguishing between to close concentrations. The value of e improves, i.e. decreases, for steeper slope of the calibration curve, γ , lower background value, n_0 , and increased integration time, t .

3.3.2 The absolute and practical detection limits

An expression for the absolute limit of detection, for very low concentrations can be derived from the equations derived in Section 3.3.1. The following expression is obtained by combining Equations 3.17 and 3.21

$$e C_1 \geq \frac{4}{\sqrt{t}} \cdot \frac{\sqrt{n_1}}{\gamma} \quad (3.22)$$

For low concentrations the slope, γ , can be obtained from a standard, s , with known concentration, C_s , where

$$n_s = n_0 + \gamma C_s \quad (3.23)$$

which gives

$$e C_1 \geq \frac{4}{\sqrt{t}} C_s \frac{\sqrt{n_1}}{n_s - n_0} \quad (3.24)$$

If the absolute limit of detection, C_L , is defined as the concentration where the measurement error is 100%, which corresponds to e equal to unity, then

$$C_L = C_s \frac{4}{\sqrt{t}} \cdot \frac{\sqrt{n_0}}{n_s - n_0} \quad (3.25)$$

or expressed in counts instead of count rate

$$C_L = 4 \cdot C_s \cdot \frac{\sqrt{N_0}}{N_s - N_0} \quad (3.26)$$

For steeper slope of the calibration curve, lower value of n_0 and increased counting time, t , the absolute detection limit decreases.

Practical limits of detection have been defined by combining Equations 3.24 and 3.25

$$e = \frac{C_L}{C_1} \sqrt{\frac{n_1}{n_0}} \approx \frac{C_L}{C_1} \quad (3.27)$$

Table 3.2 lists the accuracy, e , as a function of the measured concentration, C_1 . The practical lower limit of detection is often considered as $3C_L$.

Table 3.2 The accuracy, e , as a function of concentration, C_1 [7].

C_1	C_L	$2C_L$	$3C_L$	$4C_L$	$5C_L$...	$10C_L$
e	$\pm 100\%$	$\pm 50\%$	$\pm 33\%$	$\pm 25\%$	$\pm 20\%$...	$\pm 10\%$

Part II

Experimental arrangement and measurement results

Chapter 4

Equipment used in the experimental setup

This chapter will give a short description of the different components that have been used in the experimental setup. Pictures of some of the components described in this and the following chapters are included in Appendix A.

4.1 Radiation detection system

In general radiation detection systems convert the energy of the radiation that is deposited in the detector into an electric signal. Detector systems can be operated in one of three modes: *pulse*, *current* and *mean square voltage mode*. Pulse mode operation is the only mode that measures the energy deposited in the detector by each radiation event. Therefore in X- and gamma-ray fluorescence measurements the detector is operated in pulse mode. The most important properties of radiation detection systems applied to on-line fluorescence measurements are:

Detection efficiency: The fluorescent X-ray flux will have low intensity. Therefore it is of paramount importance that all incident fluorescent radiation on the detector surface is stopped within the detector.

Energy resolution: The ability to resolve radiation events whose energies lie near each other determines the systems ability to separate the X-ray energies, and reject scattered radiation.

Linearity: For detectors operated in pulse mode, the amplitudes must reflect the corresponding energy deposited in the detector. The linearity of the detector system will then govern the accuracy with which the energy of a radiation event can be measured.

Room temperature operation: The need for either cryogenic or electrical cooling of the detector will complicate operation and increase the cost of the system. An on-line radiation detection system should therefore operate at room temperature.

Radiation detection system consists of three main components: *radiation detector*, *preamplifier* and *amplifier*, as illustrated in Figure 4.1. A brief description of these components are given in the following subsections.

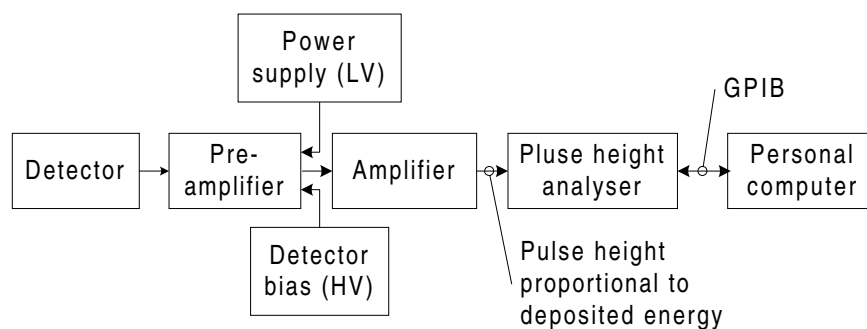


Figure 4.1 Block diagram of the radiation detection system.

4.1.1 Radiation detectors

Radiation detectors can roughly be categorized in two categories: *gaseous* and *solid state* detectors. Only solid state detectors have been used in this work, because of the need for high detection efficiency for radiation with less energy than 100 keV, see Table 4.6. Two different solid state detectors have been used, and a summary of their properties are presented in the two following paragraphs.

Scintillation detector

This detector is a model 51B51/2-HV-EP, manufactured by Scionix Holland BV. The scintillation crystal is NaI(Tl) (51 mm diameter and 51 mm high), and the detector has built-in high voltage power supply and charge sensitive preamplifier. The detector has a very high stopping efficiency, due to the high density and large dimensions of the crystal. Though, a disadvantage is its relatively poor energy resolution of approximately 11% in the energy range of interest. Unless stated, the detector was operated with 4 μ s peaking time, 2 μ s shaping time and 700 V high voltage. Detailed specifications on this detector can be found in the Appendix, Section B.1.

Semiconductor detector

This detector is an eV-180 series semiconductor detector, manufactured by eV Products. The detector crystal is made of $\text{Cd}_{0.9}\text{Zn}_{0.1}\text{Te}$ ($3 \times 3 \times 2 \text{ mm}^3$) and mounted directly on the back of a BNC connector. It is designed to be plugged on an eV-550 or any standard laboratory charge sensitive preamplifier. The detector has a high stopping efficiency, due to high Z elements and high density. Its energy resolution is relatively good, approximately 3% in the energy range of interest. Unless stated, the detector was operated with 2 μ s peaking time, 1 μ s shaping time and 200 V detector bias. Detailed specifications on this detector are listed in the Appendix, Section B.2.

4.1.2 Amplifiers

Preamplifiers

The built-in charge sensitive preamplifier of the scintillation detector is documented in the Appendix, Section B.1.

All measurements with the CdZnTe detector in this work were performed with the eV-550 preamplifier. This preamplifier is a charge sensitive configuration and has low noise for detector capacitances in the range of 0 to 100 pF. Detailed specifications on this preamplifier are listed in the Appendix, Section B.3.

Main amplifier

The main amplifier used was a Tennelec TC-244. It has an eight-pole shaping network that can produce either triangular or near-gaussian shaped unipolar pulses along with bipolar shaped pulses. Some of the amplifiers specifications are listed in Table 4.1, more specifications can be found in Reference [9].

Table 4.1 Summary of Tennelec TC-244 technical specifications.

Property	Specification
Pulse shaping	Active eight-pole shaping network <ul style="list-style-type: none"> • Gaussian unipolar • Triangular unipolar • Bipolar
Gain range	Continuously variable from $\times 2.5$ to $\times 3\,000$
Integral nonlinearity	Uni- and bipolar $\leq \pm 0.04\%$ over 0 to 10 V output range with 4 μs peaking time
Noise	$\leq 4.5 \mu\text{V}_{rms}$ referred to the input for 4 μs peaking time, with Gaussian unipolar shaping and gain of 1 000.

4.2 Data acquisition system

The data acquisition system consists of two main components:

- *Multi channel analyzer* (MCA), equipped with *General Purpose Interface Bus* (GPIB, IEEE 488).
- Laptop computer, equipped with GPIB interface and *LabVIEW* Version 4.01 data acquisition software.

4.2.1 Multi channel analyzer

The MCA is a model PCA-Multiport-E/R, manufactured by Oxford Instruments Inc. It has a 14 bit Wilkinson analog to digital converter (ADC), which operates at 100 MHz. Acquired pulse height spectra are stored in the internal random access memory (RAM), and can be uploaded to an external computer through it's GPIB interface either during or after acquisition. In this study the MCA is operated in pulse height analyser (PHA) mode only. Detailed specifications on the MCA can be found in Reference [10].

4.2.2 Software

LabVIEW

In order to control the MCA and transfer the acquired spectra to the computer LabVIEW, a product of *National Instruments*, was used. LabVIEW is a general-purpose graphical programming language, called *G*, with extensive libraries, an integral compiler and debugger, and an application builder for stand-alone applications [11]. Programs written in *G* are referred to as virtual instruments (VI) and can be stored separately in a file or grouped together in a library. These files are assigned the `.vi` or `.llb` extension, respectively. VIs consist of three parts:

Front panel: The interactive graphical user interface. It can contain knobs, push buttons, graphs and other controls and indicators.

Block diagram: The source code of the program.

Icon and connector pane: A VI within another VI is referred to as a *subVI*. The icon and connector pane is the graphical equivalent of a parameter list. It enables VIs to send and receive data from subVIs.

By linking together built in functions, VIs, controls and indicators a program can be built. Programs are executed from the front panel.

The PHA.vi program

Initially this program was developed by Hanne Pedersen [12], for use together with a measuring table for industrial gamma tomography [13]. During the period of June to August 1997, it was further developed by Sophie Boual. The program was adapted and modified for use in this study. It controls and reads data from the PHA through the GPIB bus. The functions that are implemented in the program are:

Initialisation: Set the following properties of the MCA

- ADC conversion gain.
- Preset on or off.
- Real and live time.

- Dead time control internal or external.
- Memory size and group.

Further, properties of the experimental arrangements can be specified

- Measurement name.
- Comments.
- Amplifier fine and coarse gain.
- Amplifier shaping and peaking time.
- Gradient and offset for energy calibration.

Acquisition: Start new or stop ongoing data acquisition.

Spectrum: Display the acquired differential pulse height spectrum as a function of channel or energy [keV].

Region of interest: Determine the area beneath a peak in the spectrum (numeric integration). Linear interpolation between the continuum values on either side of the peak can be used to compensate for the influence of the continuum.

Peak search algorithm: Estimate the position (energy channel) of a peak in the acquired spectrum.

Noise analysis: Determine upper and lower half width at half maximum and symmetric properties of the full energy peak.

Save and load: Store and retrieve data from tabulator delimited ASCII text file.

Smoothing: Apply a median filter, with user controllable rank, to the acquired spectrum.

Documentation on the `PHA.vi` and its subVIs can be found in Appendix C.

4.3 Radiation sources

4.3.1 Radioactive isotopes

In this study two high intensity ^{241}Am (americium) gamma emitters, with a main line emission energy of 59.5, keV were used.

Disk source

The disk source has a nominal activity of 1 110 MBq , or 30 mCi (tolerance $\pm 10\%$). It is incorporated in a ceramic enamel and sealed in a welded stainless steel capsule, with an overall diameter of 10.2 mm, active diameter of 7.2 mm and thickness of 5 mm. The manufacturers data sheet for this source is included in the Appendix, Section D.1.1.

Point source

The point source has a nominal activity of 518 MBq, or 14 mCi (tolerance +15%, -10%). It is incorporated in a ceramic bead and sealed in a welded stainless steel capsule, with an overall diameter of 3 mm, active diameter of 2 mm and length of 10 mm. The manufacturers data sheet for this source is included in the Appendix, Section D.1.2.

4.3.2 X-ray tubes

During this study two different X-ray tubes have been used:

- Balteau Baltospot GDF-165
- Andrex SMART 200

Two different tubes had to be used because the X-ray insert of the Balteau X-ray tube went “soft”, i.e. loss of vacuum. This is why some of the measurements only have been performed on one of the two tubes.

Both these tubes have been designed for use within *Non-Destructive Testing* (NDT). The variables that govern the emission from X-ray systems are primarily anode material, tube voltage and current. These parameters determine the maximum photon energy, total intensity and spectral distribution. Table 4.2 contains these parameters for the tubes used in this work.

Table 4.2 Summary of technical specifications for X-ray tubes.

Property	GFD-165	SMART 200
Tube voltage	80 - 160 kV	60 - 200 kV
Tube current	3.0 - 5.0 mA	0.5 - 4.0 mA
Anode material	tungsten	tungsten

In order to calculate theoretical fluorescence intensities generated using polychromatic excitation sources, knowledge of their emission spectra is necessary, ref. Section 3.2. However, for the X-ray tubes used here no, information regarding emission spectra could be obtained from either documents accompanying the equipment or the manufacturer. Attempts were then made to determine the spectral distribution of the tubes experimentally.

Spectral distribution

Two different approaches were used in order to record the X-ray tube’s emission spectra. In the first approach the X-ray tube and detector were positioned so that both units were directly facing each other. In order to reduce the high radiation flux emanating from the X-ray tube, both the X-ray tube and detector were collimated. The primary radiation from the X-ray tube passed a 6 mm long lead collimator with 1 mm internal diameter. Similarly, the aperture of the detector was reduced by a 4 mm long lead collimator with 1 mm internal diameter. To maximize the

count rate of the detector system the shortest peaking and shaping times, $0.5 \mu\text{s}$ and $0.25 \mu\text{s}$ respectively, were set on the amplifier. While operating the X-ray tube at its lowest voltage and current settings, an attempt to record a spectrum was done. This attempt resulted in massive pile-up, as a result of this the amplifier chain went into saturation. In addition the dead time losses in the PHA were close to 100%.

In the second approach both the X-ray tube and detector were collimated with rectangular $3 \times 3 \text{ mm}^2$ and 20 mm deep collimators. The incident radiation irradiated a sample of distilled water, and the scattered radiation emitted at 90° was detected. Within the energy range of 0–200 keV the photoelectric effect and Compton scattering are the dominating interaction mechanisms, ref. Figure 2.7. Fluorescent radiation generated in the sample is below the noise threshold of the detector system, and therefore will not be detected. The influence of Rayleigh scattering is assumed to be negligible in the specified energy range. Consequently, the radiation detected will mainly be Compton scattered radiation.

The probability of Compton scattering is dependent on the X-ray energy, as a result the recorded spectrum will be distorted from this effect. In addition, the acquired spectrum need to be corrected for the energy transfer between the incident photon and the recoil electron. By rearranging Equation 2.6 for E_γ , the energy of the incident photon is given as

$$E_\gamma = \frac{E'_\gamma}{1 - \frac{E'_\gamma}{m_e c^2} (1 - \cos\theta)} \quad (4.1)$$

The spectra recorded using this method for different voltage and current settings are presented in Figures 4.2, 4.3 and 4.4.

When comparing the spectra in Figures 4.2 and 4.3 it is evident that the Andrex tube produces radiation with higher intensity than the Balteau tube for identical settings. This is because the high voltage generator of the Balteau tube operates in pulse mode.

The recorded spectra are not sufficiently accurate for estimating theoretical fluorescence intensities. Still, the spectra does provide information on in what energy range the intensity is high. This information can be used to determine on what elements that these tubes can ionize the *K*-shell.

X-ray tube intensity

Another property of the X-ray tube's emission spectra is the total or integrated intensity, i.e. the area under the spectral distribution curves. Due to count rate limitations of the detector system, the integrated intensity could not be recorded with the detector directly facing the tube, as previous described. For each spectra in Figure 4.4 an integrated intensity was calculated by integrating from the noise threshold to maximum energy. The values that are obtained in these calculations are not good estimates of the tubes integral intensity, because the radiation from the tube has been attenuated and scattered through the water sample before detection.

To correct for the effect of the radiation interacting within the sample, two additional measurements were performed with the ^{241}Am disc source as radiation source. In the first measurement the disk source was positioned on the window of the X-ray tube, and a spectrum of the

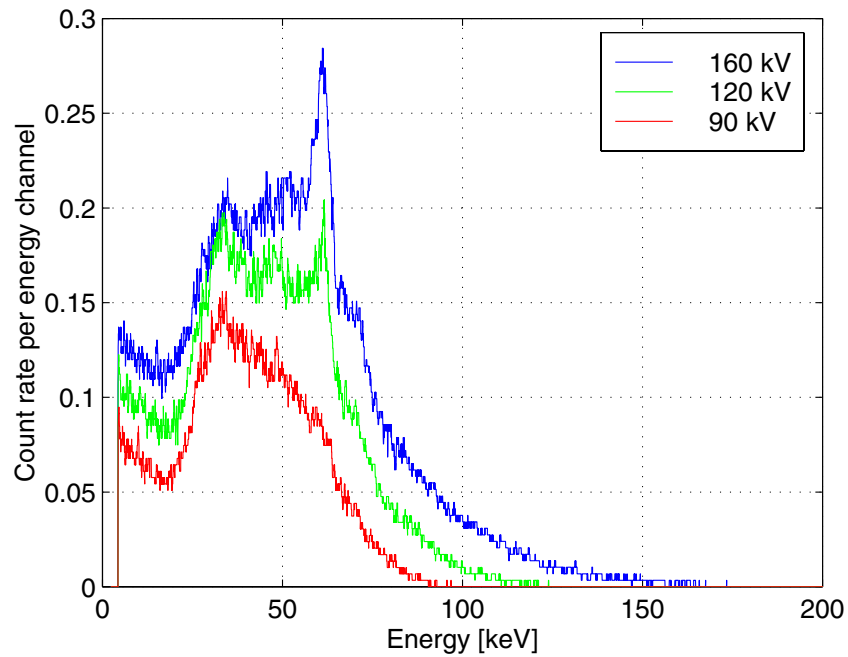


Figure 4.2 Balteau Baltospot GFD-165 emission spectra, calculated from radiation scattered 90° through a water sample for different high voltage settings. Tube current: 0.5 mA.

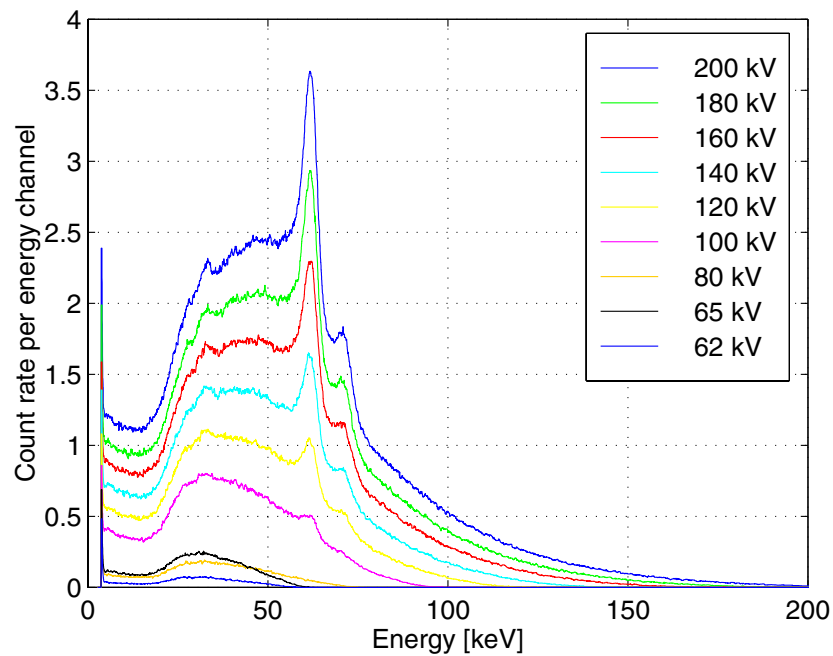


Figure 4.3 Andrex SMART 200 emission spectra, calculated from radiation scattered 90° through a water sample for different high voltage settings. Tube current: 0.5 mA.

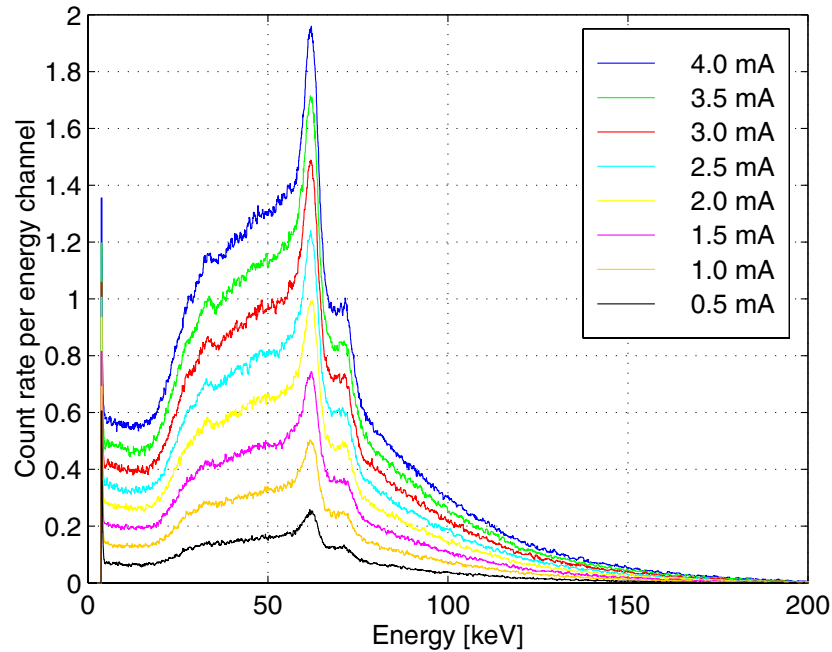


Figure 4.4 Andrex SMART 200 emission spectra, calculated from radiation scattered 90° through a water sample for different tube current settings. Tube high voltage: 200 kV.

scattered radiation was recorded. From this spectrum the integrated intensity of scattered radiation, I_{sc} , was calculated. The second measurement was conducted with the ^{241}Am source in the same position, but the water sample had been removed. In its place, the detector was positioned so that the aperture of its collimator was placed at the radiation's entry point to the sample. Also, the integrated intensity, I_{dir} , of this spectrum was calculated. The ratio of the integral intensities, I_{dir} to I_{sc} , was used as a scaling factor. By multiplying the detected integrated intensities of scattered radiation from the X-ray tube with the scaling factor, an estimate for the incident integral intensity on the sample surface was obtained.

A linear function that describes the relationship between both the scattered and estimated direct integral intensities as a function of the tube current, was found by using linear regression. The results are presented in Figure 4.5, where the left Y axis indicates the non scaled integral count rate and the right Y axis indicates the scaled integral count rate.

X-ray tube stability

The stability of the X-ray tube's emission is an important factor that will influence the accuracy of the measurement. Variations in tube current and high voltage will result in intensity variations and spectrum shift, respectively. Which in turn will lead to fluctuation amongst repeated measurements with identical experimental conditions.

By operating the semiconductor detector in current mode, the average energy deposition in the detector is measured. Thereby the variation in detector current will yield information

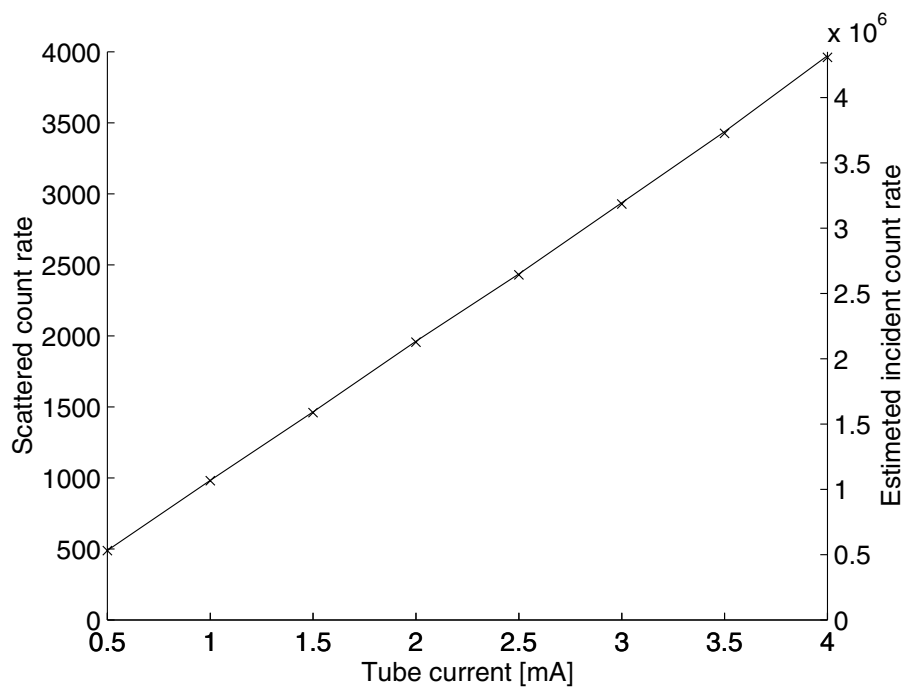


Figure 4.5 Andrex Smart 200 X-ray tube scaled and non-scaled integral count rate as a function of tube current at 200 kV tube voltage. The left *Y* axis indicates the non scaled integral count rate and the right *Y* axis indicates the scaled integral count rate.

on the stability of the X-ray tube emission. In current mode a current-measuring device, e.g. a picoammeter, is connected in series with the detector and high voltage supply. Figure 4.6 illustrates the experimental setup for current mode operation.

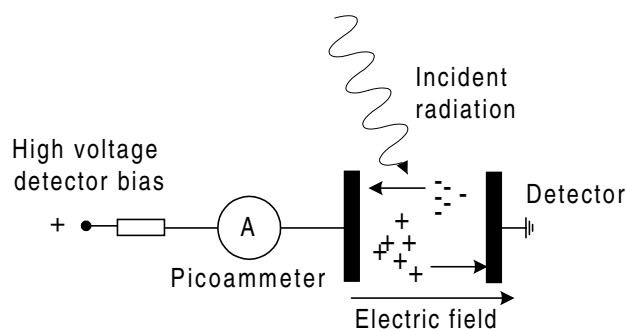


Figure 4.6 Schematic illustration of the detector system operated in current mode.

Current mode measurements were conducted with the X-ray tube and detector directly facing each other. The radiation beam from the X-ray tube was shaped by a rectangular $3 \times 3 \text{ mm}^2$ collimator, made up of two 4 mm thick lead sheets which were spaced 13 mm apart. The radiation detector was collimated with a rectangular $3 \times 3 \text{ mm}^2$ and 19.5 mm thick collimator, made up of eight 2 mm thick lead sheets which were spaced 0.5 mm apart.

A Keithley Model 485 autoranging picoammeter was utilized to perform the current readings [14]. Measurements were carried out on the Balteau Baltospot GFD-615 X-ray tube for minimum, 3 mA, and maximum, 5 mA, tube current settings in high voltage steps of 10 kV within the range 90 to 160 kV. For each combination of tube settings the minimum and maximum current was recorded. The minimum and maximum detector current were in addition measured over two different time intervals of $33\frac{1}{3}$ and 300 s.

The relative deviation from the mean value for each measurement is plotted as a function of tube voltage in Figure 4.7. The curves in the plot indicate that the best stability is obtained by operating the tube at, or close to maximum current and voltage settings.

4.4 Shielding

4.4.1 Detector shielding

All radiation detectors record some background signal, whether it is from cosmic radiation or natural radioactivity in the environment. The characteristics of this background varies greatly with detector type and size. Large volume detectors will have higher background counting rates than small volume detectors. The magnitude of the background will influence on the minimum detectable radiation level, and therefore is of most importance for applications involving low activity. Another cause for detector shielding is to isolate the detector so that scattered or radiation from other sources do not influence on the measurement.

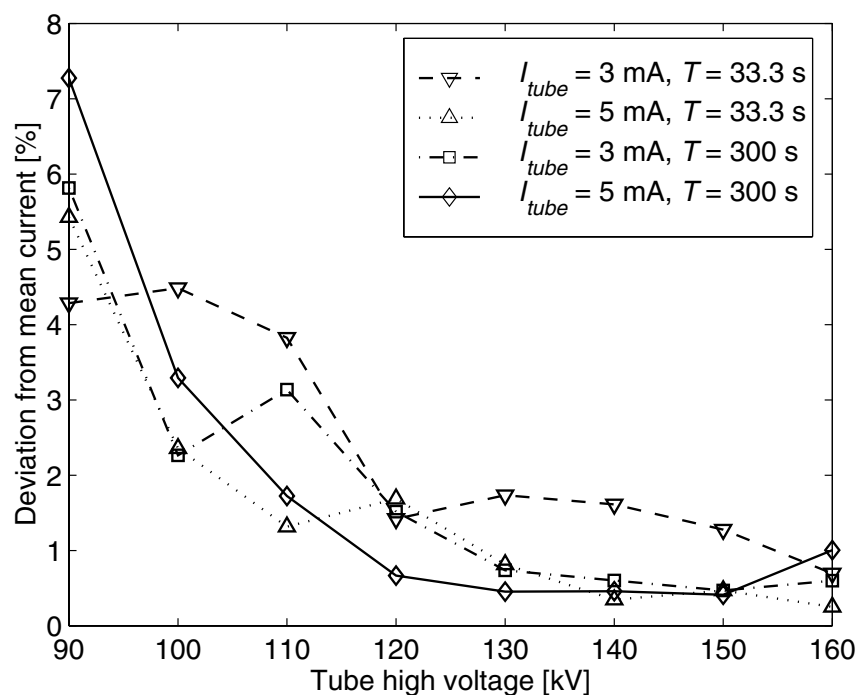


Figure 4.7 Balteau GFD-165 X-ray tube stability.

Scintillation detector

For most of the measurements in this study only a small fraction of the scintillator surface and volume was exposed to radiation emanation from the sample. I.e. the recorded background is therefore higher than what could have been achieved with a scintillator of less diameter and height.

Four different background spectra from the scintillation detector are plotted in Figure 4.8. From the spectra, it is evident that the lead shield provides the best overall reduction in background count rate.

A disadvantage of the lead shield is the presence of fluorescent K_{α} and K_{β} lines from the lead. The fluorescent radiation originate from photoelectric absorption of energetic cosmic radiation. By using a three layered shield of lead, copper and tin, radiation that is not absorbed within the layer of lead will interact within the copper layer. Fluorescent radiation from copper has lower energy than the critical excitation energy of tin, and therefore no fluorescent radiation from the tin will be generated through this process. Still a small fluorescence peak from tin can be seen in the spectra. This peak originate from photoelectric absorption of cosmic radiation.

Semiconductor detector

The detector volume of the semiconductor detector is substantially smaller compared to the scintillation detector. With small crystal dimensions the detected background is much lower. The two recorded background spectra plotted in Figure 4.9 confirm this.

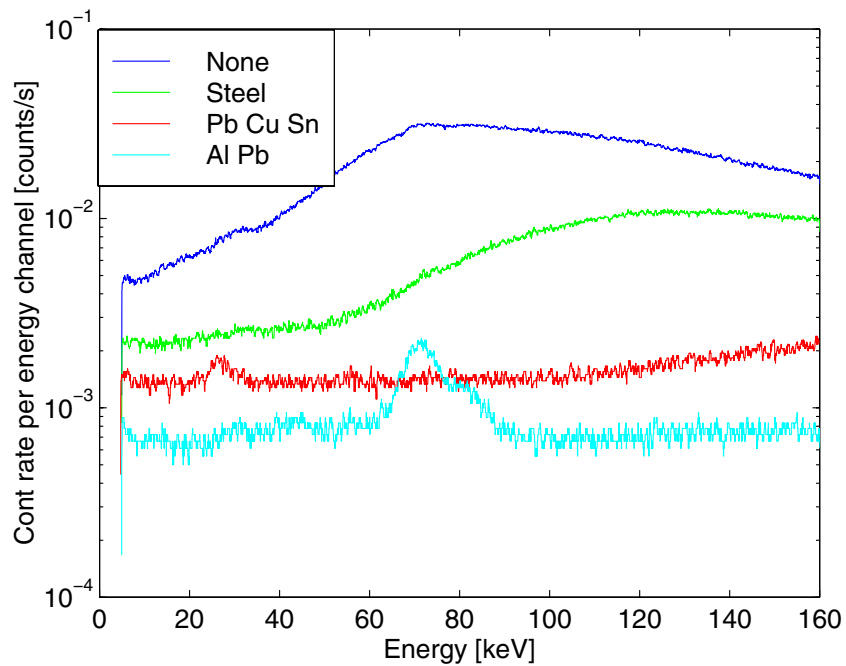


Figure 4.8 NaI(Tl) scintillation detector background spectra with different types of shielding. None: detector housing. Steel: 4 mm stainless steel. Pb Cu Sn: 2 mm lead, 4 mm copper and 3 mm tin. Al Pb: 4 mm aluminum and 4 mm lead.

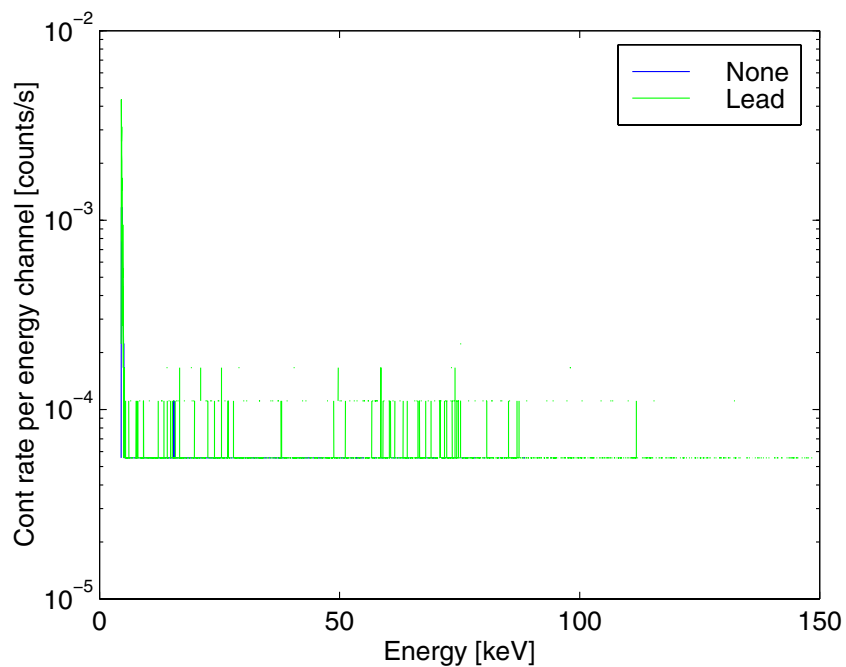


Figure 4.9 CdZnTe semiconductor detector background spectra. None: detector housing. Lead: 4 mm lead.

4.4.2 X-ray tube shielding

In order to ensure safe operation of the Balteau Baltospot GFD-165 X-ray tube an interlocked lead enclosure was designed and built at UMIST. Its inner dimensions, of $860 \times 710 \times 400 \text{ mm}^3$ are large enough to allow both the X-ray tube and the detector to fit inside. In the following subsections the thickness of the shielding is worked out so that a dose rate design criteria of $1 \mu\text{Gy}/\text{h}$ at the surface of the cabinet is met.

In the calculations below it is assumed that spherical geometry holds, i.e. the photon flux diminishes as $1/d^2$, where d is the distance to the source [4].

Barrier requirements

The radiation output from the tube at maximum voltage is listed in the manual to be $100 \text{ mGy}/\text{mAs}$ at 1 m.

Assuming barrier at 50 cm. The dose rate, DR , at 50 cm is

$$DR = 100 \text{ mGy}/\text{mAs} \cdot \frac{(100 \text{ cm})^2}{(50 \text{ cm})^2} \cdot 5 \text{ mA} \cdot 60^2 = 7.2 \cdot 10^6 \mu\text{Gy}/\text{h} \quad (4.2)$$

The relative attenuation needed is then $1/7.2 \cdot 10^6 \approx 1.4 \cdot 10^{-7}$, which can be achieved with a 6 mm thick lead shield [15].

Leakage barrier requirements

The maximum radiation leakage from the tube is listed in the manual to be less than $2175 \mu\text{Gy}/\text{h}$. What distance this was measured at is unknown. Leakage is usually quoted at 1 m. Assuming that the barrier is at 50 cm, the leakage dose rate, LDR , at this distance is

$$LDR = 2175 \mu\text{Gy}/\text{h} \cdot \frac{(100 \text{ cm})^2}{(50 \text{ cm})^2} = 8.7 \cdot 10^3 \mu\text{Gy}/\text{h} \quad (4.3)$$

The relative attenuation needed is then $1/8.7 \cdot 10^3 \approx 114 \cdot 10^{-6}$, which can be achieved with a 4.5 mm thick lead shield [15].

Dose measurements

Dose measurement were measured around the lead enclosed housing of the X-ray tube using a Mini-Instruments SmartIon detector, which had been calibrated at the North Western Medical Physics department. The tube was operated at its maximum voltage and current, i.e. 200 kV and 5 mA. All the measurements were made with the lid, beam collimators and the rest of the internal shielding in place. The unit must only be used with all the shielding in place. Measurements were carried out with and without scattering material, e.g. sample. There was no significant difference between the dose rates obtained in the two circumstances. The dose rates obtained are listed in Table 4.3.

Table 4.3 Measured dose rates around the lead enclosure.

Site	Value
Front of the box (in line of main beam)	$\approx 1 \mu\text{SV/h}$
Right side of the box	$< 1 \mu\text{Sv/h}$
Underneath box	$\approx 1 \mu\text{SV/h}$
Back of box (maximum at lower vent duct)	$\approx 6 \mu\text{SV/h}$
Office adjoining the wall at back of the box	$< 1 \mu\text{Sv/h}$

4.5 Samples

To prepare samples of liquid with known concentration of the specie, SpectrosoL standard solutions from BDH Laboratory Supplies were used. Four different standards were obtained: cadmium (Cd), caesium (Cs), platinum (Pt) and lead (Pb). All standards have a concentration of $1\,000 \pm 5$ ppm, which is equivalent to 1 mg/ml .

Table 4.4 Physical data SpectrosoL standard solutions, from BDH Laboratory Supplies.

Standard solution	Solute	Matrix
Cadmium $1\,000 \pm 5$ ppm	Cadmium nitrate $[\text{Cd}(\text{NO}_3)_2]$	Nitric acid $[\text{HNO}_3]$, 0.5 mol/l
Caesium $1\,000 \pm 5$ ppm	Caesium nitrate $[\text{Cs}(\text{NO}_3)_2]$	Nitric acid $[\text{HNO}_3]$, 0.5 mol/l
Platinum $1\,000 \pm 5$ ppm	Platinum chloride $[\text{H}_2\text{PtCl}_6]$	Hydrochloric acid $[\text{HCl}]$, 0.5 mol/l
Lead $1\,000 \pm 5$ ppm	Lead nitrate $[\text{Pb}(\text{NO}_3)_2]$	Nitric acid $[\text{HNO}_3]$, 0.5 mol/l

The samples were prepared by dilution of the standard with distilled water using standard laboratory volumetric glassware, i.e volumetric flasks and pippettors.

The X-ray critical excitation energies wavelengths of the samples are listed in Figures 4.6 and 4.5, respectively.

Table 4.5 Critical excitation energies in keV of the *K* level [16].

Element	Energy [keV]	Element	Energy [keV]
^{48}Cd Cadmium	26.716	^{78}Pt Platinum	78.381
^{55}Cs Caesium	39.987	^{82}Pb Lead	88.005

Table 4.6 X-ray wavelengths in Å* and in keV [17]. The probable error (p.e.) is the error in the last digit of wavelength. Designation indicates both Siegbahn and empirical notation.

Element	Designation		Wavelength [Å*]	p.e.	Energy [keV]	
	Siegbahn	Conventional				
⁴⁸ Cd Cadmium	K_{α_2}	KL_{II}	0.539422	3	22.9841	
	K_{α_1}	KL_{III}	0.53501	3	23.1736	
	K_{β_3}	KM_{II}	0.355050	4	34.9194	
	K_{β_1}	KM_{III}	0.354364	7	34.9869	
	K_{β_2}	$KN_{II,III}$	0.34611	2	36.822	
⁵⁵ Cs Caesium	K_{α_2}	KL_{II}	0.404835	4	30.6251	
	K_{α_1}	KL_{III}	0.40029	4	30.9728	
	K_{β_3}	KM_{II}	0.35505	4	34.9194	
	K_{β_1}	KM_{III}	0.354364	7	34.9869	
	K_{β_2}	$KN_{II,III}$	0.34611	2	35.822	
⁷⁸ Pt Platinum	K_{α_2}	KL_{II}	0.190381	4	65.122	
	K_{α_1}	KL_{III}	0.185511	4	66.832	
	K_{β_3}	KM_{II}	0.164501	3	75.368	
	K_{β_1}	KM_{III}	0.163675	3	75.748	
	K_{β_2}	KN_{II}	0.15939	1	77.785	
	$K_{\beta_2'}$	KN_{III}	0.1592	1	77.878	
		$KO_{II,III}$	0.15826	1	78.341	
		$K_{\beta_5''}$	KM_{IV}	0.16271	2	76.199
		$K_{\beta_5'}$	KM_{V}	0.16255	3	76.27
		K_{β_4}	$KN_{IV,V}$	0.15881	2	78.69
	⁸² Pb Lead	K_{α_2}	KL_{II}	0.170294	2	72.8042
K_{α_1}		KL_{III}	0.165376	2	74.9694	
K_{β_3}		KM_{II}	0.14681	4	84.45	
K_{β_1}		KM_{III}	0.14597	6	84.936	
$K_{\beta_2''}$		KN_{II}	0.14212	2	87.23	
$K_{\beta_2'}$		KN_{III}	0.14191	1	87.364	
		$KO_{II,III}$	0.141012	8	87.922	
		KP	0.1408	1	88.06	
		K_{β_5}	$KM_{IV,V}$			
		$K_{\beta_5''}$	KM_{IV}	0.14512	2	85.43
		$K_{\beta_5'}$	KM_{V}	0.14492	3	85.53
	K_{β_4}	$KN_{IV,V}$	0.14155	3	87.59	

Chapter 5

Gamma-ray stimulated fluorescence

The measurements presented in this chapter have all been carried out with the ^{241}Am isotope as the source of ionizing radiation. Two different modes of operation have been investigated experimentally:

- Fluorescence yield.
- Surface fluorescence measurements. With two different source positions:
 - Radiation source above surface
 - Submerged radiation source.

5.1 Fluorescence yield

The measurement system that is presented in this section was developed in order to experimentally investigate fluorescence yield from a specie diluted in liquid. Knowledge of the fluorescence yield can be used to determine the performance of an on-line system. To accurately measure the fluorescence yield it is necessary have knowledge of the incident radiation's energy and intensity in addition to the geometrical properties of the experimental setup. The first two requirements preclude the use of either of the two X-ray tubes available. A controlled setup was designed, and is presented in the next paragraph.

5.1.1 Experimental arrangement

The test sample to be analysed was contained in a plastic box with outer dimensions $75 \times 44 \times 22$ mm³ and 1.5 mm wall thickness. Radiation from the disk shaped ^{241}Am source passed a 30 mm long cylindrical lead collimator with a diameter of 1 mm. The radiation emanating from the sample was collimated with a rectangular 3×3 mm² and 19.5 mm thick collimator, made up of eight 2 mm thick lead sheets which were spaced 0.5 mm apart. By positioning the detector collimator perpendicular with respect to the direction of the incident radiation, one minimizes the influence of Compton scattered radiation, ref. Figure 2.5. The position of the sample box

relative to the collimated stimulation and detection paths determine the attenuation of both input and output radiation. Long attenuation paths also contribute to generate more scattered radiation. Therefore, by positioning the sample so that the point of intersection of the paths is close to the edges of the box, these effects will be minimized. The experimental setup is illustrated in Figure 5.1.

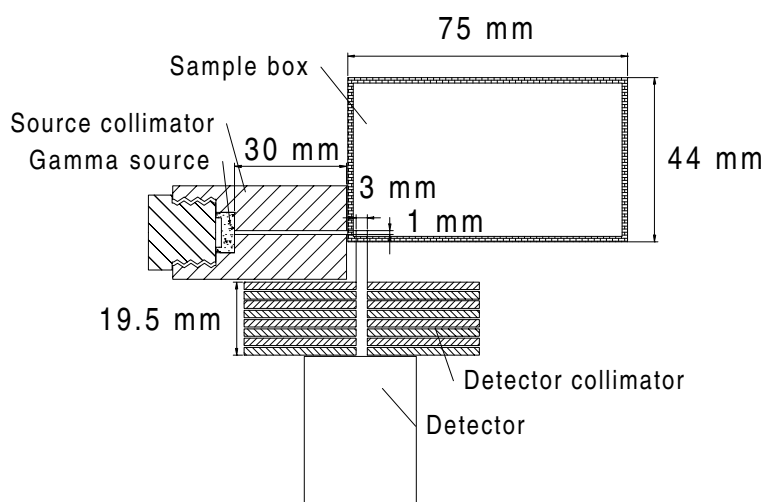


Figure 5.1 Experimental arrangement of gamma source, collimators, sample and detector for fluorescence yield measurements.

With this geometry the intersection of the collimated stimulation and detection paths define a small volume element in which the measured fluorescent radiation is produced.

5.1.2 Measurement results

Measurements with the setup described in the previous section were performed on the cadmium and caesium standard solutions with specie concentration 1 000 ppm. Spectra were recorded with both the scintillation and semiconductor detectors. The integration time was 18 000 s (5 hours) for all measurements.

In the spectra that were recorded no fluorescent K lines from either cadmium or caesium could be distinguished from the continuum. The reason for this was probably to low intensity in the incident radiation.

The only way to increase the incident intensity was by increasing the internal diameter of the source collimator. A second and third round of measurements were carried out, this time the diameter in the source collimator had been increased to 2 mm and 3 mm, respectively. The incident radiation intensities were measured to be approximately $5.3 \cdot 10^3$ photons/s for 2 mm and $10.3 \cdot 10^3$ photons/s for 3 mm diameter. In the third attempt small cadmium and caesium K_α lines could barely be distinguished from the continuum, in the spectra recorded with the semiconductor detector, see Figure 5.3.

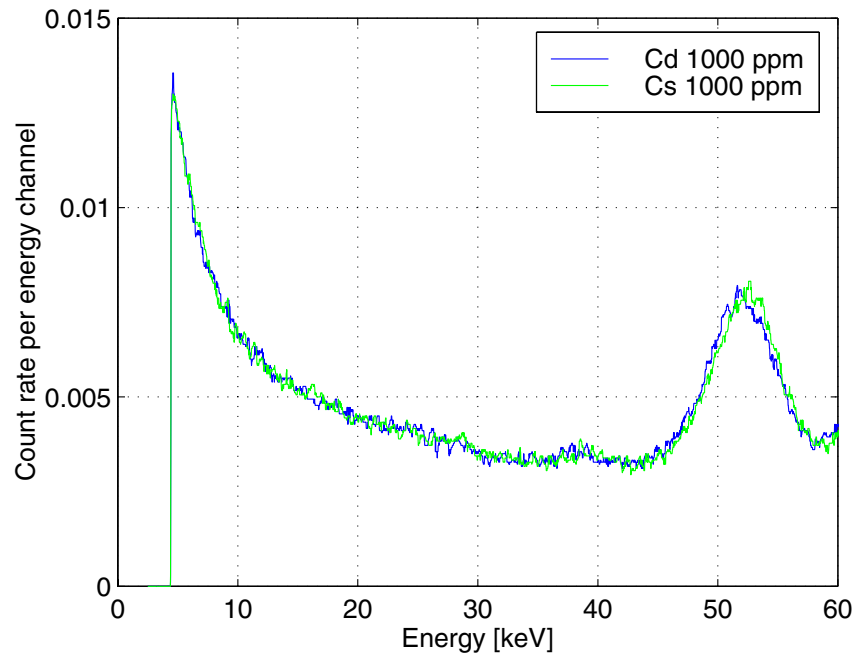


Figure 5.2 Recorded spectra for gamma-ray stimulated fluorescence yield measurements. Detector: NaI(Tl). Coarse gain: 20. Fine gain: 1.08.

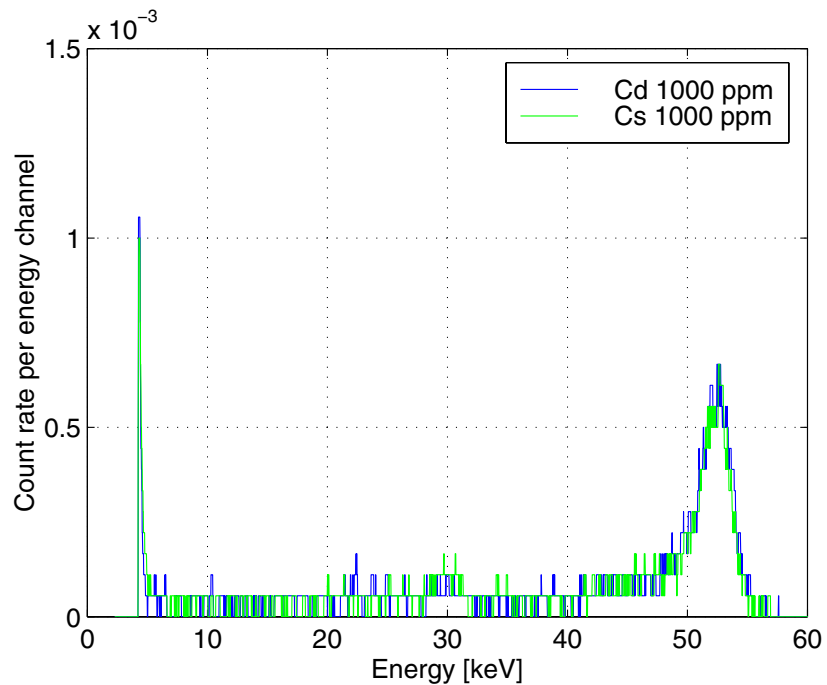


Figure 5.3 Recorded spectra for gamma-ray stimulated fluorescence yield measurements. Detector: CdZnTe. Coarse gain: 1000. Fine gain: 0.73.

If one were to try to increase the intensity of the incident radiation further, by widening the diameter of the source collimator problems would arise with respect to the semiconductor detector. The face of the detector has an area of $3 \times 3 \text{ mm}^2$, and therefore represent a practical limit. Further widening of the source collimator without increasing its length will result in a less well defined incident radiation beam and thereby also production volume.

A second option is to use a gamma-ray source with higher activity. Though this might introduce the problem of self absorption within the source. This can be illustrated by comparing the AMC.65 and AMC.66 disk sources, see Appendix Section D.1.1. The AMC.66 source has triple the nominal content activity compared to AMC.65, but the typical photon output in photons/s per steradian is only doubled.

The integral number of counts beneath the fluorescent peaks from cadmium and caesium are so low that they cannot be used to experimentally determine the fluorescence yield with any reasonable degree of precision.

5.2 Surface measurements

Based on the results in the previous section two new experimental arrangements were designed. In these arrangements the objective was to measure relative fluorescence, i.e. differences in fluorescent intensity for samples with different specie concentration. Also, the two different arrangements were used to test which geometry that provides the highest fluorescence intensities and less influence of scattered radiation. The sample was no longer contained in a closed vessel or box, but its surface was exposed. The motivation behind exposing the sample was two-sided: less attenuation of both incident and fluorescent radiation, and its potential use for pollution monitoring of open flows (see Chapter 1).

5.2.1 Source above surface

Experimental setup

A new source collimator was designed and manufactured for the disk shaped ^{241}Am source. This lead collimator expose the entire active area of the source, and defines a “cone shaped” beam. Thereby the radiation intensity incident on the sample was increased. In order to enable the detectors to detect as much of the radiation leaving the sample as possible, they were not collimated. The test sample to be analysed was contained in a plastic box with outer dimensions $80 \times 72 \times 55 \text{ mm}^2$.

The experimental arrangement is illustrated in Figures 5.4 and 5.5, for the scintillation and semiconductor detectors, respectively.

Measurement results

Measurements were performed with both detector arrangements on 1 000 ppm cadmium and caesium samples. In addition spectra from a distilled water sample was recorded. The measurements are presented in Figures 5.6, 5.7, 5.8 and 5.9. Three curves are presented in each figure. One for

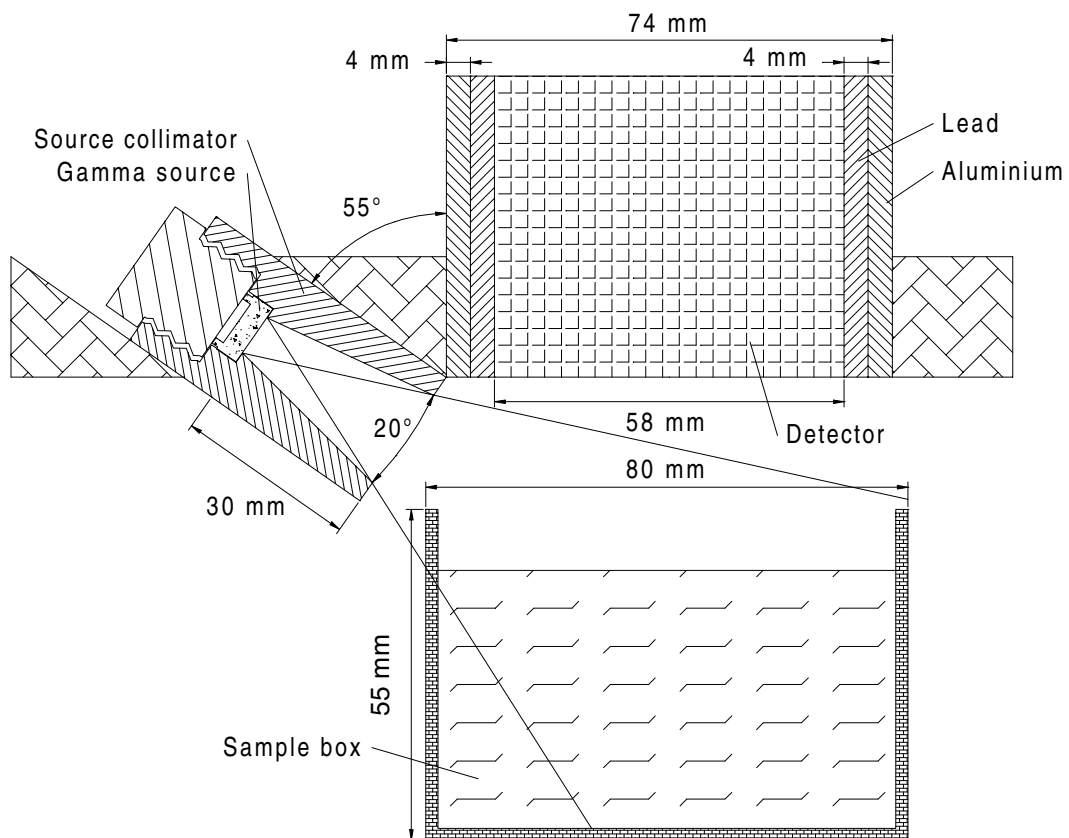


Figure 5.4 Experimental arrangement of gamma source, collimator, sample and scintillation detector for fluorescence surface measurements.

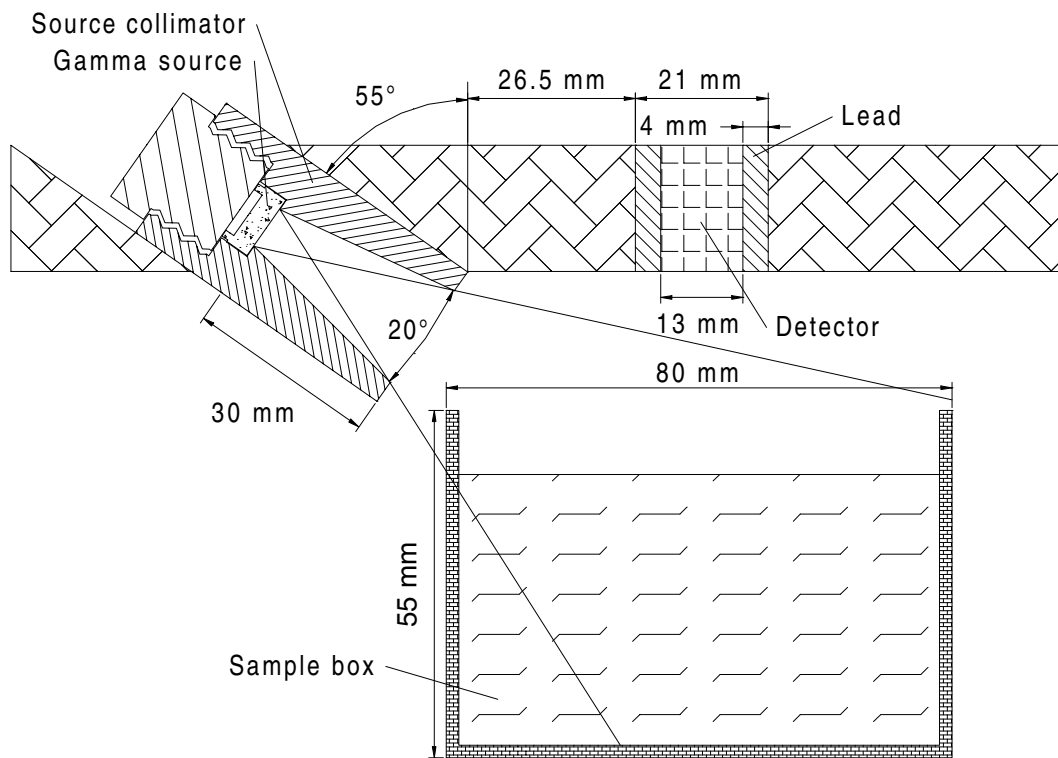


Figure 5.5 Experimental arrangement of gamma source, collimator, sample and semiconductor detector for fluorescence surface measurements.

the sample with cadmium or caesium content and one for the distilled water sample. The third curve is calculated from the difference in count rate per energy channel between the sample with a specie and the distilled water sample.

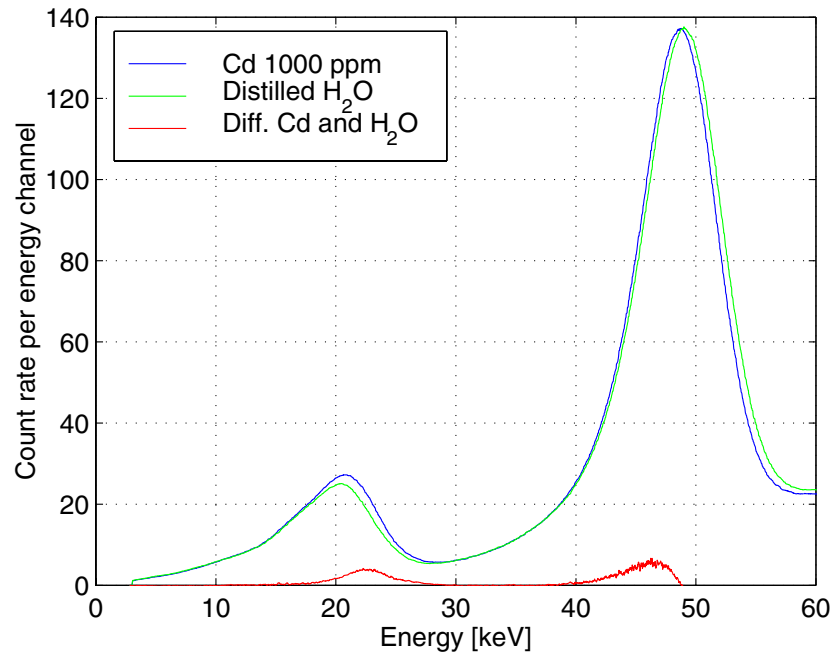


Figure 5.6 Recorded spectra for gamma-ray stimulated fluorescence, with source above the sample surface. Samples: cadmium 1 000 ppm and distilled water. Detector: NaI(Tl).

For the cadmium spectra recorded with the scintillation detector, the fluorescent radiation from cadmium is superimposed on the iodine X-ray escape and backscatter peak. The area under the fluorescent peak is so small that it can only be clearly seen in the curve where the difference between the cadmium and distilled water sample is plotted. The spectra for the caesium sample is easier to analyse, because the fluorescent radiation's energy is slightly higher than the iodine X-ray escape and backscatter peak energy.

The cadmium and caesium spectra, recorded with the semiconductor detector are easier to interpret, because of the higher energy resolution which allow better rejection of scattered radiation. In both the cadmium and caesium spectrum small fluorescent radiation peaks can clearly be distinguished from the continuum.

A comparison of the spectra recorded with the two detectors reveal a large difference in count rate. As discussed previously, this is due to the difference in crystal size between the detectors.

The recorded spectra are for the highest specie concentration available. Due to the small peak area, measurements on lower concentrations were not carried out. These results suggest that measurements have to be performed on samples with higher concentration or the incident radiation intensity will have to be increased.

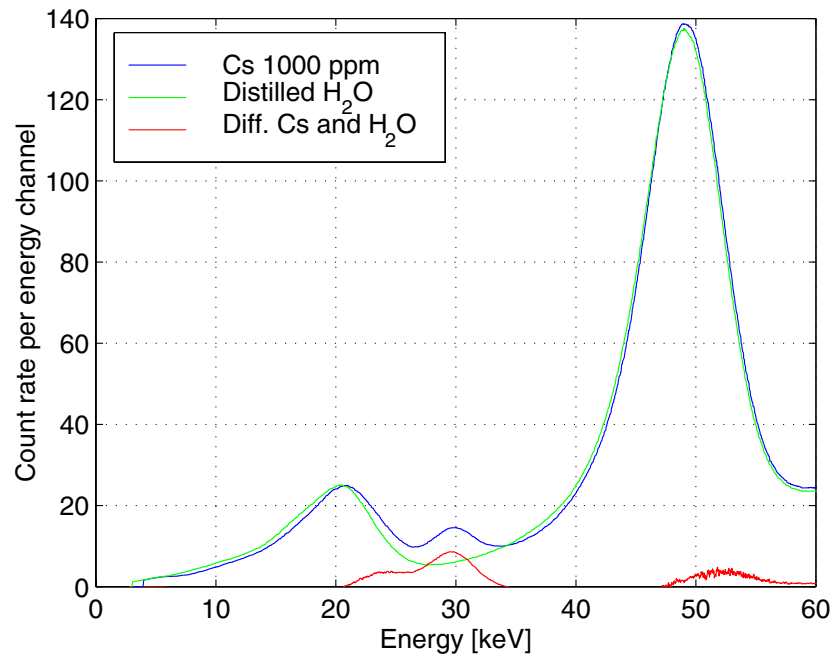


Figure 5.7 Recorded spectra for gamma-ray stimulated fluorescence, with source above the sample surface. Samples: caesium 1 000 ppm and distilled water. Detector: NaI(Tl).

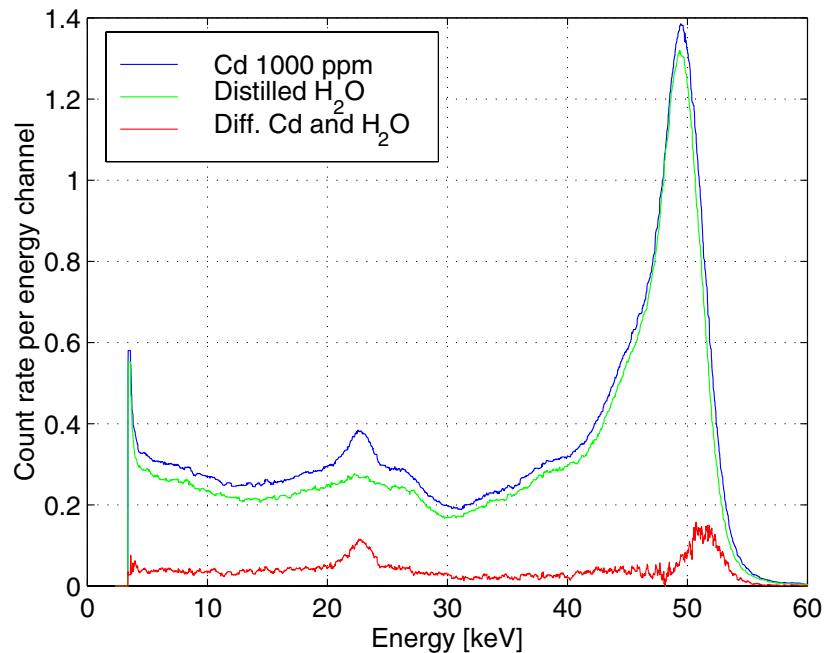


Figure 5.8 Recorded spectra for gamma-ray stimulated fluorescence, with source above the sample surface. Samples: cadmium 1 000 ppm and distilled water. Detector: CdZnTe.

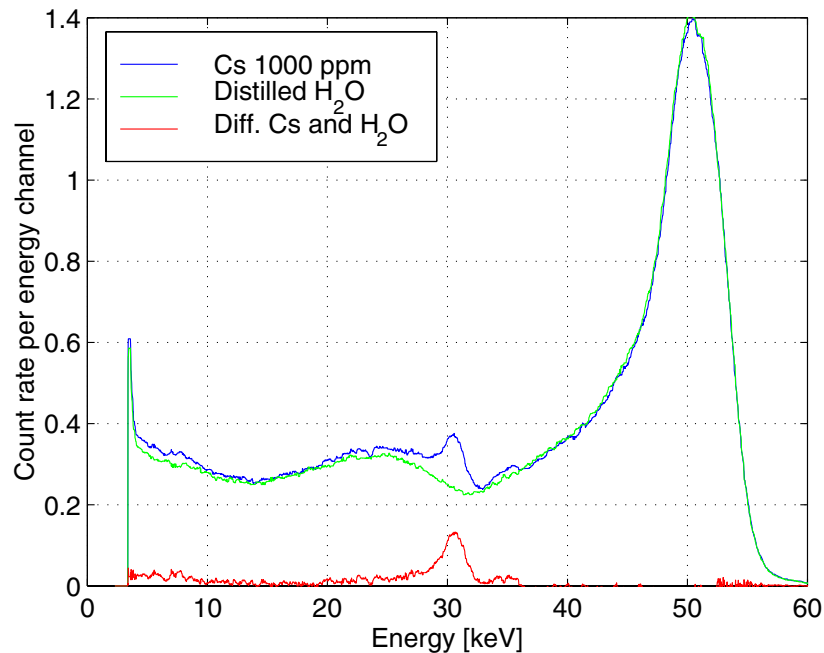


Figure 5.9 Recorded spectra for gamma-ray stimulated fluorescence, with source above the sample surface. Samples: caesium 1000 ppm and distilled water. Detector: CdZnTe.

5.2.2 Source submerged

Experimental setup

A source holder for the point shaped ^{214}Am source was designed and manufactured. The shape of the source lead holder was designed so that the active cylindrical pellet could be submerged, and that no radiation from it could enter the detector directly. For use with the scintillation detector, the back of the holder was attached in the center of the scintillation crystal, see Figure 5.10. When used together with the semiconductor detector, the holder was attached on the supporting bracket adjacent to the detector's lead shield, see Figure 5.11.

Measurement results

Measurements were first attempted with the arrangement which incorporated the scintillation detector. This arrangement of detector, source and sample proved to present a very high intensity of radiation to the detector surface, which resulted in pulse pile-up and high PHA dead time around 60%. The pulse pile-up and PHA dead time problems might have been reduced, for instance by covering a part of the detector face with a few millimeter thick lead sheet. Though this was not tried out.

Instead of modifying the experimental setup for the scintillation detector, the setup was re-arranged to accommodate the semiconductor detector. The change of detector will not greatly influence the ratio of fluorescent and scattered radiation, which is determined by the experimen-

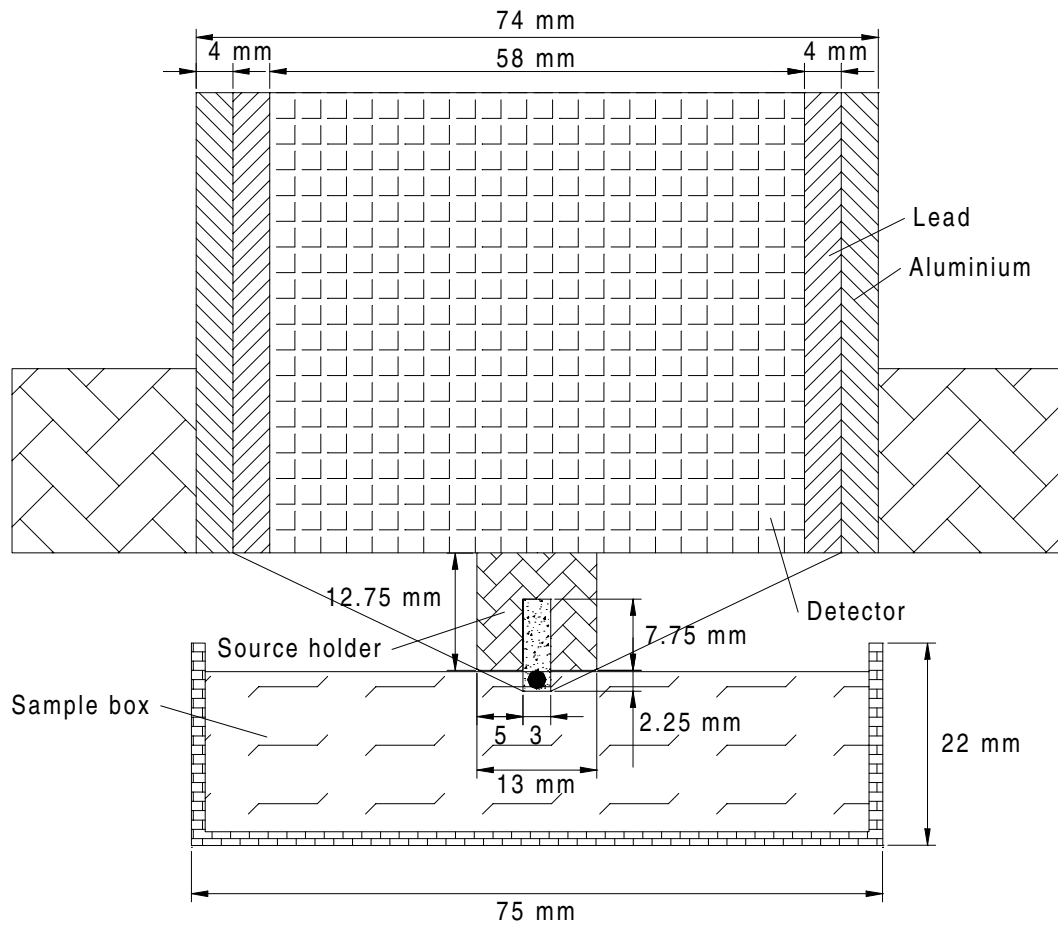


Figure 5.10 Experimental arrangement of gamma source, collimator, sample and scintillation detector for fluorescence surface measurements with submerged gamma-ray source.

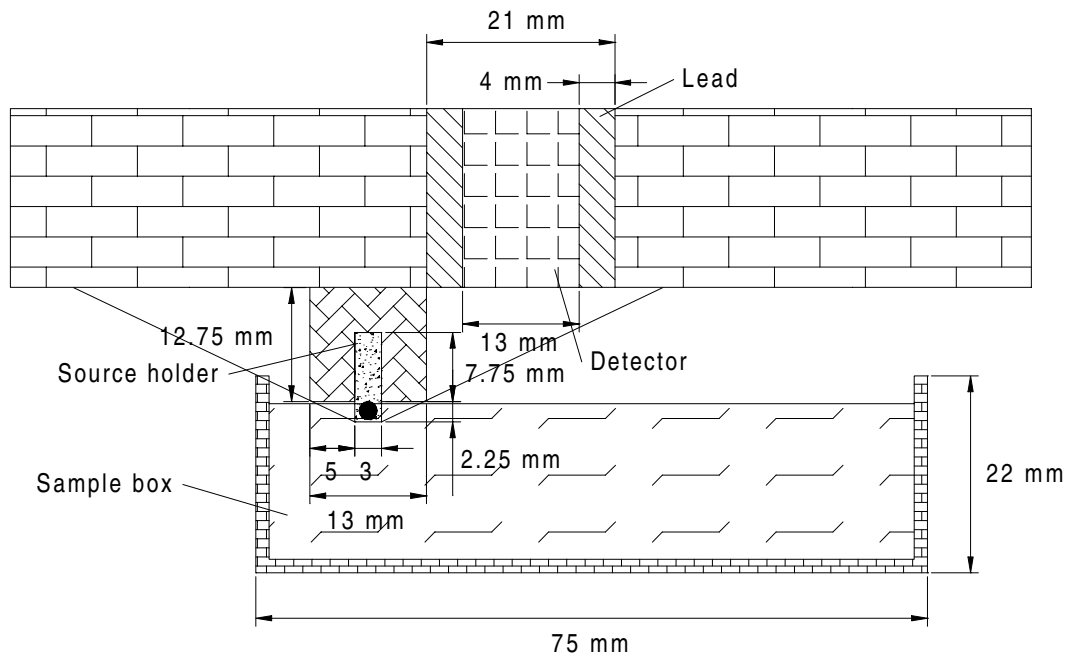


Figure 5.11 Experimental arrangement of gamma source, collimator, sample and semiconductor detector for fluorescence surface measurements with submerged gamma-ray source.

tal arrangement. Though, a disadvantage is that the semiconductor detector's smaller crystal size will result in poorer counting statistics.

Measurements were then conducted with the semiconductor detector on samples with cadmium and caesium concentrations in the range from 50 to 1 000 ppm. The measurement results are presented in Figures 5.12 and 5.13.

For the recorded cadmium spectra, the curves for the concentrations of 500, 750 and 1 000 ppm fluorescent peaks can be distinguished from the continuum. For concentrations lower than 500 ppm the spectra are practically indistinguishable from the water spectra. The recorded spectra for caesium were performed for fewer specie concentrations than with cadmium, due to lack of caesium standard. For the 1 000 ppm caesium measurement the sample box was only filled half way up, and therefore the count rate of both the continuum and fluorescent peak is lower than for the three other curves. For caesium fluorescent a peak could only be observed for the highest concentration of 1 000 ppm.

Similar to the results from the previous measurement mode, the integral number of counts beneath the fluorescent peaks from cadmium and caesium are low. The results suggest that measurements have to be performed on samples with higher concentration or the incident radiation intensity will have to be increased.

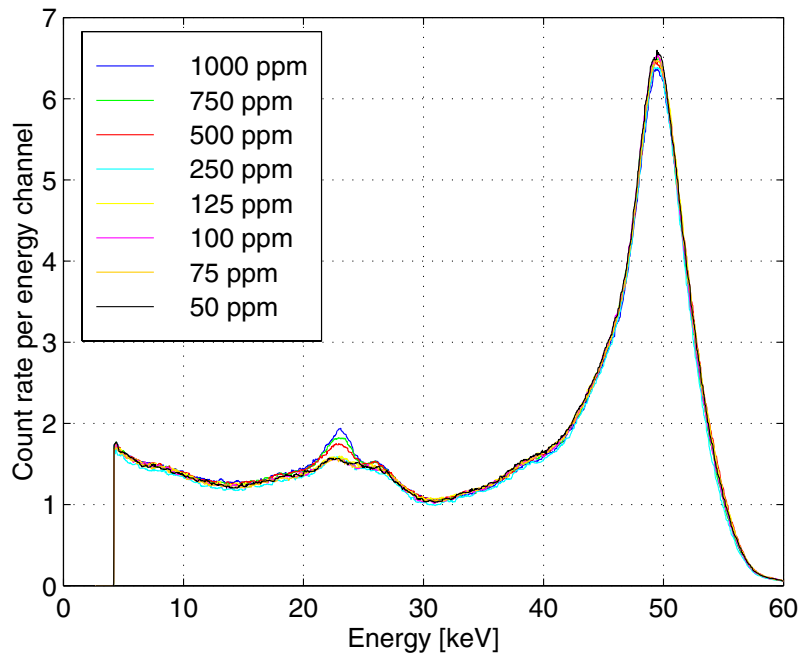


Figure 5.12 Recorded spectra for gamma-ray stimulated fluorescence, with submerged source. Samples: cadmium. Detector: CdZnTe. Integration time: 10 minutes.

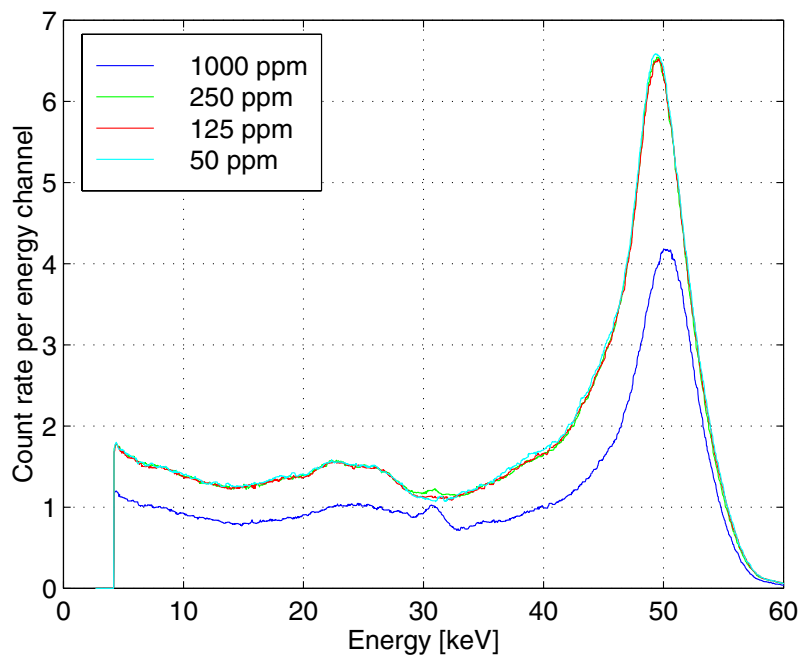


Figure 5.13 Recorded spectra for gamma-ray stimulated fluorescence, with submerged source. Samples: caesium. Detector: CdZnTe. Integration time: 10 minutes.

Chapter 6

X-ray stimulated fluorescence

The measurements presented in this chapter have all been carried out with the Andrex SMART 200 X-ray tube as the source of ionizing radiation. Four different measurement series have been carried out:

- Species in liquid host.
- Species in “gaseous” host.
- Variation of penetration depth for ionizing radiation.
- Variation of escape depth for fluorescent radiation.

6.1 Experimental arrangement

The experimental arrangement used for X-ray stimulated fluorescence is identical to the one used for estimating the spectral distribution of the X-ray tubes, see Section 4.3.2. The sample was contained in the same type of box, with outer dimensions $75 \times 44 \times 22 \text{ mm}^3$ and wall thickness 1.5 mm. The radiation beam from the X-ray tube was shaped by a rectangular $3 \times 3 \text{ mm}^2$ collimator, made up of two 4 mm thick lead sheets which were spaced 13 mm apart. The radiation detector was collimated with a rectangular $3 \times 3 \text{ mm}^2$ and 19.5 mm thick collimator, made up of eight 2 mm thick lead sheets which were spaced 0.5 mm apart. In order to minimize the influence of Compton scattered radiation incident on the detector, the detector collimator was positioned so that it picked up radiation emitted at 90° relative to the direction of incident radiation, see Figure 2.5. The experimental arrangement is illustrated in Figure 6.1.

6.2 Measurement results

Measurements were primarily performed on species in a liquid host, though measurements for two different concentrations were performed on species in a “gaseous” host. The experimental arrangement could accommodate both the scintillation and semiconductor detectors. Two spectra

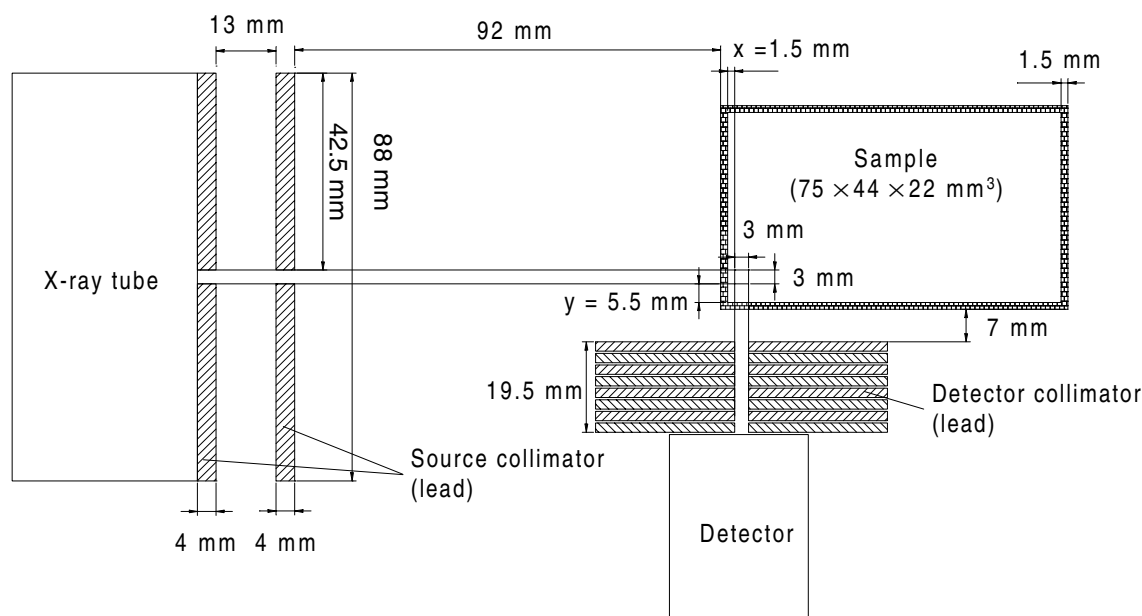


Figure 6.1 X-ray fluorescence measurement set-up.

with the same sample present were recorded with both detectors. When the two spectra were compared the one recorded with the semiconductor detector was easier to interpret, due to the higher energy resolution of the semiconductor detector. Also, in favor of the semiconductor detector was its ability to handle high count rates better than the scintillation detector. Therefore, measurements presented in this chapter were recorded using the semiconductor detector.

6.2.1 Liquid host

As mentioned in Section 4.5, the available samples consisted of cadmium, caesium, platinum and lead. The recorded emission spectra of the Andrex SMART 200 X-ray tube, see Figure 4.3, indicate that the energy region with highest intensity ranges from approximately 25 keV to 70 keV. The critical excitation energies of the K shell for platinum and lead are 78.4 keV and 88.0 keV, respectively. In other words the Andrex tube is not the ideal tube for excitation of platinum and lead. Measurements were performed on two samples with 1 000 ppm concentration of platinum and lead. The recorded spectra were integrated over 10 minutes, but no fluorescence lines from either platinum or lead could be distinguished from the continuum.

The critical excitation energies of the K shell for cadmium and caesium are 26.7 keV and 40.0 keV, respectively. These energies are in the lower end of the X-ray tube's highest intensity region, therefore the Andrex tube is well suited to ionize these two species. Measurements were then conducted on the cadmium and caesium samples with different specie concentration. The integration time was set to 10 minutes, and the tube current and voltage were 0.5 mA and 200 kV, respectively. These measurements are presented in Figures 6.2 and 6.3.

In the two figures fluorescence peaks from the K_{α} lines of cadmium and caesium can clearly

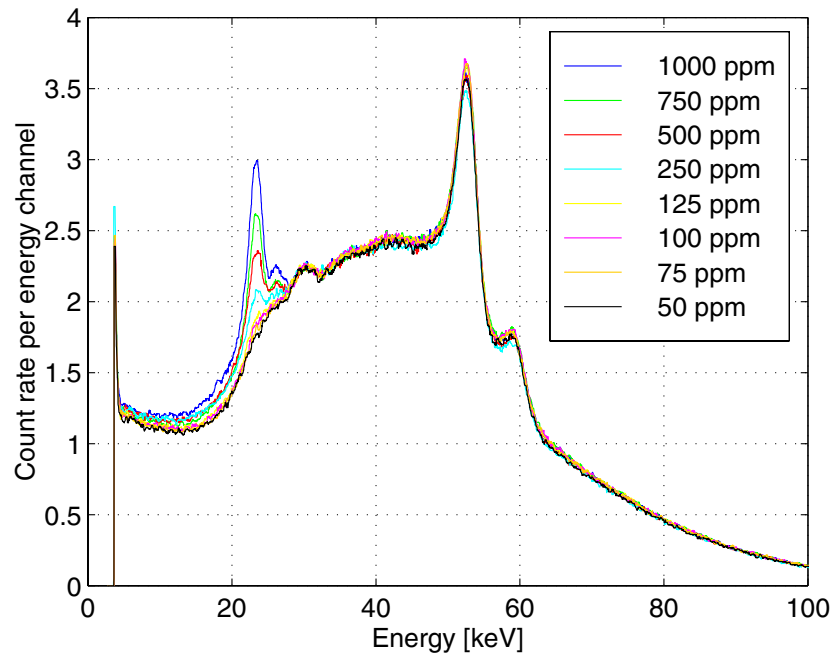


Figure 6.2 Recorded spectra from cadmium samples. Integration time: 10 minutes. Tube current: 0.5 mA. Tube voltage: 200 kV.

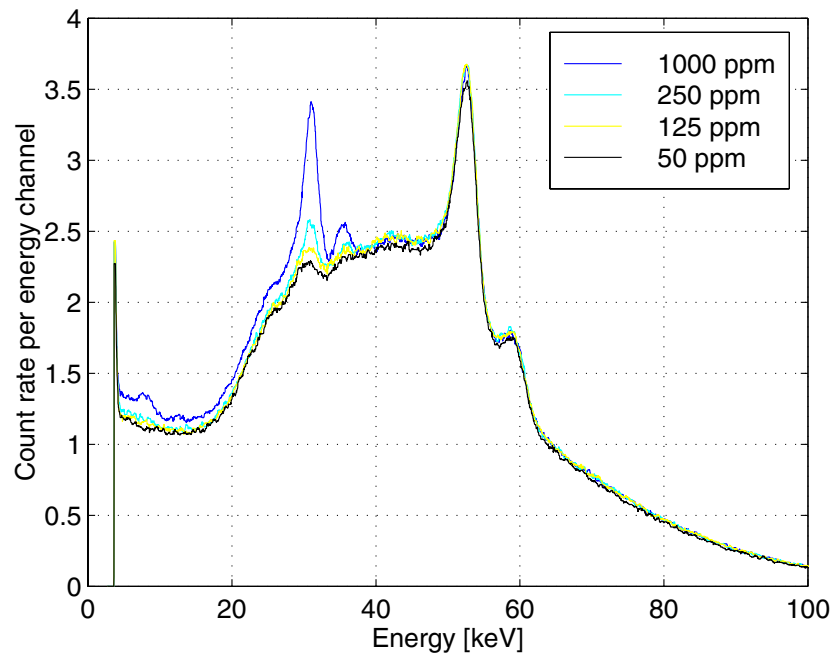


Figure 6.3 Recorded spectra from caesium samples. Integration time: 10 minutes. Tube current: 0.5 mA. Tube voltage: 200 kV.

be identified for specie concentrations in the range from 250 ppm to 1 000 ppm. The K_{β} lines of caesium can also be identified for the same concentration range.

According to the mathematical model developed in Section 3.2, there will be a linear relationship between specie concentration and intensity of the fluorescent radiation. The peak area under the fluorescent peaks were determined using two different techniques for estimating the influence of the continuum:

- Linear interpolation between the continuum values on either side of the peak.
- Subtraction of the continuum area from a sample of distilled water.

The resulting peak areas for cadmium and caesium, estimated using both methods, are presented in Figures 6.4 and 6.5.

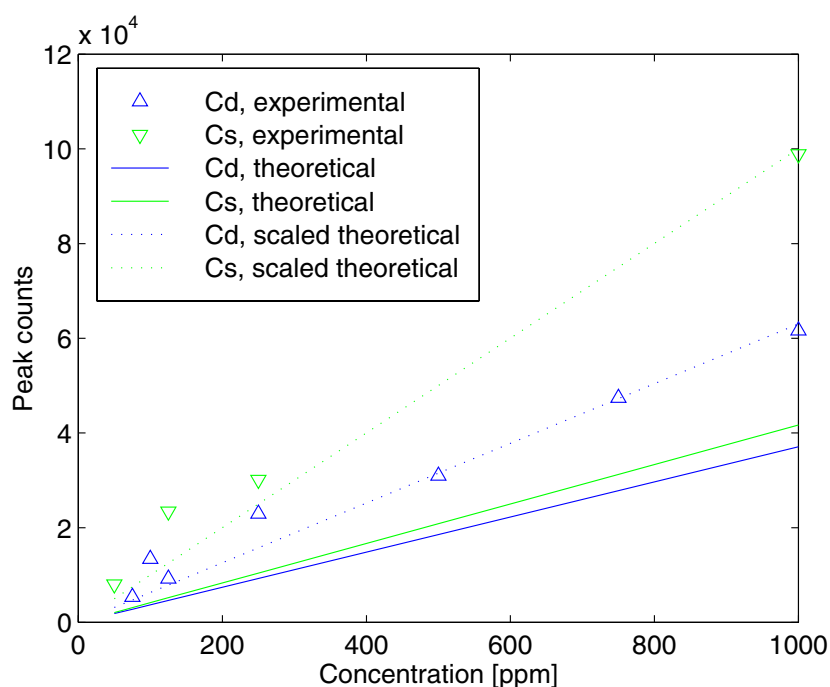


Figure 6.4 Peak counts versus concentration. Peak area determined using linear interpolation between the continuum values on either side of the peak.

By applying the mathematical model from Section 3.2 and numerical integration of the estimated incident radiation spectra, theoretical fluorescence peak counts versus specie concentration were obtained. The results from these calculations are also presented in Figures 6.4 and 6.5. Comparing the experimental to theoretical results it is evident that they deviate from each other to some extent. The deviation can be explained by taking the following points into consideration:

Incident radiation: The incident radiation spectrum that was used in the calculations can only be considered to be an estimate of the true spectrum, see Section 4.3.2.

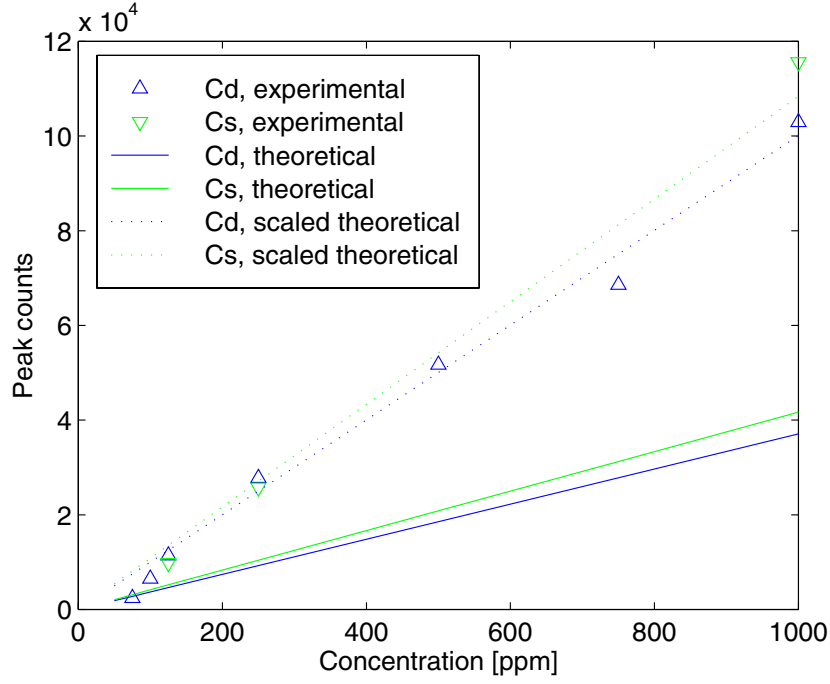


Figure 6.5 Peak counts versus concentration. Peak area determined by subtraction of continuum area from a sample of distilled water.

Mathematical model: Approximations have been used regarding calculation of the solid angle, and absorption of incident and fluorescent radiation in the voxel.

Collimation: Due to the distance from source collimator to sample, the beam incident on the sample surface will be wider than $3 \times 3 \text{ mm}^2$. This increases the voxel volume and thereby also the intensity of the fluorescent radiation that reach the detector.

For each specie and peak determination method, dotted lines in Figures 6.4 and 6.5 represent the results obtained from the theoretical model scaled by a factor to better fit the experimental data.

Consider the samples containing $C_s = 1000 \text{ ppm}$ cadmium and caesium, which give a peak area of $N_{sCd} = 332194$ and $N_{sCs} = 631350$ and a background of $N_{0Cd} = 229274$ and $N_{0Cs} = 515749$, respectively, after 10 minutes integration time. From Equation 3.26, the theoretical absolute limits of detection are then

$$C_{L_{Cd}} = C_s \cdot 4 \cdot \frac{\sqrt{N_{0_{Cd}}}}{N_{s_{Cd}} - N_{0_{Cd}}} = 1000 \cdot 4 \cdot \frac{\sqrt{229274}}{332194 - 229274} \text{ ppm} = 22.4 \text{ ppm} \quad (6.1)$$

and

$$C_{L_{Cs}} = C_s \cdot 4 \cdot \frac{\sqrt{N_{0_{Cs}}}}{N_{s_{Cs}} - N_{0_{Cs}}} = 1000 \cdot 4 \cdot \frac{\sqrt{515749}}{631350 - 515749} \text{ ppm} = 24.8 \text{ ppm} \quad (6.2)$$

Indicating a practical lower limit of detection, $3C_L$, of 67.2 ppm for cadmium and 74.5 ppm for caesium, with an accuracy of $\pm 33\%$. Comparing these results to the recorded spectra these limits seem to be too optimistic. The acquired spectra in Figures 6.2 and 6.3 indicate a lower limit of detection of approximately 250 ppm, which is closer to $6C_L$.

6.2.2 “Gaseous” host

Liquid samples can readily be prepared from standards, but when it comes to preparing samples for analysis of specie concentration in a gaseous host, no simple solution was found.

The one method of simulating a specie in a gaseous host that was used in this study, incorporated saturating a piece of sponge in the standard solution, and leaving it to dry. By using this method the actual concentration of the specie was unknown, and only two different concentrations could be achieved: saturated and left to dry, and saturated, squeezed and left to dry. Eight sponges were prepared for the four different species available. The sponge material had a density of 28.4 kg/m^3 , and was cut up into small pieces with dimensions of approximately $15 \times 15 \times 15 \text{ mm}^3$. The eight measurements are presented in Figure 6.6, the integration time was 10 minutes and tube current and voltage was 4.0 mA and 200 kV, respectively.

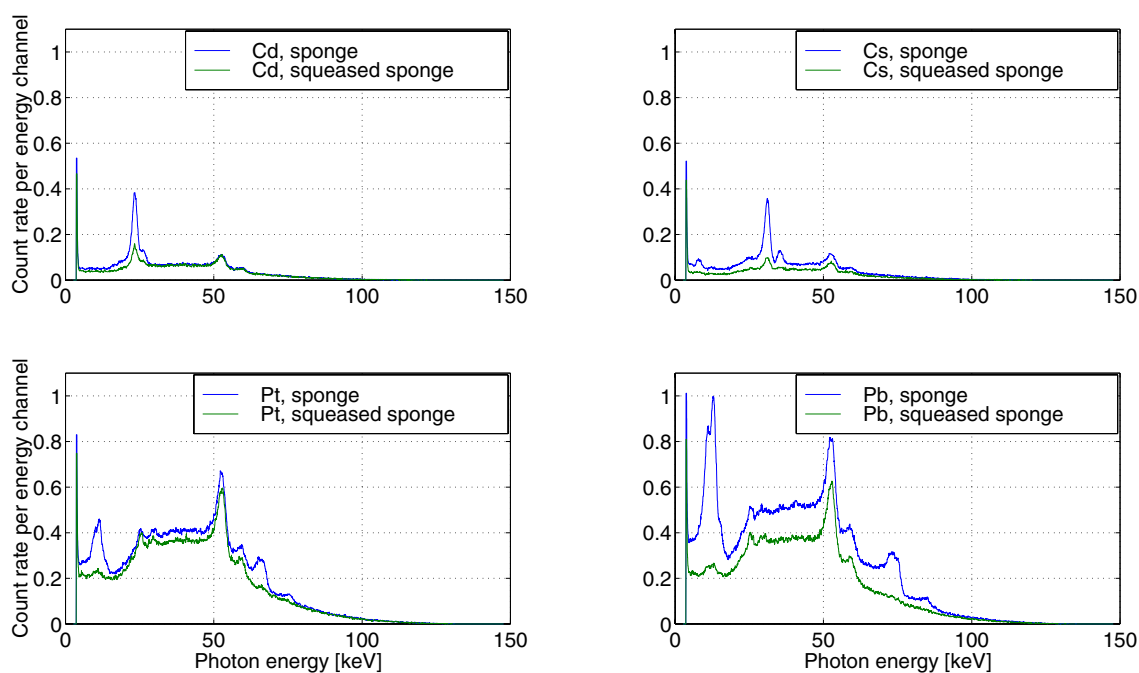


Figure 6.6 Recorded spectra from the sponge samples. Integration time: 10 minutes. Tube current: 4.0 mA. Tube voltage: 200 kV.

Generally, the recorded spectra show that the count rate of the continuum was reduced substantially, due to the lower density of the host material. This effect can be quantified by investigating the ratio of the peak and continuum count rates for the cadmium and caesium samples in

both liquid and gaseous hosts, see Table 6.1. The peak to continuum ratio improves with a factor of approximately 3 and 4 for the caesium and cadmium samples, respectively.

Table 6.1 Peak to continuum ratios for the 1 000 ppm liquid and non-squeezed cadmium and caesium samples.

Specie	Liquid host count rates			Gaseous host count rates		
	Peak	Continuum	Ratio	Peak	Continuum	Ratio
Cd	230	41	5.6	1 796	1 277	1.4
Cs	215	45	4.8	2 038	1 376	1.5

The lower density also results in less attenuation of both incident and fluorescent radiation, which is favorable. Though, it should be kept in mind that the low density of the host allowed operation of the X-ray tube at a higher current, without introducing problems with pulse pile-up in the amplifier and high dead time in the PHA.

Comparison of the recorded spectra reveal that the samples with platinum and lead generate more scattered radiation than the cadmium and caesium samples. This is a result of higher densities in the samples with species of platinum and lead compared to those with cadmium and caesium.

Also, fluorescent lines from platinum and lead can clearly be distinguished from the continuum. Especially, the L_{α} and L_{β} lines are much stronger than the K_{α} and K_{β} lines. This latter effect can be explained by the shape of the incident spectra. The intensities of photons which are more energetic than the critical excitation energy is higher for the L level compared to the K level.

6.2.3 Voxel position within the sample

Measurements in this section were focused on investigating changes in the recorded spectra when the location of the voxel in the sample box was altered. The motivation behind these measurements was to verify whether the penetration or escape depth is most critical regarding the intensity of fluorescent radiation that reach the detector. Two measurement series were carried out:

- Increased penetration depth, x , in the sample for incident radiation, see Figure 6.1.
- Increased escape depth, y , from the sample for radiation viewed by the detector, see Figure 6.1.

Increased penetration depth was achieved by moving the sample nearer to the radiation source, and increased escape depth was achieved by moving both the sample and the detector away from the incident radiation beam. Spectra were recorded in 5 mm steps for both series. Integration time was 10 minutes, tube voltage 200 kV and current 0.5 mA. The results are presented in Figures 6.7 and 6.9 for a sample containing distilled water, and in Figures 6.8 and 6.10 for a sample with 1 000 ppm cadmium.

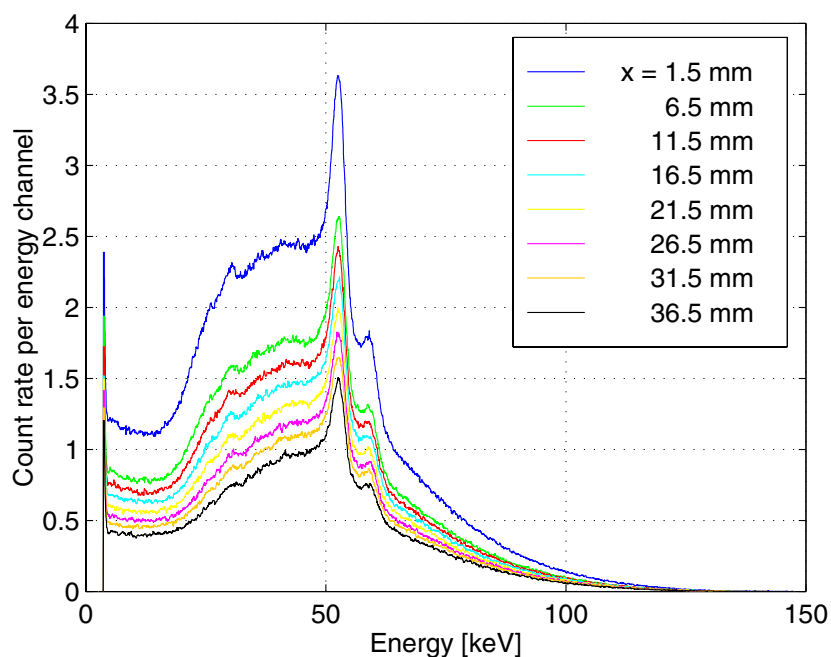


Figure 6.7 Count rate versus energy channel and increased penetration depth, x , for radiation incident on the sample. Sample: distilled water. Tube voltage: 200 kV. Tube current: 0.5 mA. Integration time: 10 minutes.

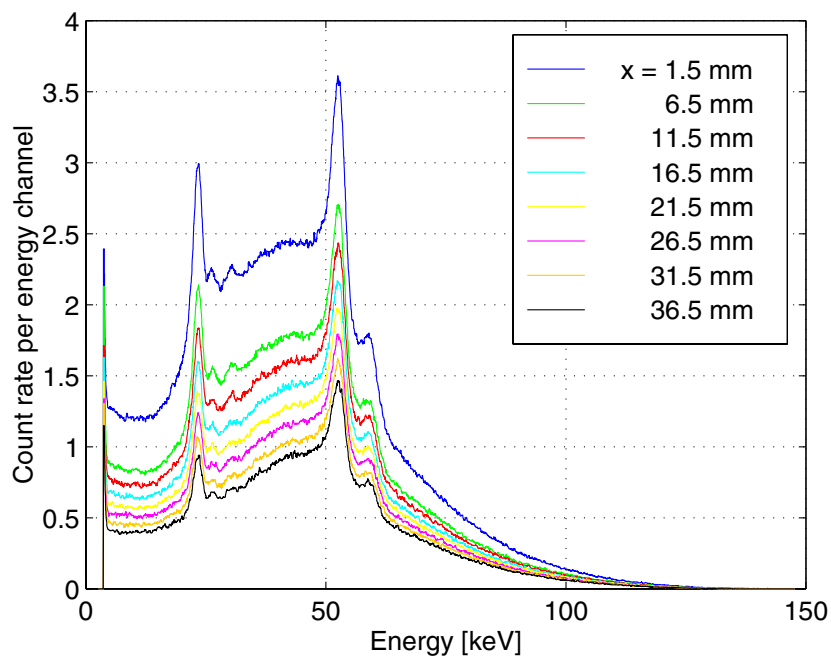


Figure 6.8 Count rate versus energy channel and increased penetration depth, x , for incident radiation on the sample. Sample: Cd 1000 ppm. Tube voltage: 200 kV. Tube current: 0.5 mA. Integration time: 10 minutes.

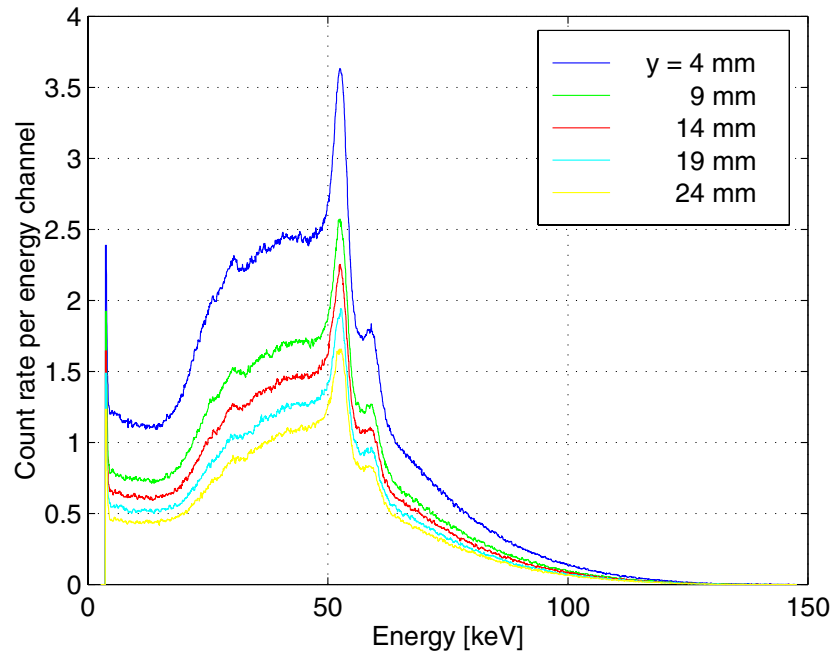


Figure 6.9 Count rate versus energy channel and increased escape depth, y , for radiation viewed by the detector. Sample: distilled water. Tube voltage: 200 kV. Tube current: 0.5 mA. Integration time: 10 minutes.

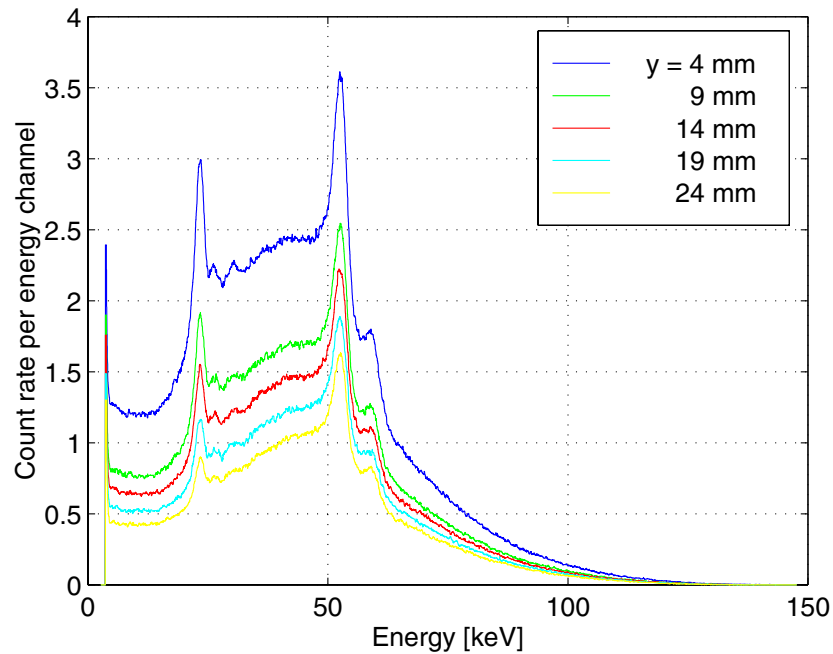


Figure 6.10 Count rate versus energy channel and increased escape depth, y , for radiation viewed by the detector. Sample: Cd 1000 ppm. Tube voltage: 200 kV. Tube current: 0.5 mA. Integration time: 10 minutes.

Except from higher attenuation in the lower energy range of the spectrum, increased penetration or escape depths have only a small influence on the shape of the continuum for the scattered radiation.

The effect of increased penetration depth, x , for the ionizing radiation is less prominent compared to the effect of increased escape depth, y , for the fluorescent radiation with respect to the intensity of fluorescent radiation that reach the detector. This is because the attenuation of fluorescent radiation is higher per unit path length, than for the ionizing radiation. These effects are also illustrated in Figure 6.11, where the peak area of K_{α} emission from a sample containing 1 000 ppm cadmium is plotted as a function of both penetration and escape depths. By applying the mathematical model from Section 3.2 and numerical integration of the estimated incident radiation spectra, theoretical fluorescence peak counts versus penetration and escape depth were obtained. The results from these calculations are also presented in Figure 6.11. The difference between the experimental and theoretical results can be explained by the same arguments as in Subsection 6.2.1.

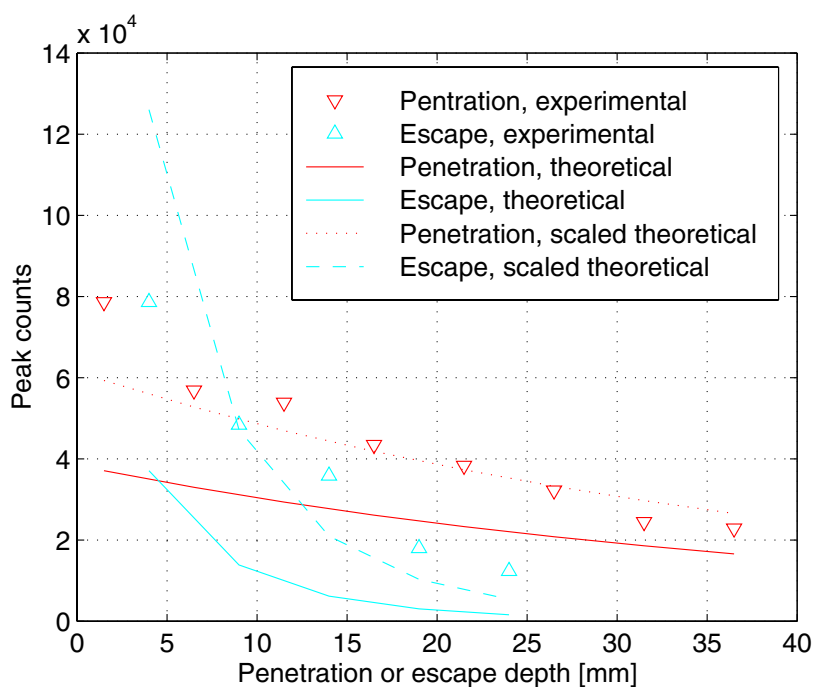


Figure 6.11 Influence of penetration and escape depth on K_{α} fluorescent peak area. Sample: Cd 1 000 ppm. Tube voltage: 200 kV. Tube current: 0.5 mA. Integration time: 10 minutes.

For both increased penetration and escape depths dotted lines in Figure 6.11 represent the results obtained from the theoretical model scaled by a factor to better fit the experimental data.

This verifies that in an optimized measurement system based on an X-ray source, it is more important to reduce the escape depth for fluorescent radiation than the penetration depth for ionizing radiation.

Chapter 7

Discussion

In this project several factors that govern the performance of an on-line instrument using X- or gamma-ray stimulated fluorescence analysis have been investigated.

7.1 Radiation sources

X- and gamma-ray sources have some practical differences regarding their use in this study. Gamma-ray sources provide radiation of discrete energies, whereas X-ray sources provide a continuous radiation spectrum, on which characteristic lines of the anode material are superimposed.

The nearly monochromatic characteristic character of most gamma-ray sources make them advantageous for selective excitation of elements, though the availability of different gamma-ray energies are limited. For X-ray tubes the polychromatic emission spectra can be tuned to obtain optimal conditions for fluorescence from specific elements. The emission spectra can be varied through the tube voltage and current settings, choice of anode material and radiation window.

The output intensity of an X-ray tube is typically 10^{12} photons/s per steradian, whereas the intensity of a gamma-ray source is limited to about 10^7 photons/s per steradian [7]. With the geometrical arrangements used here to measure fluorescence a very strong excitation source is needed, which is in favor of X-ray tubes. Though, the X-ray tubes used here do not have the required intensity above the critical excitation energy for excitation of high Z elements. Higher acceleration voltage is then needed.

The stability of the radiation intensity emanating from the source will influence on the accuracy of the measurement. Radioactive isotopes provide good stability when monochromatic sources are required. Fluctuations and drift in the beam intensity of X-ray tubes occur due to unstable power supply voltage. A 5–10% ripple in the intensity of the X-ray beam with a frequency of about 300 Hz has been reported [18, 19]. Stability measurements performed on the Balteau Baltospot GFD-165 X-ray tube indicate intensity fluctuations in the range of 0.5–8% over the entire operational region. The region of best stability for the Baltospot GFD-165 X-ray tube is for maximum tube current and high voltage in the range 130–150 kV.

The emission spectra of the X-ray tubes have been estimated through experimental techniques. Though, the accuracy is fairly limited because of several factors. Due to count rate

limitations of the detector systems available the emission spectra were recorded after being scattered 90° through a sample of distilled water. This method makes it necessary to correct the energy deposited in the detector for the energy transfer between the incident photon and the recoil electron (Compton scattering). In addition the probability of Compton scattering will vary over the incident photons' energy range, thus introducing a distortion in the recorded spectra. Further a correction to the intensity is required, because only a fraction of the scattered radiation is viewed by the detector. The scaling factor found in this work is inaccurate because it is based solely on measurements for one energy, however is still applicable for estimation purposes.

7.2 Radiation detection

The two different detectors available had quite different properties. The semiconductor detector has in this study presented better results than those obtained from the scintillation detector. This difference originates from properties of the detectors such as energy resolution, crystal size and count rate limitations.

Energy resolution will govern the detector's ability to discriminate between close lying energies and reject scattered radiation. The energy resolution of the detectors was experimentally determined to be 3% and 11% for the semiconductor and scintillation detectors, respectively. The energy resolution needed will increase with the number of species present in the sample, Therefore the energy resolution of the scintillation detector can be sufficient for samples containing only a few species with well separated emission lines.

Crystal size will influence on the detector stopping power, background count rate and the input area of the detector. The stopping power of the scintillation detector is superior to the semiconductor, due to its large volume. Still, both detectors have proved to provide sufficient stopping power for the energy range of interest. Large crystals will have a higher background compared to smaller crystals, this can be a problem when measuring on low count rate systems such as the set-up for absolute fluorescence yield measurements. For the application of the scintillation detector to absolute fluorescence yield measurements a detector with a smaller crystal might have improved the results. The surface area of the detector proved to be an important factor with the measurements on the surface of samples with submerged radiation source. By using a detector with face area larger than the semiconductor's, but smaller than the scintillation detector's, might have given better measurement results. The count rate could then have been controlled through the area of the detector's face. For scintillation detectors a variety of crystal sizes and shapes can easily be obtained, but for semiconductor detectors size is a limiting factor. Though, a pixellized matrix of semiconductor detectors with multi channel read-out ASIC electronics could be used to increase the effective area of the detector. Count rate limitations proved to be important factor. Especially for the measurements on liquid specimens, because their higher density will generate more scattered radiation than the "gaseous" samples which are less dense.

Count rate limitations of the scintillation detector ruled it out for use on liquid samples, but it might have a potential for use on gaseous samples. The semiconductor detector could handle higher count rates than the scintillation detector and was therefore the preferred detector for

measurements on liquid hosts ionized by radiation from the X-ray tube.

7.3 X-ray fluorescence measurements

Fluorescence measurements have been performed using both radioactive isotopes and X-ray tubes as sources of ionizing radiation.

Measurements utilizing gamma-rays for ionization of the samples have been applied to measurements of absolute and relative fluorescence yield. The measurement results from absolute fluorescence yield did not contain any usable information to determine the fluorescence yield through application of the developed mathematical model. Results over a limited specie concentration range were obtained for the relative fluorescence yield measurements with the gamma-ray source submerged into the sample. Though, the feasible range may extend to higher concentrations than tested in this study.

Measurements utilizing X-rays for ionization of the samples have been applied to measurements of fluorescence from both liquid and “gaseous” samples. These measurements have given the best result judged by the fluorescent peak area. Comparison of the measurements from these two sample types show that measurements on “gaseous” samples give a better peak to continuum ratio, which also was expected because of a less dense host. Effects of different penetration and escape depths for incident and fluorescent radiation were also investigated for a liquid host. The results from these measurements confirm that for an optimized system it is more important to reduce the escape depth for fluorescent radiation than the penetration depth for ionizing radiation.

Relating the measurement results to the mathematical model proved to be difficult for both sample types. For the “gaseous” samples the concentrations were unknown, and therefore theoretical results could not be compared to experimental results. On the other hand the specie concentrations of the liquid samples were known. The theoretical results calculated for the liquid samples underestimated the fluorescence yield and overestimate the practical detection limits. Factors that can explain the deviation between the experimental and theoretical results are uncertainties regarding the accuracy of the estimated incident radiation spectrum, influence of approximations used in the mathematical model and source to sample distance.

Effects of different penetration and escape depths for incident and fluorescent radiation were also investigated for a liquid host. The results from these measurements confirm that for an optimized system it is more important to reduce the escape depth for fluorescent radiation than the penetration depth for ionizing radiation.

Chapter 8

Conclusions

Measurement results and data analysis show that it is possible to measure specie concentrations in both liquid and “gaseous” hosts.

Gamma-ray sources versus X-ray tubes

Based on the results obtained through measurement in this work the X-ray tube is found to be the best source of ionizing radiation for measurements of X-ray fluorescence from liquid hosts. It should also be kept in mind that the X-ray tubes available in this study were not optimized for X-ray fluorescence measurements. Though, gamma-ray sources can be used to measure on open surfaces of liquid samples over a limited concentration range. Measurements on both liquid and gaseous samples have only been performed with an X-ray tube as the source of the ionizing radiation, with best result for the latter sample type. Therefore measurements with ionizing radiation from gamma-ray sources on gaseous samples should yield better results than for liquid samples.

Scintillator versus semiconductor detectors

The semiconductor detector has provided better measurement results than the scintillation detector, because of its better energy resolution and ability to handle higher count rates. This conclusion is based on measurements on liquid hosts only. The problems related to the count rate limitations of the scintillation detector can possibly be reduced when measuring on gaseous hosts, due to less scattered radiation. Therefore X-ray fluorescence measurements on gaseous samples with both detector types should yield good results, but this is also dependent on the complexity of the sample matrix.

Liquid versus gaseous host measurements

Measurements on known specie concentrations have only been performed on liquid samples, with good results in the concentration range 500–1 000 ppm. In contrast to this, measurements on “gaseous” hosts have only been performed without knowledge of the concentrations the two methods of preparation of the sponges gave. Comparison of the recorded spectra for both liquid

and “gaseous” hosts reveal less scatter and larger fluorescence peak areas for the “gaseous” samples compared to the liquid samples. The conclusion is then that measurements on gaseous hosts should be possible yielding better results, and resulting in feasibility over a larger concentration range than for liquid hosts.

Feasibility

This study has shown that measurements of X-ray fluorescence from both liquid and gaseous samples are possible with either radiation from gamma- or X-ray sources. The best performance has been obtained for “gaseous” hosts with an X-ray tube as radiation source and semiconductor detector for readout. Measurements on gaseous hosts should also be feasible with readout of fluorescent radiation, through the scintillation detector generated with either gamma- or X-ray sources. The combination of a liquid host and ionization through use of gamma-ray sources have been proved to have a very limited range of detection.

The results of this study predicts that the feasibility of the X-FAPT measurement principle will be restricted to measurements on species in gaseous hosts. In addition, the low flux of the fluorescent radiation limits the system’s speed of response. Therefore, measurements on the dynamic behavior of a process will not be feasible, but a time average of the chemical distribution in the measurement cross section can be obtained.

Chapter 9

Suggestions for further work

Further investigation of the emission spectra from X-ray tubes should be carried out in order to determine the spectra with a higher degree of accuracy. This can be done with either a wavelength dispersive system in which the radiation from the X-ray tube is allowed to fall directly on the analysing crystal, or with a energy dispersive system capable of handling very high count rates.

The X-ray tubes used in this study provided a maximum acceleration voltage of 200 kV. This acceleration voltage is sufficient to ionize low and medium Z elements, but does not provide the intensity needed in the upper energy range of the emission spectrum to ionize high Z elements. Therefore measurements should be carried out on high Z species in both liquid and gaseous hosts with an X-ray tube that can provide higher acceleration voltages. The X-ray tube should allow the use of a radiation window (filter) to minimize output of bremsstrahlung radiation below the critical excitation energy. This filtering technique will reduce the background in the spectra, which is mainly produced by Compton scattering of incident radiation from the sample, and thereby reduce the problems of saturation in the amplifier chain and PHA.

X-ray fluorescence have been successful on detecting medium Z species in both liquid and gaseous hosts. Gaseous hosts have also provided the best fluorescence yield, therefore an effort should be put into developing an experimental set-up that can enable measurements on known concentrations of species in a gaseous host. Measurements on such an arrangement should be carried out with both gamma- and X-ray sources.

The mathematical model for calculations of X-ray fluorescence intensities developed in this study contain approximations with regard to calculations of the fraction of the radiation that is absorbed in the voxel, relative attenuation by the host medium of fluorescent radiation within the voxel and solid angle subtended by the detector collimator at the voxel. Development of an accurate mathematical model should result in better agreement between the theoretical and experimental results, and can therefore be used to better estimate the performance of an X-ray fluorescence measurement system.

Bibliography

- [1] Jaklevik, J M and Walter R L, *X-ray fluorescence of environmental samples*, Ann Arbor Sci. 63 (1977).
- [2] M^cCann H and Johansen G A, *X-ray Fluorescence Autoprojection Tomography (X-FAPT)*, University of Manchester, Institute of Science and Technology and University of Bergen, Department of Physics (1999) Internal report.
- [3] Johansen G A, *Industrial applications of nuclear radiation*, Department of Physics, University of Bergen (1994) Internal report/compendium No. 1994–03.
- [4] Knoll G F, *Radiation Detection and Measurement Second Edition*, John Wiley & Sons (1989) ISBN 0–471–81504–7.
- [5] *PhotCoef*, AIC Software Inc., P.O. Box 544, Grafton, MA 01519, USA. WWW: <http://www.photcoef.com>. E-mail: photcoef@aol.com.
- [6] Evans R D, *The Atomic Nucleus*, M^cGraw-Hill Book Company (1955).
- [7] Tertian R and Claisse F, *Principles of Quantitative X-Ray Fluorescence Analysis*, Heyden & Son (1982) ISBN 0–85501–709–0.
- [8] Tsoulfanidis N, *Measurement and Detection of Radiation Second Edition*, Taylor & Francis (1995) ISBN 1–56032–317–5.
- [9] *Instruction manual TC 244 amplifier*, Tennelec INC, 601 Oak Rigde Turnpike, PO Box 2560, Oak Rigde, TN 37831–2560.
- [10] *Instruction manual PCA-Multiport-E/R Version 2.42* Oxford Instruments Inc, Nuclear Measurement Group, 601 Oak Rigde Turnpike, PO Box 2560, Oak Rigde, TN 37831–2560.
- [11] Johnson G W, *LabVIEW Graphical Programming*, M^cGraw-Hill series on visual technology, M^cGraw-Hill Inc., (1994).
- [12] Pedersen H, *Development of a measuring table for industrial gamma tomography* (in Norwegian), Cand. scient. thesis, Department of physics, University of Bergen (1996).

BIBLIOGRAPHY

- [13] Johansen G A, Frøystein T, Pedersen H and M^cKibben B, *A Flexible Test Platform for Investigating Gamma-ray Tomography Geometries and Applications*, Proc. Frontiers in Industrial Process Tomography II, Delft, The Netherlands, 8–12 April (1997) pp. 365–369.
- [14] *Model 485 Autoranging Picoammeter Instruction Manual*, Keithley Instruments INc., Instrument Division, 28775 Auroa Road, Cleveland, Ohio 44139, USA.
- [15] *Recommendation for data on shielding from ongiong radiation Part 2. Shielding from X radiation*, British Standard 4094 Prt 2 (1971).
- [16] Bearden J A, *Rev. Mod. Phys.* 39, 78 (1967).
- [17] *CRC Handbook of Chemistry and Physics*, edition 1995–1996, CRC Press Inc (1995).
- [18] Wentz, L B, Neal L G and Wright, R W, *X-ray Measurement of Void Dynamics in Boiling Liquid Metals*, Nuclear Technology, Vol. 4 pp. 347–355 (1968).
- [19] Smith, A V, *A Fast Response Multi-Beam X-ray Absorption Technique for Identifying Phase Distributions During Steam-Water Blowdowns*, Journal of British Nuclear Energy Society, Vol. 14 pp. 227–235 (1975).

Part III
Appendix

Appendix A

Pictures of components in the measurement system

A.1 Collimators



Figure A.1 Collimator for absolute fluorescence yield measurements.



Figure A.2 Collimator for relative fluorescence yield measurements, with source above the sample surface.

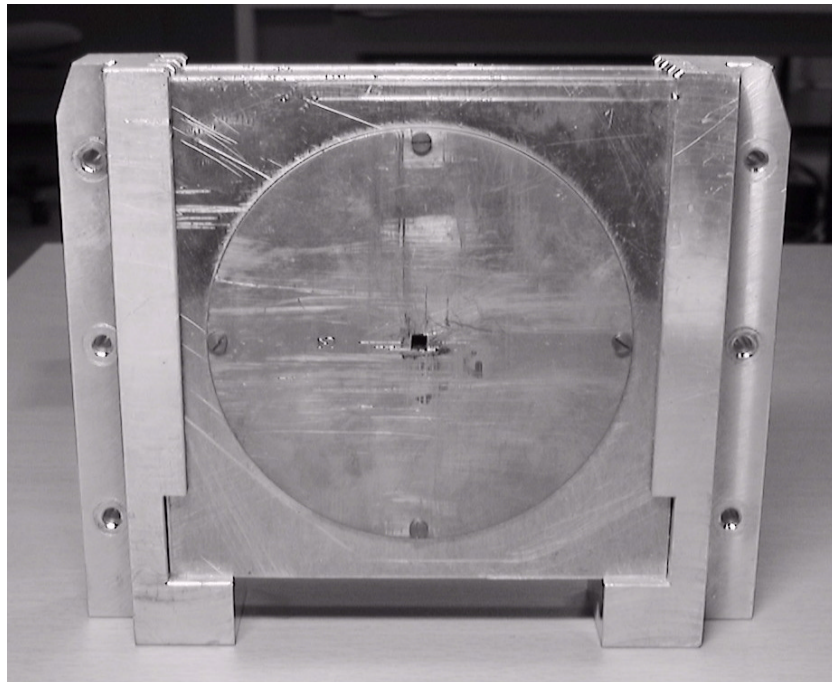


Figure A.3 X-ray tube collimator.

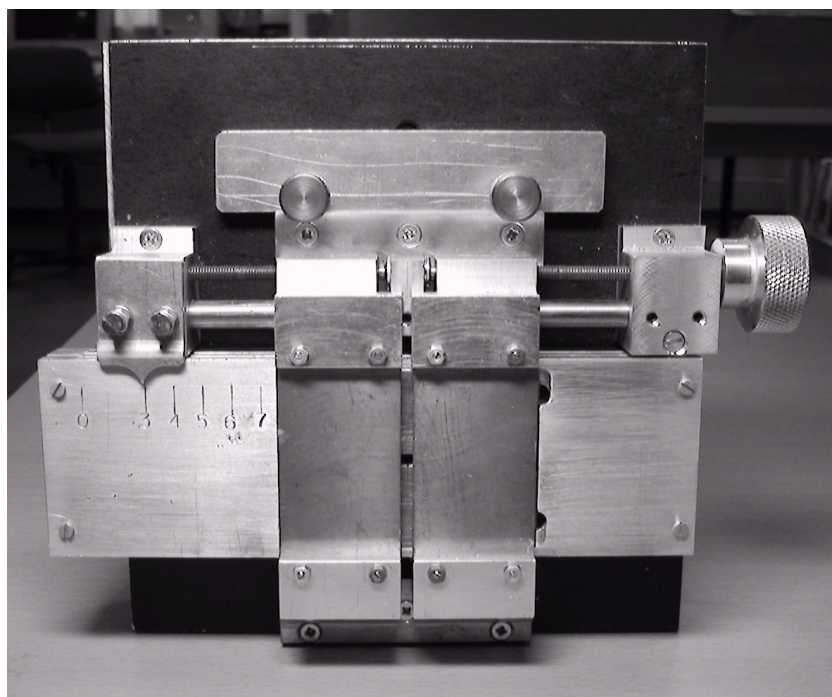


Figure A.4 Detector collimator.

A.2 Radiation shields



Figure A.5 Detector shields. Left: Three layer shield (Pb, Cu and Sn) for the scintillation detector. Middle: Two layer shield (Al and Pb) for the scintillation detector. Right: Lead shield for the semiconductor detector.



Figure A.6 Lead enclosure, exterior.

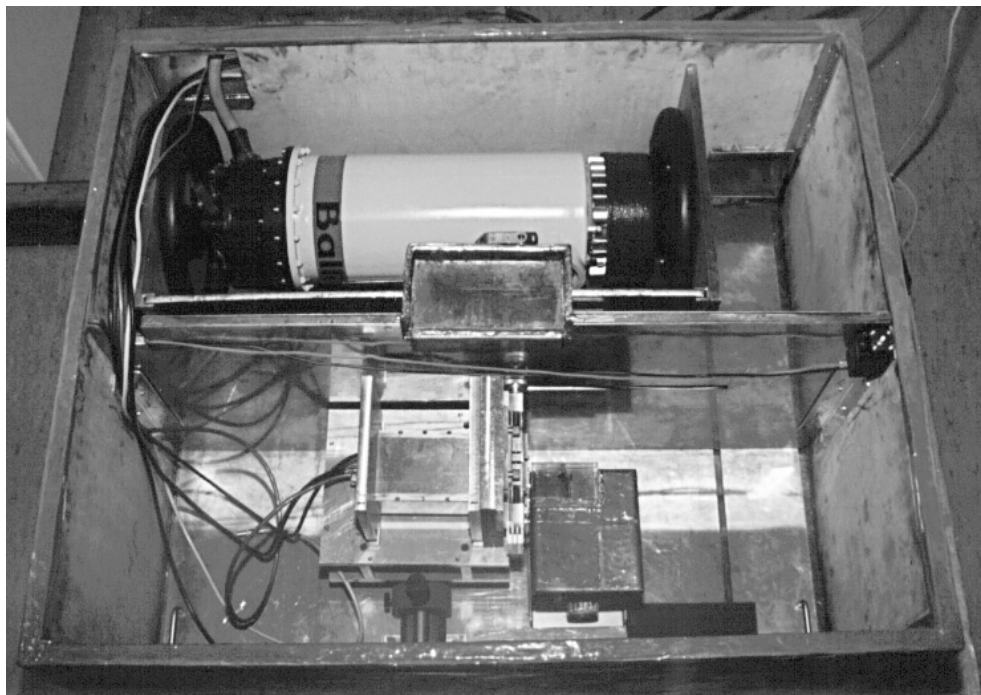


Figure A.7 Lead enclosure, interior.

Appendix B

Technical specifications

B.1 Scionix scintillation detector



Figure B.1 Scionix 51B51/2-HV-EP scintillation detector with integrated high voltage power supply and charge sensitive preamplifier.

Scionix Engineering Note 9506001

Subject: Specifications 51 B 51 / 2 - HV - EP
Serial Numbers : SSE 526
Description: Scintillation detector with built-in high voltage power supply (Cockroft Walton type) and charge sensitive preamplifier.

Scintillation crystal : NaI(Tl) 51 mm diameter, 51 mm high .
Crystal read out : 51 mm diameter photomultiplier EMI type 9266
Internal High Voltage generator : Cockroft Walton Type.
High Voltage regulation : by means of potentiometer ("G").
Adjustable between : - 200 - - 1065 V
Recommended Voltage : - 600 - - 700 V

Power requirements : + and - 12 V; 100 mW for HV supply PMT, 400 mW for fast preamplifier (Max).
Maximum input voltage + - 15 V.
An asymmetrical power supply leads to a DC offset on the output signal.
Power can be fetched from NIM crate or other standard laboratory power supply.

Preamplifier : Charge sensitive preamplifier,
Output pulses : Negative (max. 10 V),
Pulse fall time : 50 μ s, suited to feed directly into NIM based or PC board based spectroscopic amplifier.
Output impedance : 50 Ω , long (many tens of m) cable allowed.
(for schematic see below)



Electrical connections : Negative High Voltage circuit (anode at ground potential). Readout at Anode of PMT.

Signal : BNC connector ("S")
 Power : dual LEMO connector, type 0;
 for polarity, see housing, female on chassis part (on detector) is + 12 V, male on chassis part is - 12 V. HV generator and preamplifier are both protected against polarity reversal.

HV regulation : linear precision potentiometer

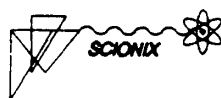
Housing : Aluminum , thickness around crystal 0.5 mm
 Maximum outer diameter : 58 mm
 Total length : 250 mm
 (up to connectors)

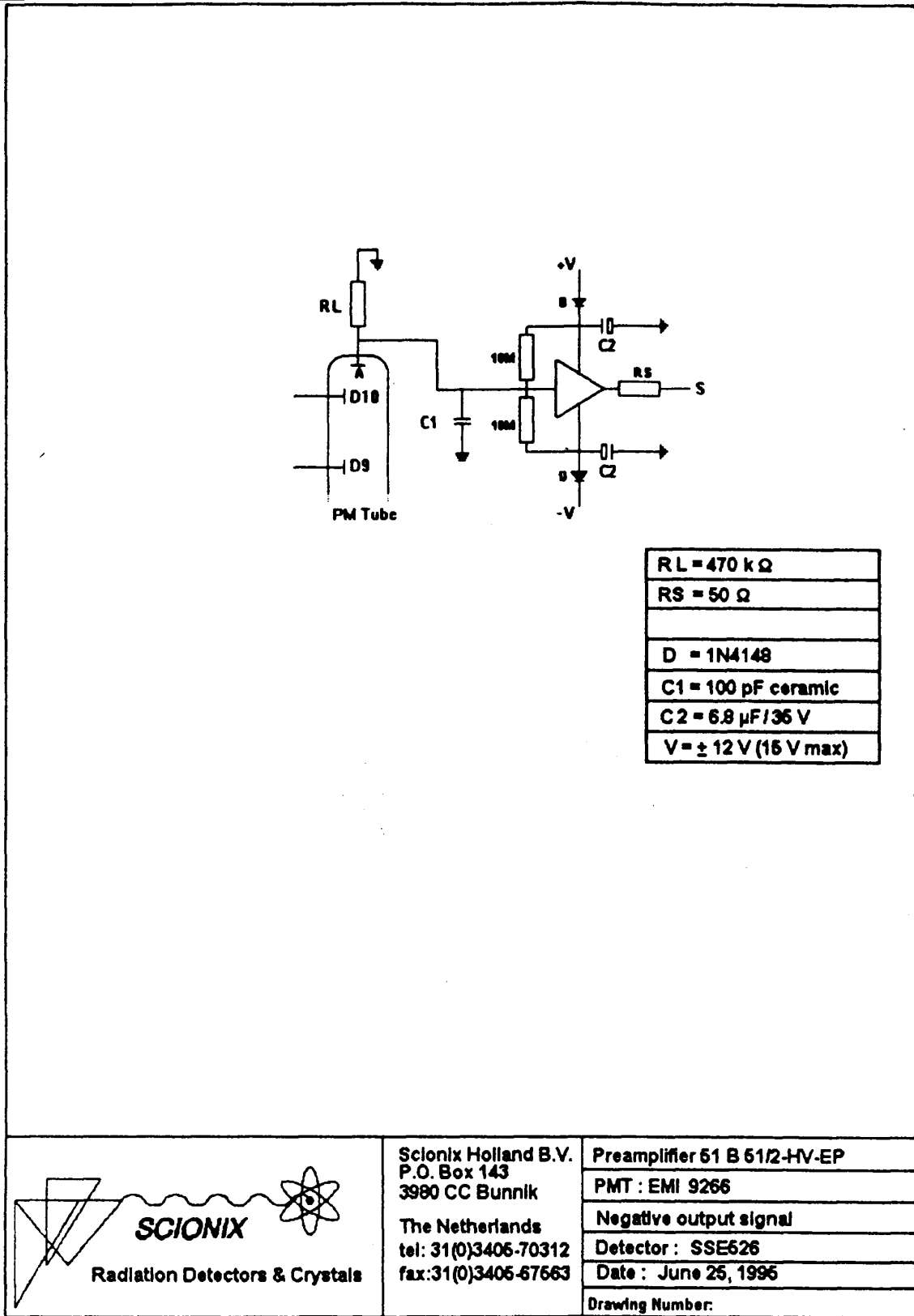
Calibration settings

Factory adjusted high voltage (approx.) : - 700 V
 Factory adjusted gain : - 1.5 V / MeV gamma
 Minimum High Voltage : - 200 V
 Maximum high voltage : -1065 V

Energy resolution : 662 keV : 6.8 % FWHM
 1332 keV : 4.8 % FWHM
 59.5 keV : 11.4 % FWHM

HV generator ripple at - 700 V : 1 keV





B.2 eV semiconductor detector

Mounted directly on the back of a BNC connector, the eV-180 is designed to be plugged on an eV-550 or any standard laboratory charge sensitive preamplifier. The housing comes in 1.25" OD or 0.5" OD, depending on the detector crystal size.



Figure B.2 eV-180 series detector configurations.

CdZnTe (Zn=10%, High Pressure Bridgman grown) for Radiation Detection

- Wide operating temperature range (-30°C to $+70^{\circ}\text{C}$).
- Good energy resolution over a wide energy range (~ 5 keV to 1 MeV).
- High Z (Cd 48, Te 52, Zn 30) and high density (~ 5.78 g \cdot cm $^{-3}$), yields high absorption efficiency.
- Size $3 \times 3 \times 2$ mm 3 .
- Non hygroscopic.
- Chemically stable.

B.3 eV 550 preamplifier, with eV-5093 hybrid circuit

All values measured with preamplifier output unloaded.

Table B.1 eV 550 preamplifier, with eV-5093 hybrid circuit specifications.

Parameter	Value
Source capacitance	0 to 100 pF
Risetime	20 ns
Falltime	1 030 μ s
Sensitivity	3.6 mV/fc
R_f	1 G Ω
C_f	0.4 pF

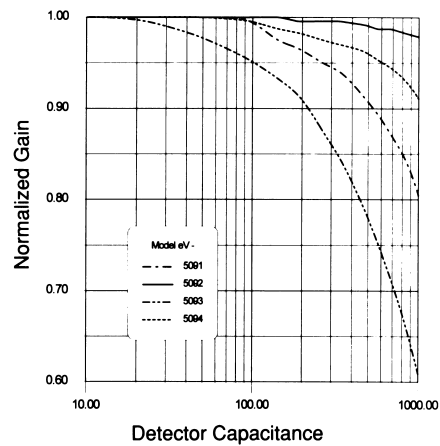


Figure B.3 Normalized gain vs. detector capacitance.

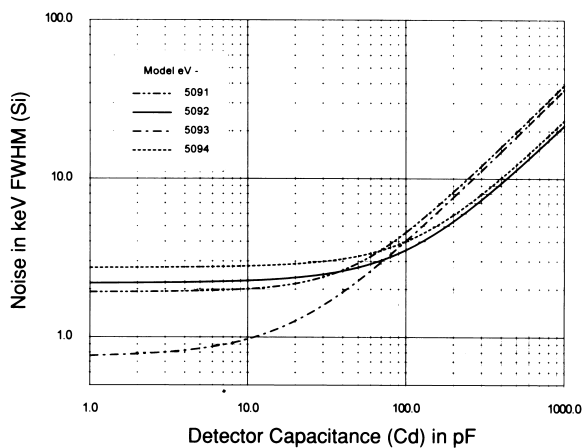


Figure B.4 Noise vs. detector capacitance.

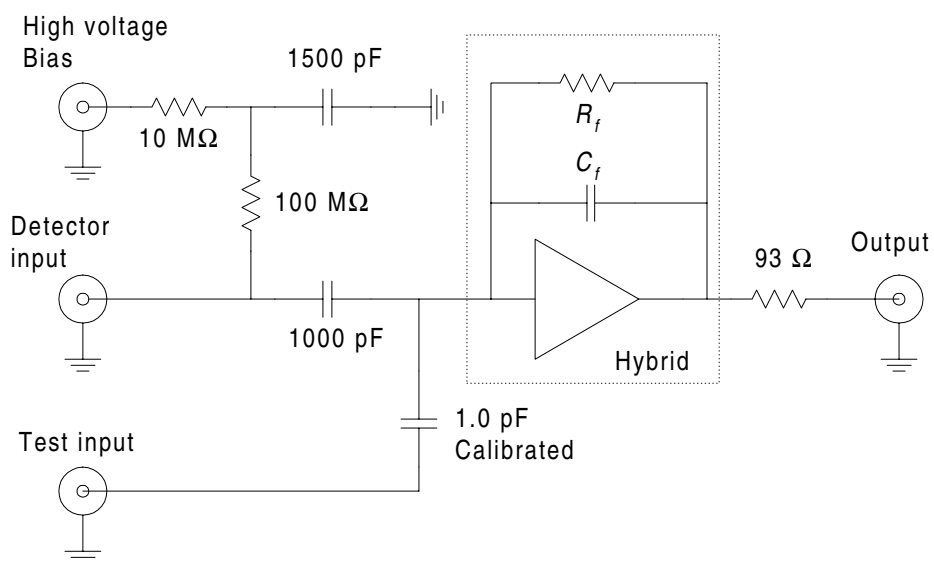


Figure B.5 Circuit diagram for the charge sensitive eV-550 preamplifier.

Appendix C

LabVIEW Virtual Instruments

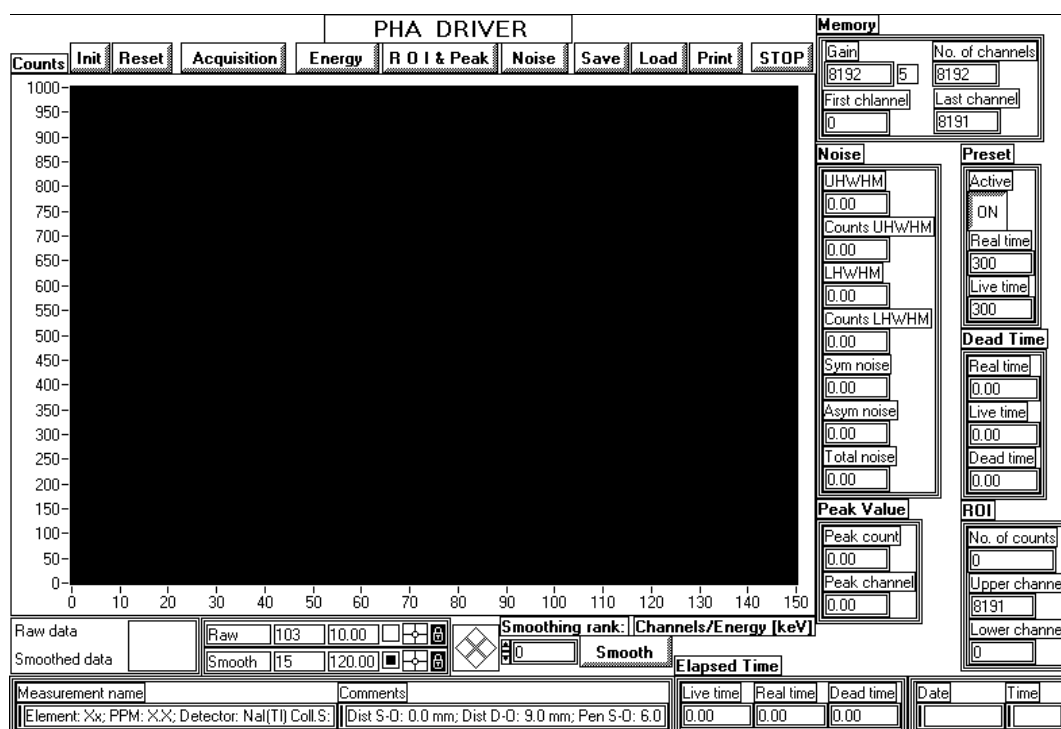
C.1 PHA.vi

PHA.vi

Connector Pane



Front Panel



Controls and Indicators

Acquisition

Start or stop data acquisition.. This control is always active, regardless of acquisition mode (Preset on/off).

Save

Save acquired or loaded data to a tabulator delimited text-file.

The following data will be saved:

- Measurement name.
- Comment.
- Date.
- Time.

SETUP

- Gain.
- First channel.
- Last channel.
- No. of channels.
- Preset on/off.
- Preset real time.
- Preset live time.

ENERGY CALIBRATION

- Coarse gain.
- Fine gain.
- Gradient.
- Intercept.

PULSE SHAPE

- Peaking time.
- Shaping time.

DEAD TIME

- Real time.
- Live time.

- Dead time.

CALCULATION

- Peak channel & counts.
- UHWHM channel & counts
- LHWHM channel & counts.
- Sym noise.
- Asym noise.
- Total noise.

COUNT

- Upper limit.
- Lower limit.
- No. of counts.
- Smooth rank.

TF Noise

Calculate UHWHM, LHWHM channels plus symmetric, asymmetric and total noise.

After clicking this button a new dialogue appears which use the peak channel determined by the 'ROI & Peak' function. Modify the values if appropriate. The cursors in the spectrum cannot be moved while the dialogue is open.

Explanation of abbreviations:

UHWHM:

Upper Half Width Half Maximum.

LHWHM:

Lower Half Width Half Maximum.

Total noise:

The number of channels between UHWHM and LHWHM.

Symmetric noise:

The number of channels between the peak channel and UHWHM multiplied by a factor of two.

Asymmetric noise:

The difference in number of channels between total noise and symmetric noise.

Init

Initialise the Tennelec/Oxford PCA Multiport Multi Channel Analyser: conversion gain, dead time control, preset on/off, memory size and group.

Enter details regarding experimental set-up: measurement name, comments, amplifier gain, peaking and shaping times, energy calibration.

Reset

Resets all the channels of the active memory group to zero. Re-initialises global-variables to default values.

Always reset the PCA and the memory group before recording the first spectrum.

Load

Load a spectrum and its data from a tabulator delimited text-file.

The following data will be retrieved:

- Measurement name.
- Comment.
- Date.
- Time.

SETUP

- Gain.
- First channel.
- Last channel.
- No. of channels.
- Preset on/off.
- Preset real time.

- Preset live time.

ENERGY CALIBRATION

- Coarse gain.
- Fine gain.
- Gradient.
- Intercept.

PULSE SHAPE

- Peaking time.
- Shaping time.

DEAD TIME

- Real time.
- Live time.
- Dead time.

CALCULATION

- Peak channel & counts.
- UHWHM channel & counts.
- LHWHM channel & counts.
- Sym noise.
- Asym noise.
- Total noise.

COUNT

- Upper limit.
- Lower limit.
- No. of counts.
- Smooth rank.

132 Smoothing rank:

This control sets the smooth rank of the median filter.

TF Print

Print the smoothed curve along with the following information:

- Measurement name

- Date

- Time

SETUP

- Gain

- First channel

- Last channel

- No. of channels

- Preset on/off

- Preset real time

- Preset live time

ENERGY CALIBRATION

- Coarse gain

- Fine gain

- Gradient

- Intercept

PULSE SHAPE

- Peaking time

- Shaping time

DEAD TIME

- Real time

- Live time

- Dead time

CALCULATION

- Peak channel & counts

- UHWHM channel & counts

- LHWHM channel & counts

- Sym noise

- Asym noise

- Total noise

COUNT

- Upper limit

- Lower limit

- No. of counts

- Smooth rank

- Comment

ROI & Peak

Estimate the position of a peak and determine the area beneath it. Linear interpolation between the continuum values on either side of the peak can be used to compensate for the influence of the continuum.

STOP

Stop execution of the VI.

Smooth

Click on this button and alter the smoothing rank, i.e. to increase or decrease the number of points the raw data are smoothed over.

To stop the calculation click this button a second time.

Energy/Channels

Switch between channels and energy [keV] as the unit for the abscissa.

Graph

Plots the number of counts vs. channel or energy [keV].

 **Noise**

Displays the results of noise calculations.

 **UWHM**

 **Counts UWHM**

 **LWHM**

 **Counts LWHM**

 **Sym noise**

 **Asym noise**

 **Total noise**

 **Dead Time**

Displays the live, real and dead time after acquisition has ended.

 **Real time**

 **Live time**

 **Dead time**

 **Preset**

Indicates if preset is in-/active, and real and live time settings.

 **Active**

 **Real time**

 **Live time**

 **Info**

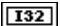
Displays measurement name and comments as entered in the initialisation dialog.

 **Measurement name**

 **Comments**

 **ROI**

Region of interest.

 **No. of counts**

 **Upper channel**

 **Lower channel**

 **Point in time**

Date and time for start of acquisition.

 **Date**

abc Time

Peak Value

Result of peak search.

DBL Peak count

DBL Peak channel

Memory

Displays the current memory settings of the MCA.

U16 No. of channels

U16 First channel

U16 Last channel

U16 Gain

This control specifies the ADC conversion gain which is a multiple of 256. The choices are prewritten.

Elapsed Time

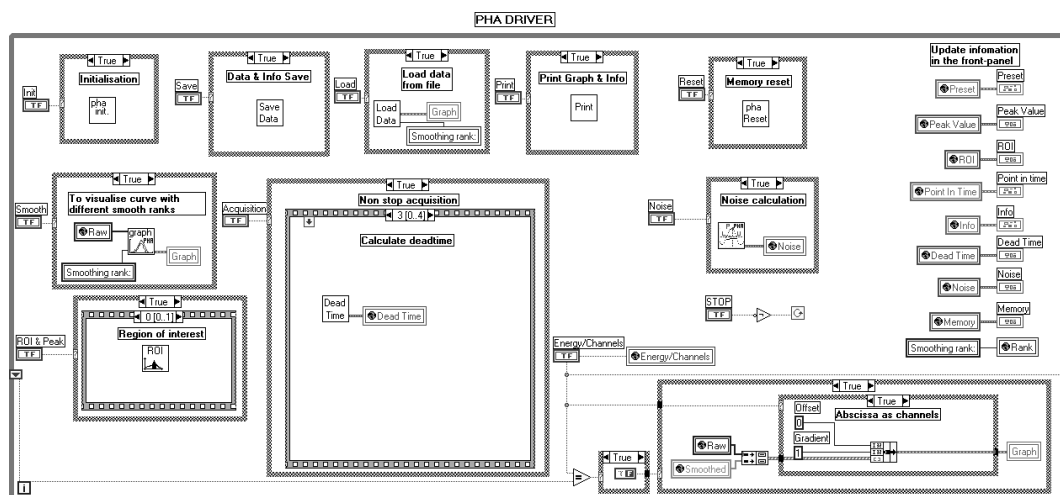
Displays the live, real and dead time during acquisition.

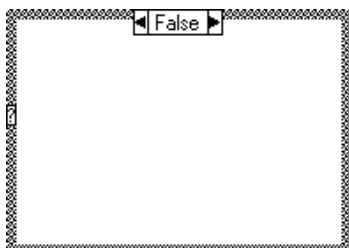
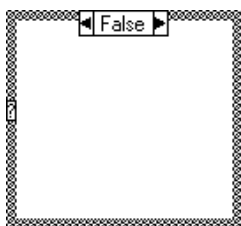
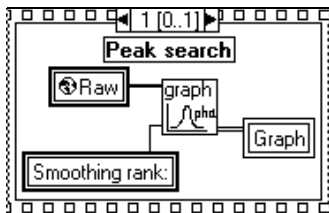
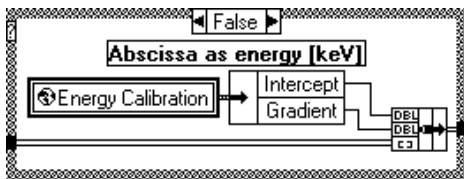
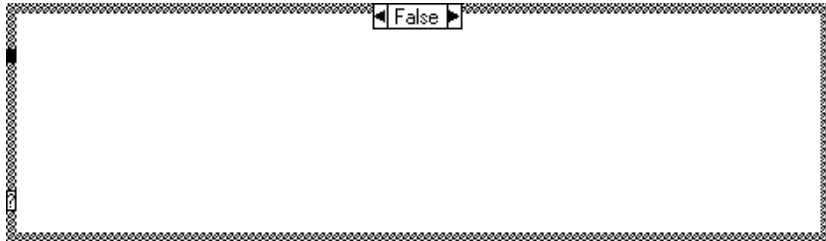
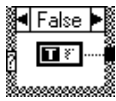
DBL Live time

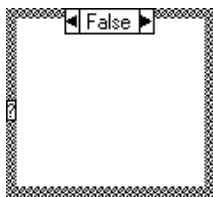
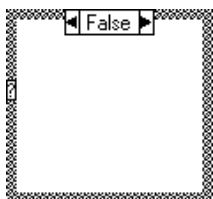
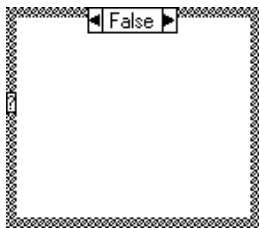
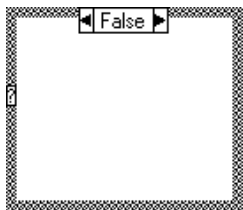
DBL Real time

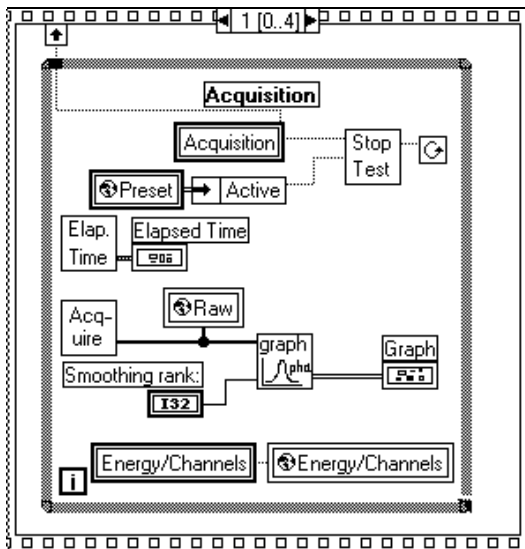
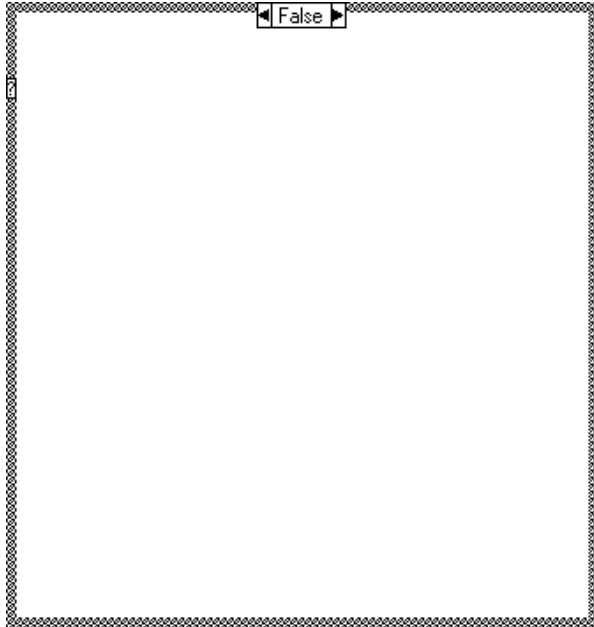
DBL Dead time

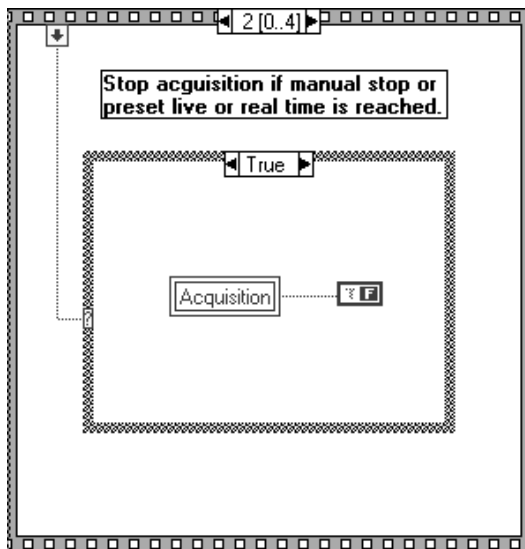
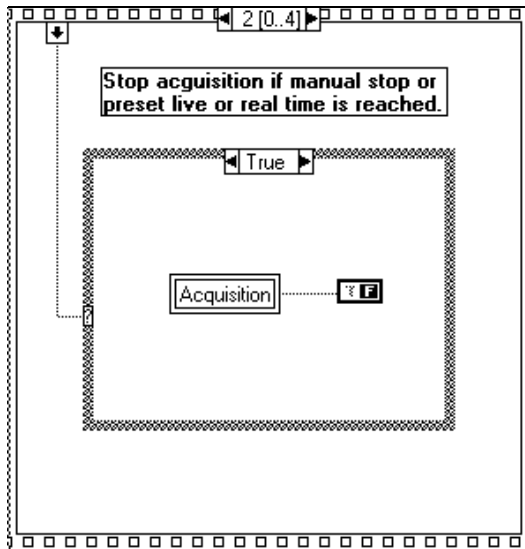
Block Diagram

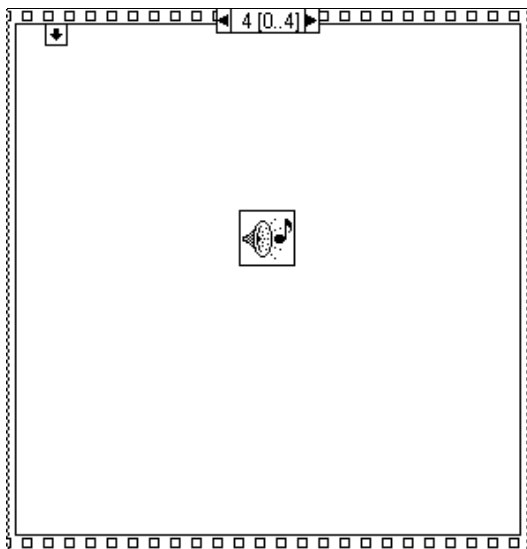
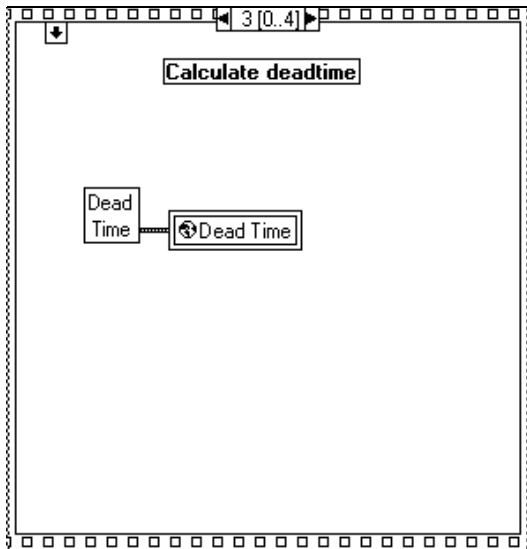












C.2 Initialisation.vi

Initialisation.vi

Initialises the Tennelec/Oxford PCA Multiport Multichannel Analyser.

The settings for the PCA are:

- Gain
- Dead time control: external/internal
- Preset: on/off
- Preset live time
- Preset real time
- Memory size
- Memory group

The energy calibration data consist of:

- Amplifier coarse gain
- Amplifier fine gain
- Gradient
- Intercept

The pulse shape settings consist of:

- Peaking time
- Shaping time

Energy calibration data, amplifier gain and pulse shaping settings can also be entered.

Connector Pane



Front Panel

INITIALISATION

The screenshot shows the INITIALISATION front panel with the following sections:

- ConversionGain:** A numeric control set to 8192 with a multiplier of 5.
- Dead time control:** Radio buttons for External and Internal.
- Memory:**
 - Memory size: Full (16383 channels), Halves (8192 channels), Quarters (4096 channels).
 - Memory group: A dropdown menu.
- Energy Calibration:**
 - Coarse gain: 20 with a multiplier of 2.
 - Fine gain: 1.08.
 - Gradient: 0.0192.
 - Intercept: 2.7865.
- Pulse Shape:**
 - Peaking time (µs): 4 with a multiplier of 6.
 - Shaping time (µs): 2 with a multiplier of 6.
- Preset:**
 - Preset live time: 300.
 - Preset on/off: Radio buttons for On and Off.
 - Preset real time: 300.
- Info:**
 - Measurement name: Element: Xx; PPM: X.X; Detector: NaI(Tl) Coll.S: d=3 mm; Coll.D: 3*3 mm^2
 - Comments: Dist S-O: 0.0 mm; Dist D-O: 9.0 mm; Pen S-O: 6.0 mm; Pen D-O: 5.5 mm; Source: 241-Am 30 mCu
- CONTINUE:** A button to exit the dialog.

Controls and Indicators

TF Continue

Press this button when to exit from this dialog.

I32 Memory size

For information look at description of the 'Memory group' control.

U8 Memory group

The two memory controls enable you to select active memory group and memory size (no. of channels).

First choose memory size, i.e. the number of channels used during acquisition. The number of channels must be greater than or equal to the selected conversion gain.

Then select the memory group, i.e. the part of memory you want to store the spectrum in (total memory of device 16384channels).

The product of memory group number and memory size must not exceed 16384 channels.

U16 ConversionGain

This control specifies the ADC conversion gain, which is a multiple of 256.

U32 Preset real time

 **Preset live time**

 **Preset on/off**

When preset is set active the data acquisition will automatically stop when either of the preset times are reached.

Data acquisition can be stopped manually even when preset is active.

 **Info**

 **Measurement name**

 **Comments**

 **Energy Calibration**

 **Fine gain**

 **Gradient**


 **Intercept**

 **Coarse gain**

 **Pulse Shape**

 **Shaping time [ms]**

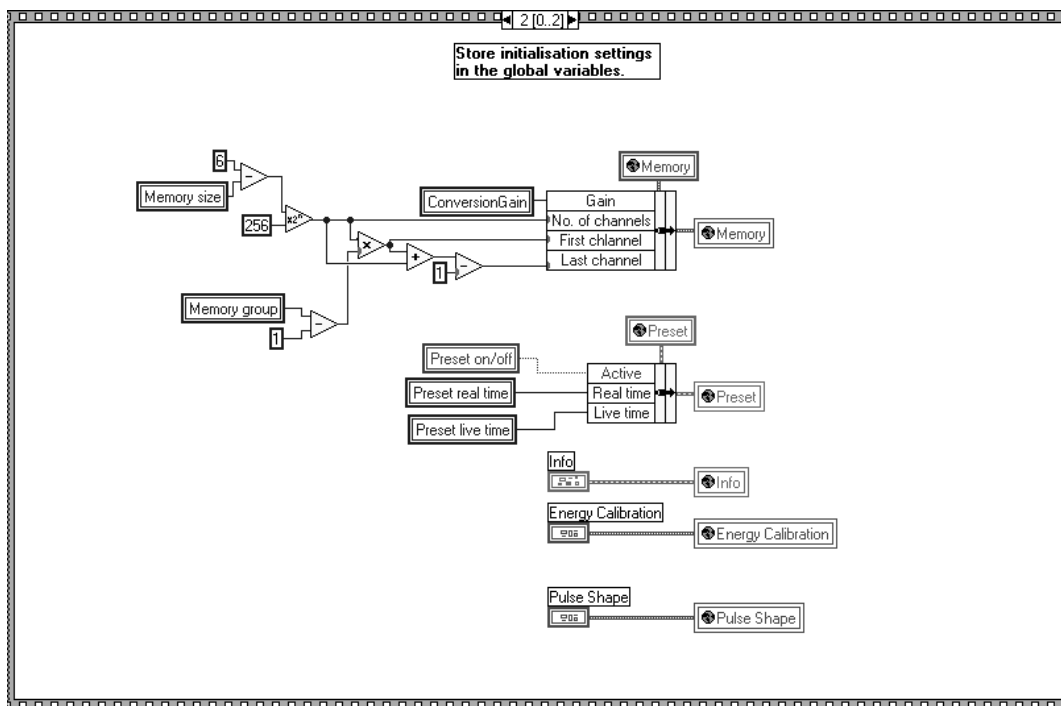
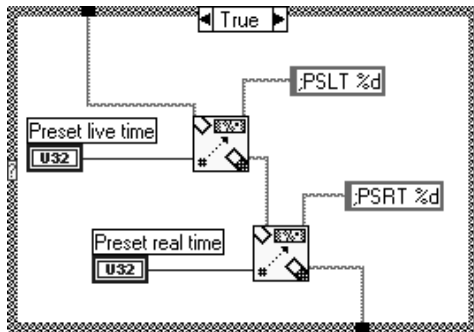
 **Peaking time [ms]**

 **Dead time control**

Dead time control should only be set to external if an external ADC is used.

 **error mes**

Block Diagram



C.3 Reset.vi

Reset.vi

Reset all the channels of the active memory group to zero.

Re-initialise global-variables to default values.

Connector Pane



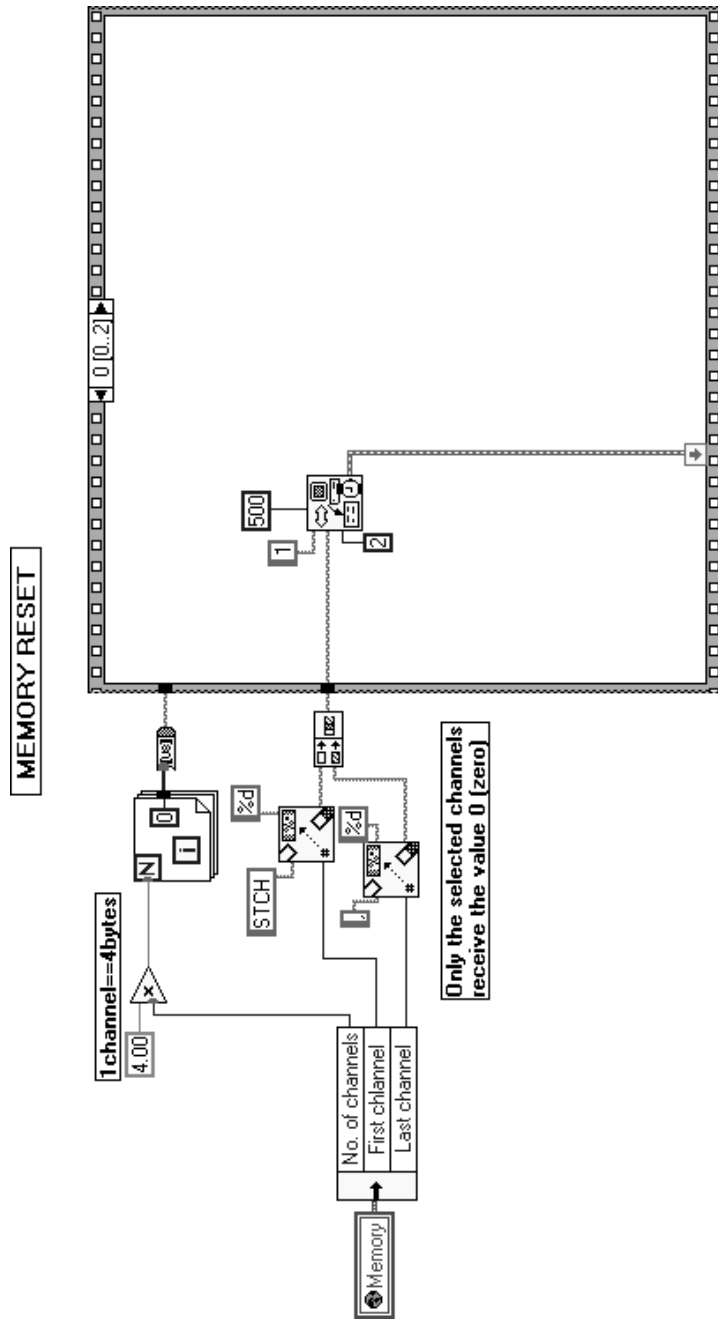
Front Panel

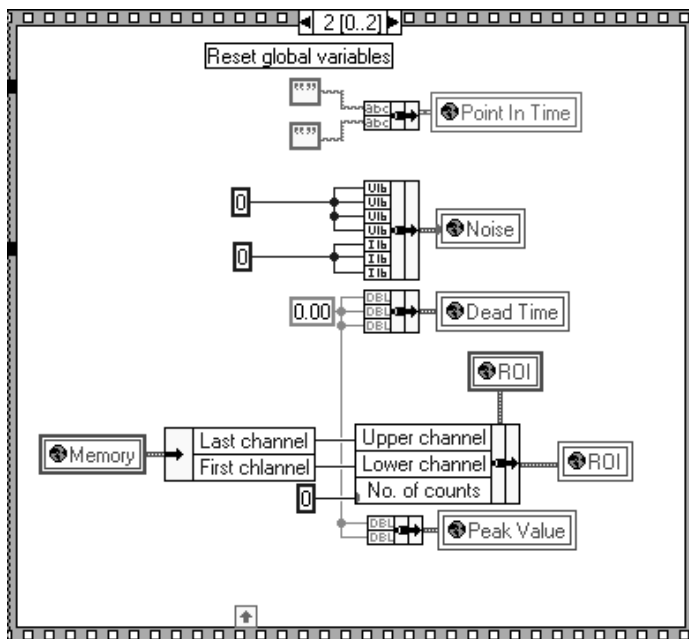
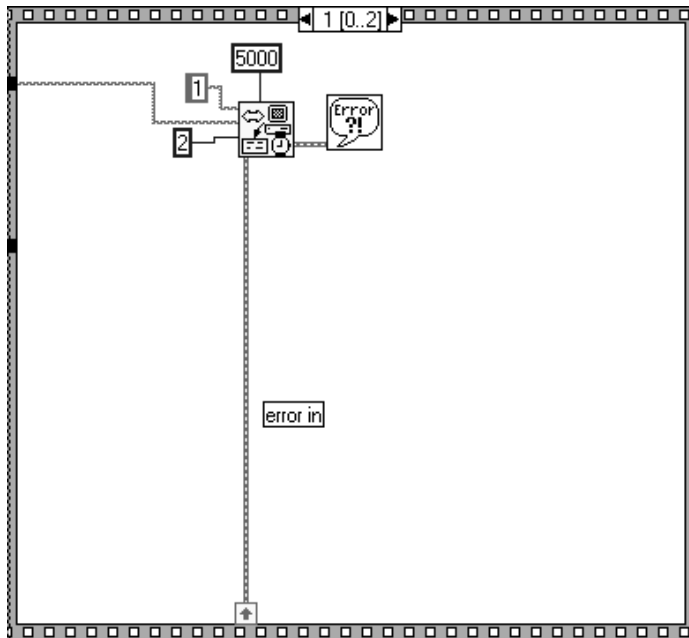
Reset

Reset all the channels of the active memory group to zero.
Initialise global-variables.

Controls and Indicators

Block Diagram





C.4 Region of interest.vi

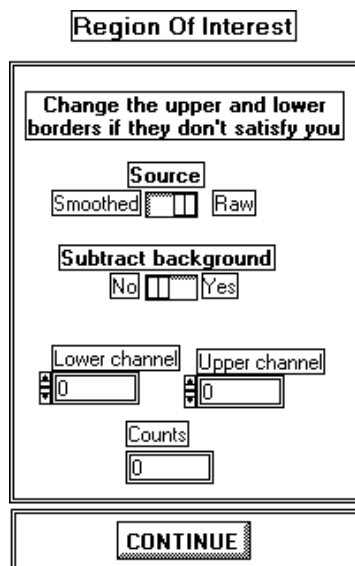
Region Of Interest.vi

This function determines the area under a peak. A linear interpolation between the continuum values on either side of the peak is used to estimate the influence of the continuum.

Connector Pane



Front Panel



Controls and Indicators

 Continue

Press this button when the entered values satisfy you.

 Lower channel

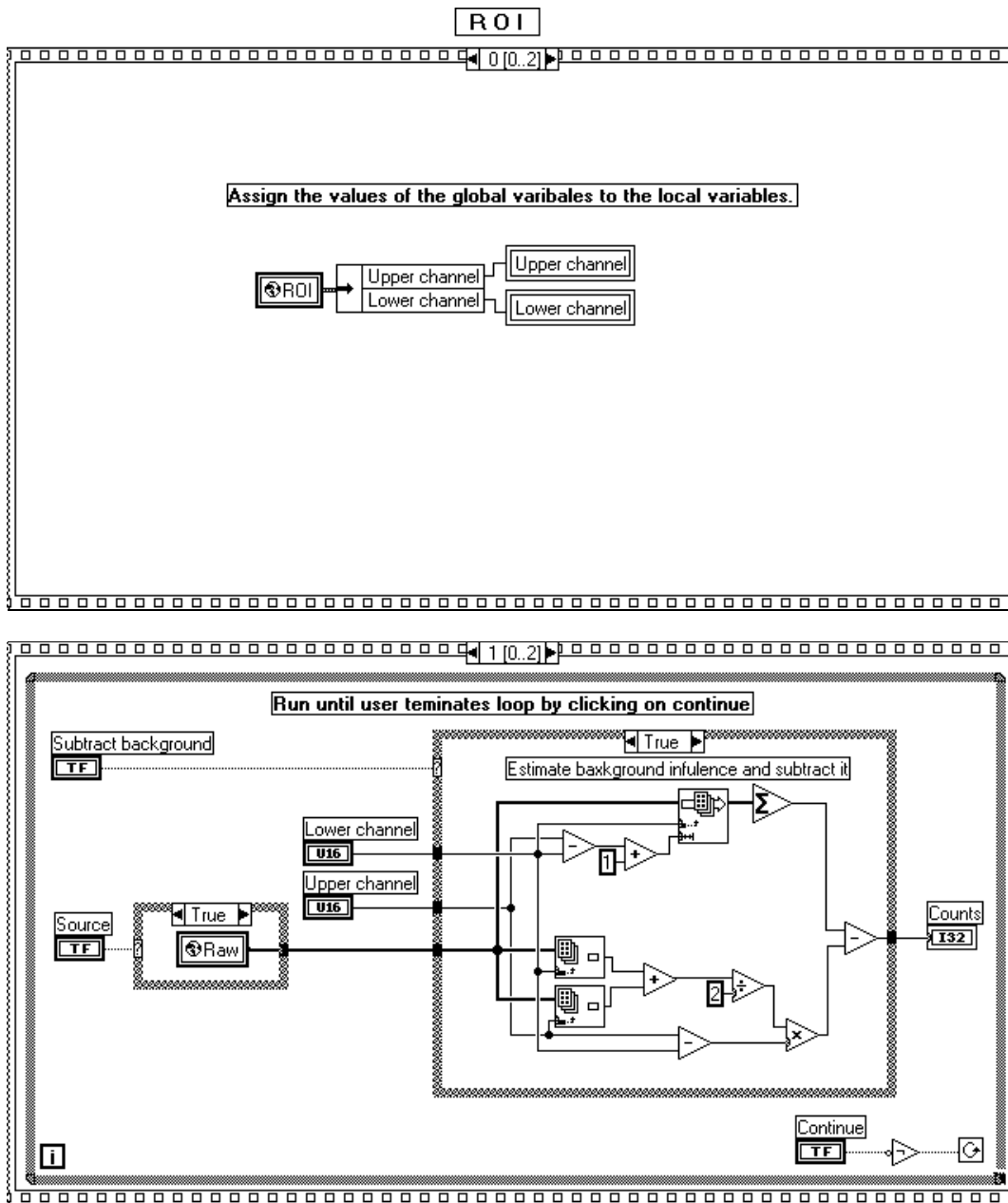
 Upper channel

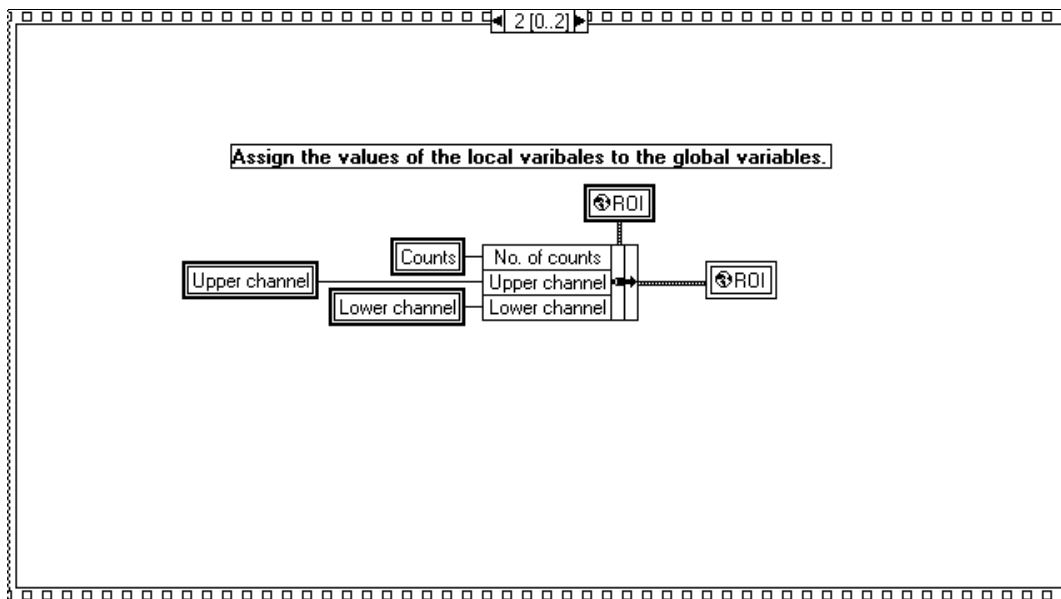
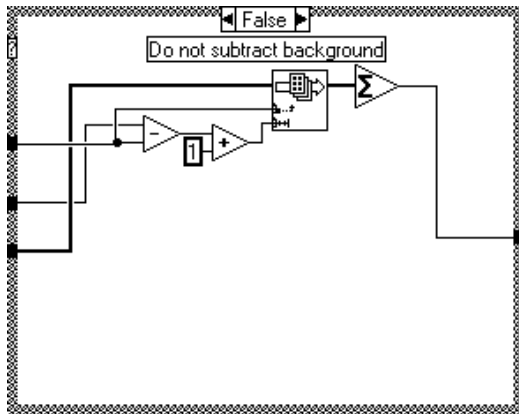
 Source

 Subtract background

 Counts

Block Diagram





C.5 Noise calculation.vi

Noise Calculation.vi

Calculates peak channel & counts, UHWHM, LHWHM channels plus symmetric, asymmetric and total noise.

This VI will suggest peak channel & counts. The user may modify the peak channel value.

Explanation of abbreviations:

UHWHM:

Upper Half Width Half Maximum

LHWHM

Lower Half Width Half Maximum

Total noise:

The number of channels between UHWHM and LHWHM.

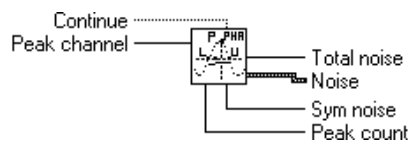
Symmetric noise:

The number of channels between the peak channel and UHWHM multiplied by a factor of two.

Asymmetric noise:

The difference in number of channels between total noise and symmetric noise.

Connector Pane



Front Panel

CALCULATION

Change the peak values if they don't satisfy you :

Peak channel Peak count

0.00 0.00

LHWHM UHWHM

0.00 0.00

Sym noise Asym noise Total noise

0.00 0.00 0.00

CONTINUE

Controls and Indicators

DBL Peak channel

TF Continue

Press this button to exit form this dialog.

DBL Peak count

DBL LHWHM

DBL UHWHM

DBL Sym noise

DBL Asym noise

DBL Total noise

DBL Noise

DBL UHWHM

DBL

DBL LHWHM

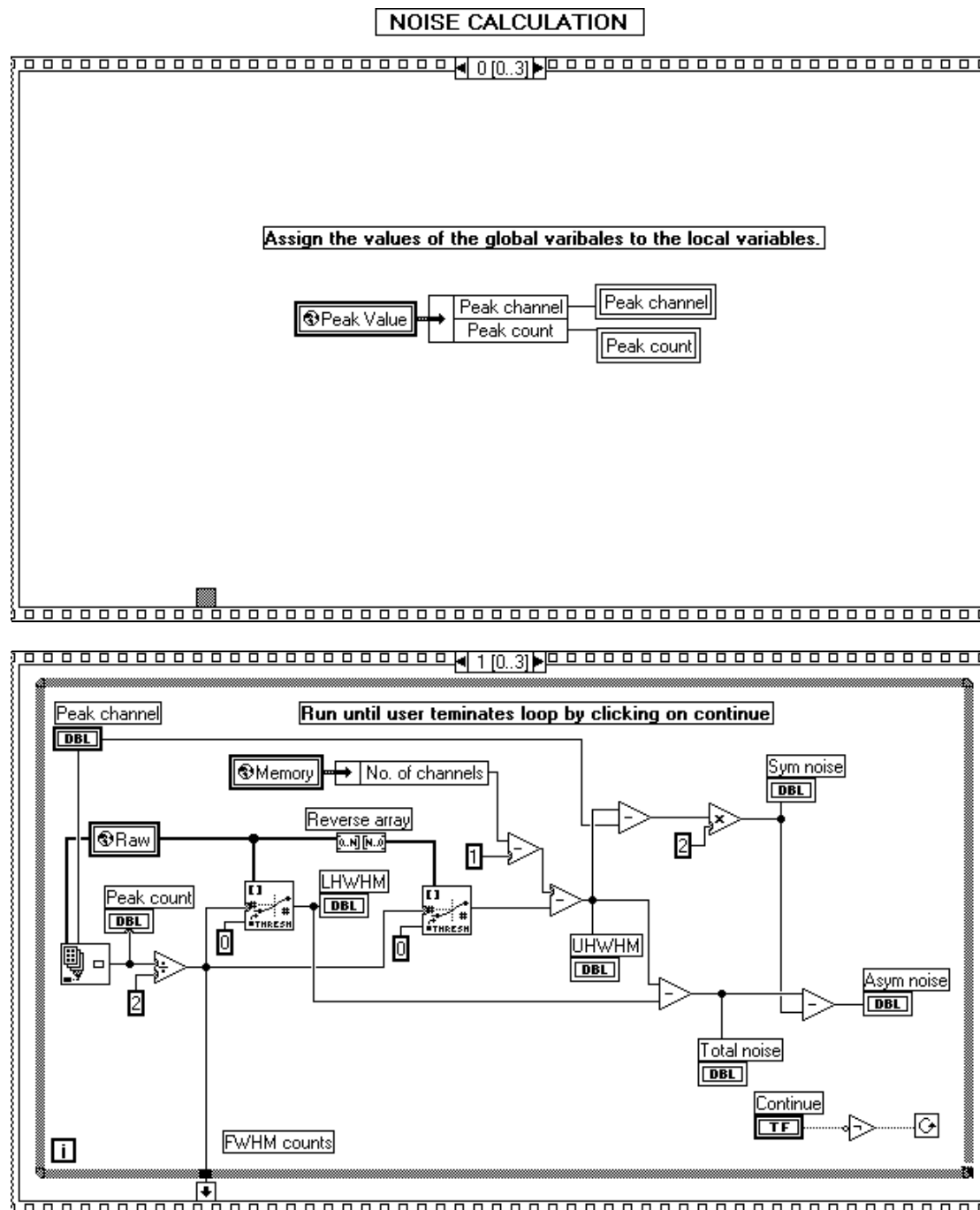
DBL

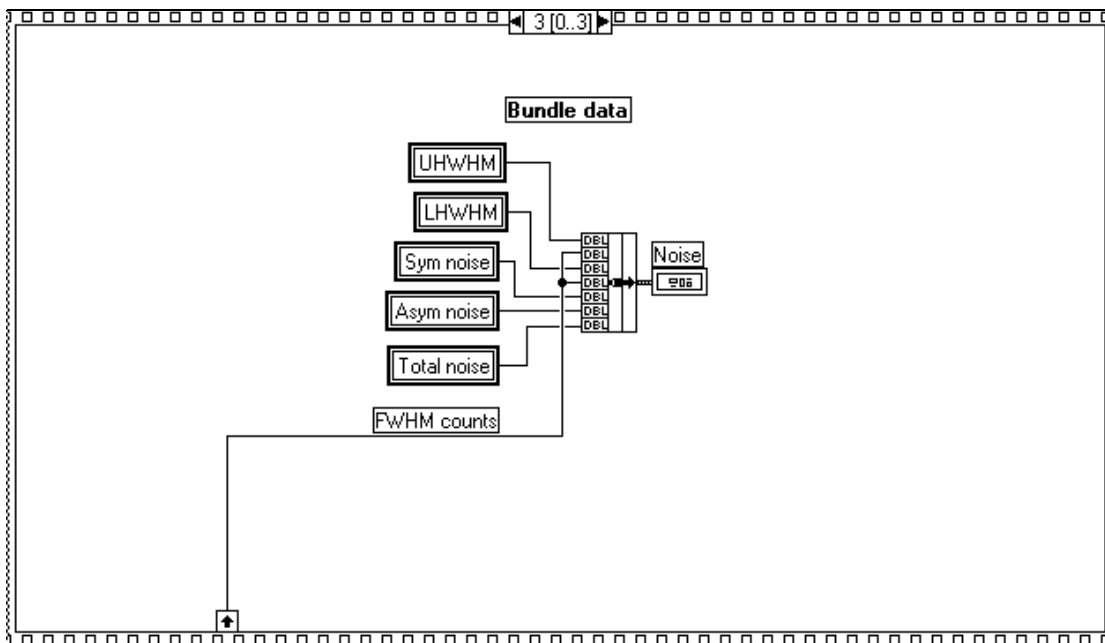
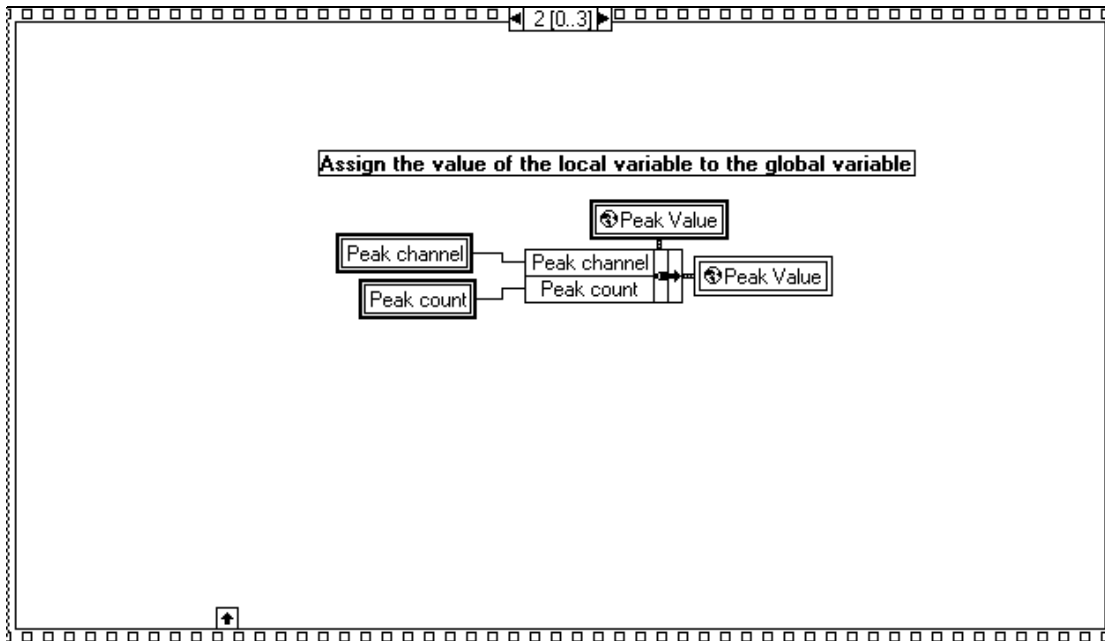
DBL Sym noise

DBL Asym noise

DBL Total noise

Block Diagram





C.6 Save data.vi

Save Data.vi

Saves acquired or loaded data to a tabulator delimited text-file.

The following data will be saved:

- Measurement name

- Date

- Time

SETUP

- Gain

- First channel

- Last channel

- No. of channels

- Preset on/off

- Preset real time

- Preset live time

ENERGY CALIBRATION

- Coarse gain

- Fine gain

- Gradient

- Intercept

PULSE SHAPE

- Peaking time

- Shaping time

DEAD TIME

- Real time

- Live time

- Dead time

CALCULATION

- Peak channel & counts

- UHWHM channel & counts

- LHWHM channel & counts

- Sym noise

- Asym noise

- Total noise

COUNT

- Upper limit

- Lower limit

- No. of counts

- Smooth rank

- Comment

- Recorded spectrum (channel numer, counts per channel and smoothed counts per channel)

Connector Pane

Save
Data

Front Panel

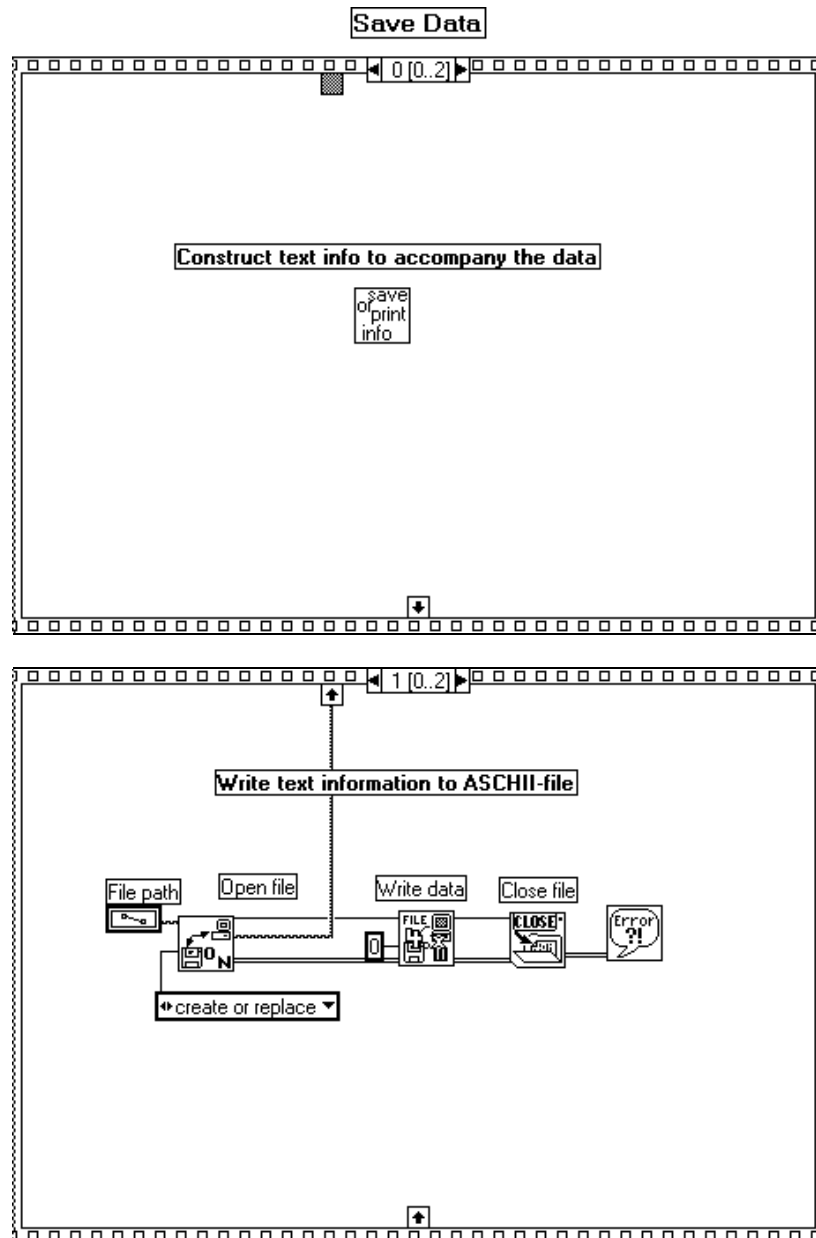
Save Data

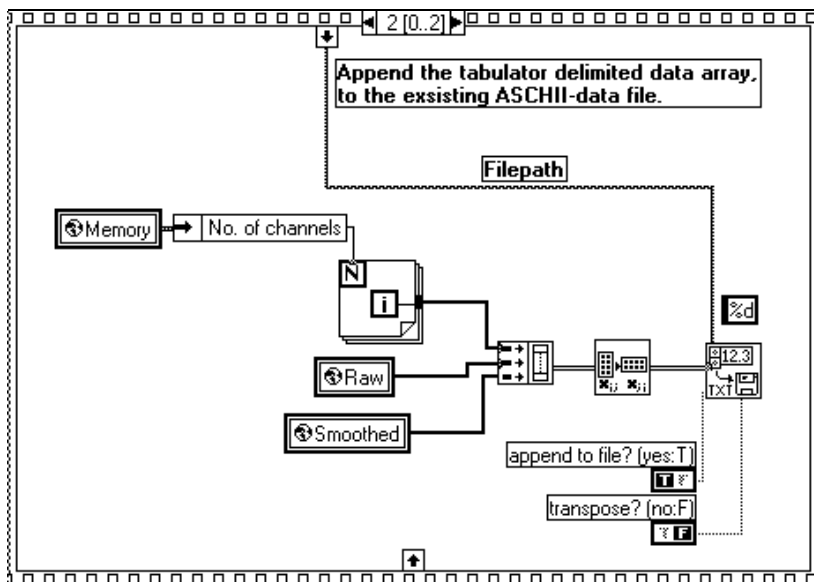
File path

Controls and Indicators

 File path

Block Diagram





C.7 Load data.vi

Load Data.vi

Loads a spectrum and its data from a tabulator delimited text-file.

The following data will be retrieved:

- Measurement name

- Date

- Time

SETUP

- Gain

- First channel

- Last channel

- No. of channels

- Preset on/off

- Preset real time

- Preset live time

ENERGY CALIBRATION

- Coarse gain

- Fine gain

- Gradient

- Intercept

PULSE SHAPE

- Peaking time

- Shaping time

DEAD TIME

- Real time

- Live time

- Dead time

CALCULATION

- Peak channel & counts

- UHWHM channel & counts

- LHWHM channel & counts

- Sym noise

- Asym noise

- Total noise

COUNT

- Upper limit

- Lower limit

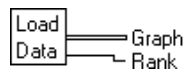
- No. of counts

- Smooth rank

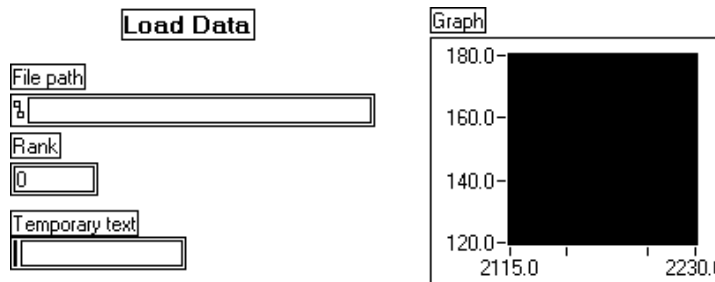
- Comment

- Recorded spectrum (channel numer, counts per channel and smoothed counts per channel)

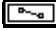


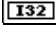
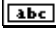

Connector Pane



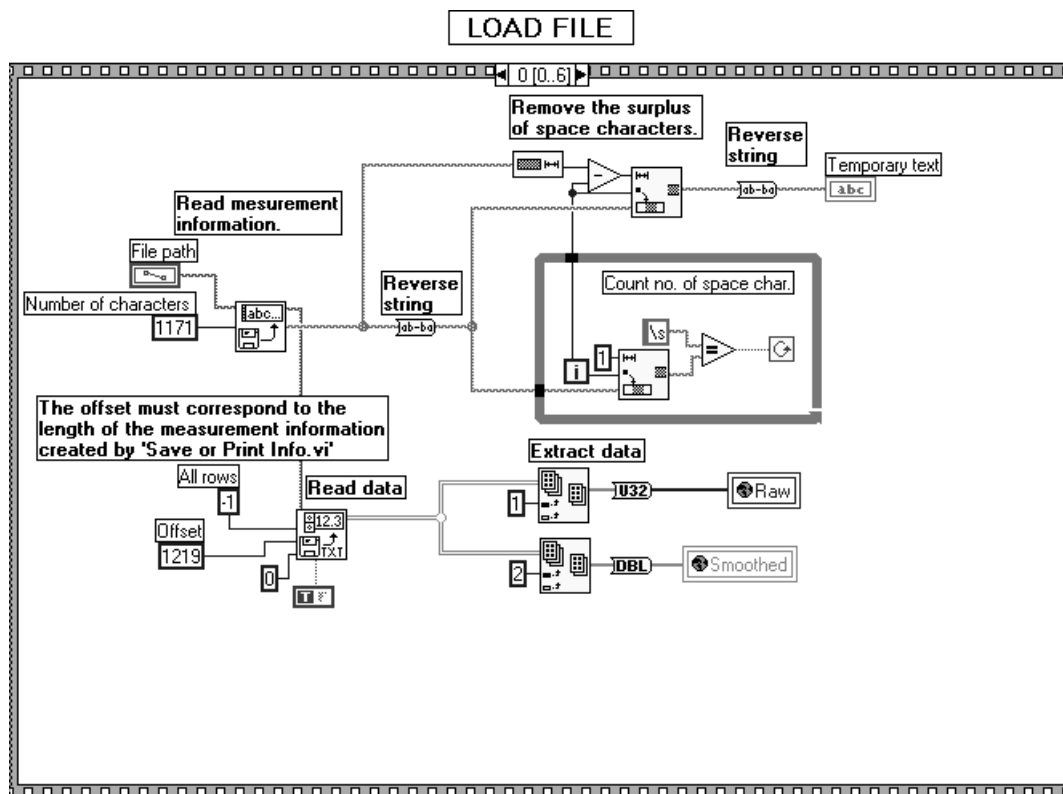
Front Panel

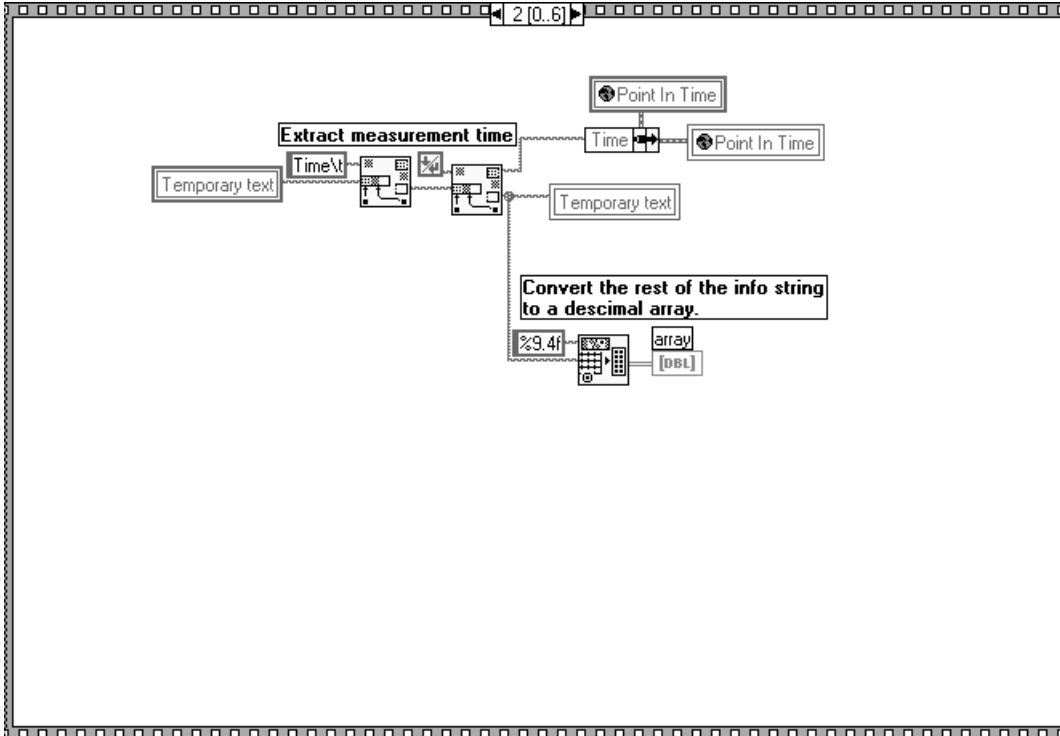
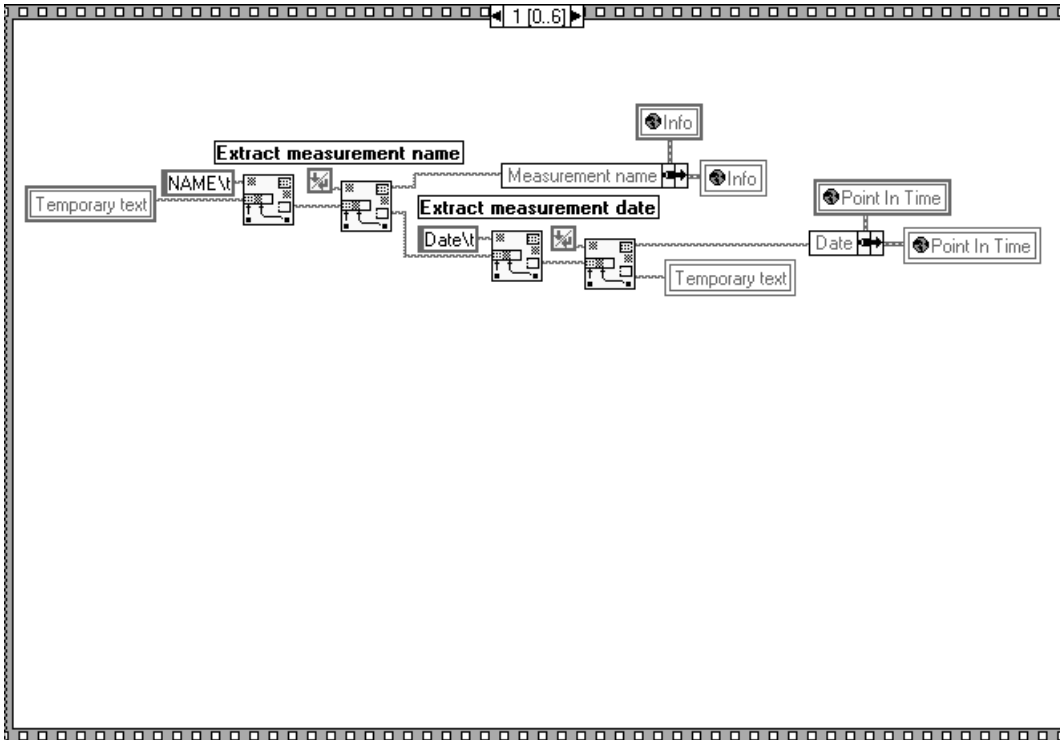


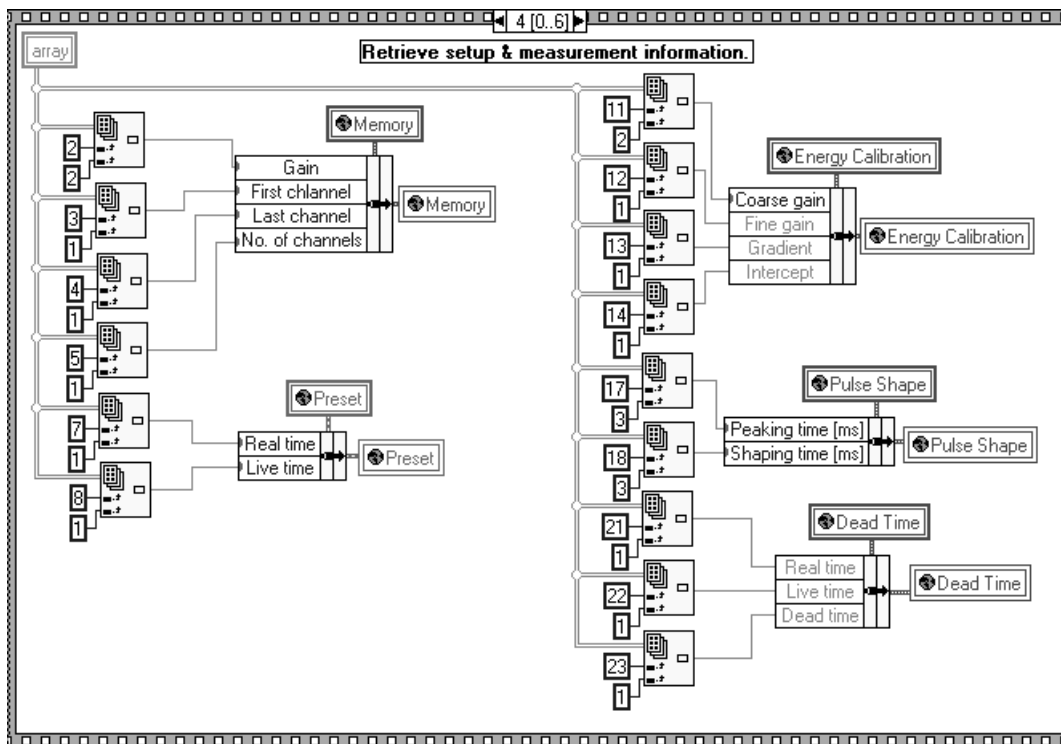
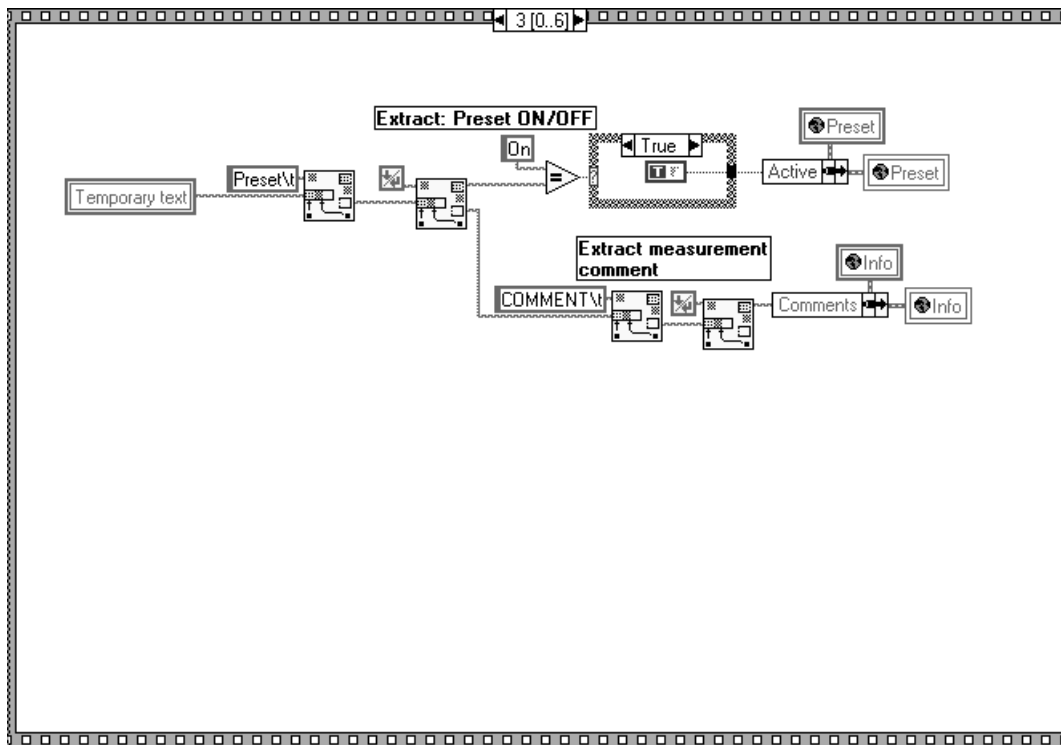
Controls and Indicators

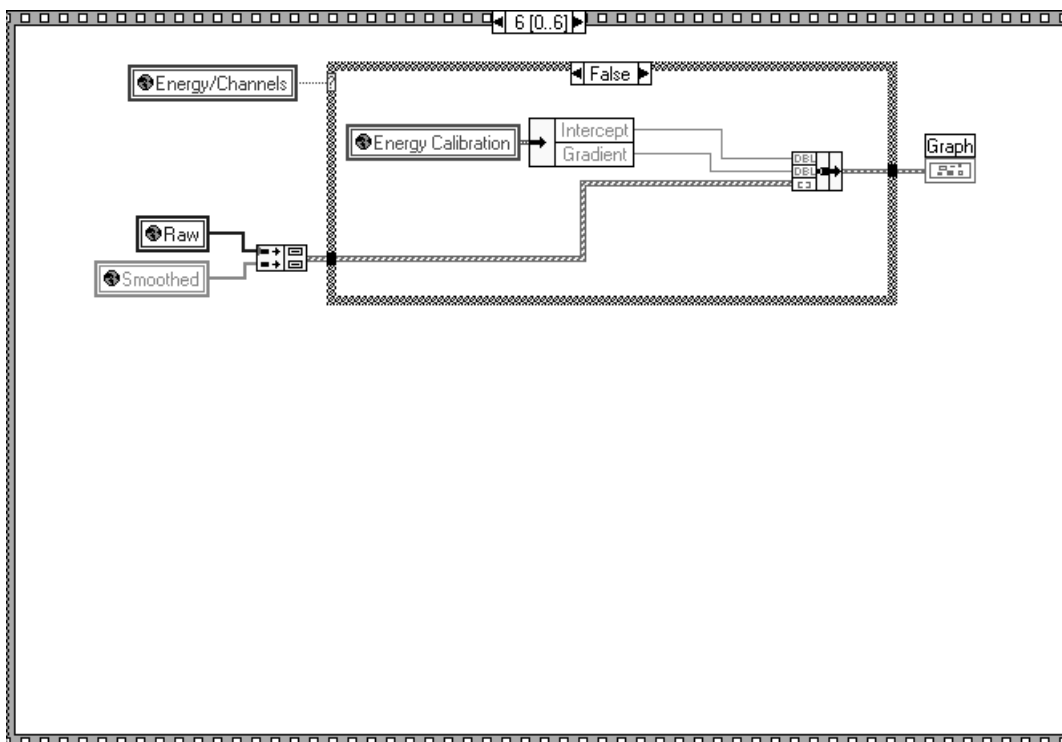
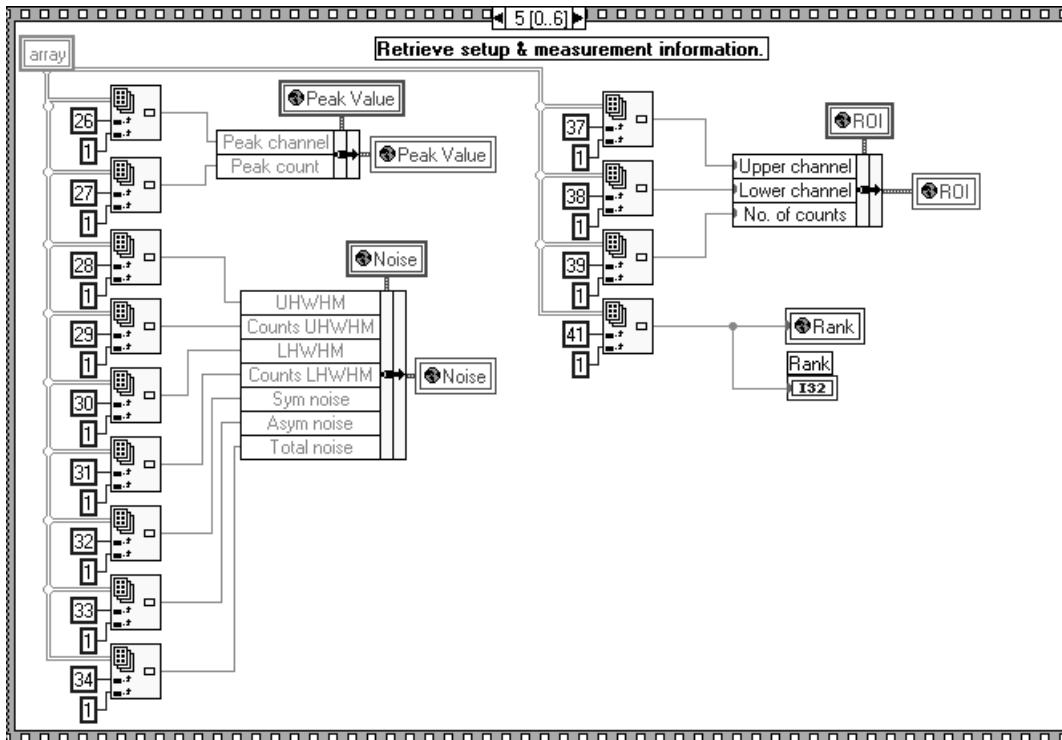
-  File path
-  array
- 
-  Rank
-  Temporary text
-  Graph

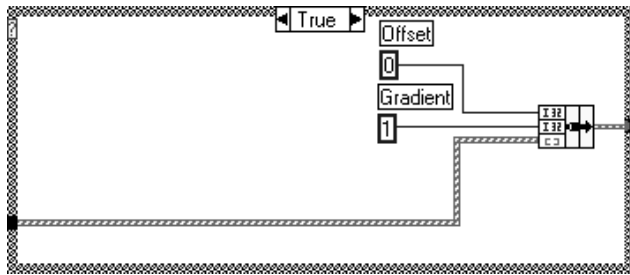
Block Diagram











C.8 Print.vi

Print.vi

Prints the smoothed curve along with the following information:

- Measurement name

- Date

- Time

SETUP

- Gain

- First channel

- Last channel

- No. of channels

- Preset on/off

- Preset real time

- Preset live time

ENERGY CALIBRATION

- Coarse gain

- Fine gain

- Gradient

- Intercept

PULSE SHAPE

- Peaking time

- Shaping time

DEAD TIME

- Real time

- Live time

CALCULATION

- Peak channel & counts
- UHWHM channel & counts
- LHWHM channel & counts
- Sym noise
- Asym noise
- Total noise

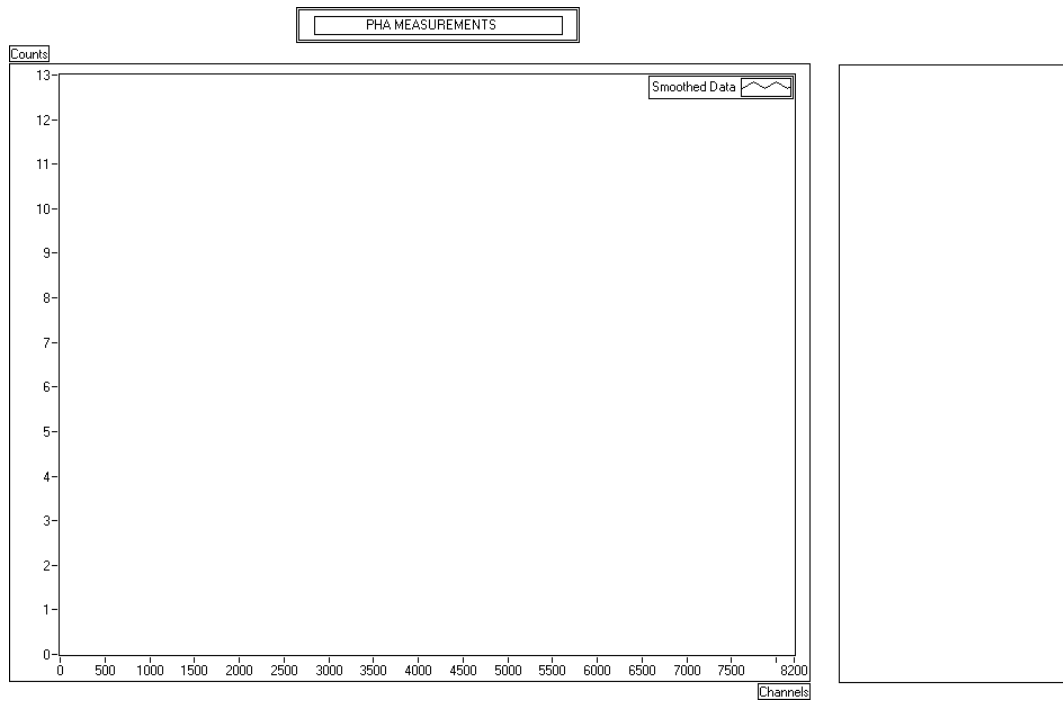
COUNT

- Upper limit
- Lower limit
- No. of counts
- Smooth rank
- Comment

Connector Pane



Front Panel

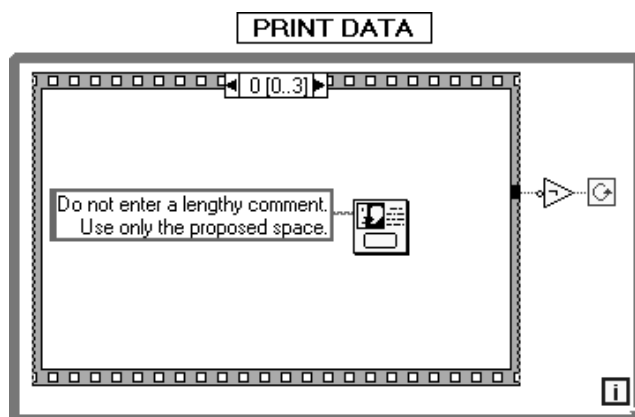


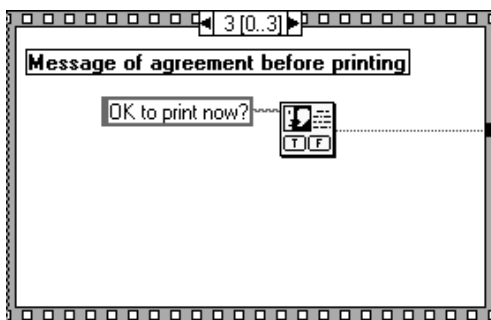
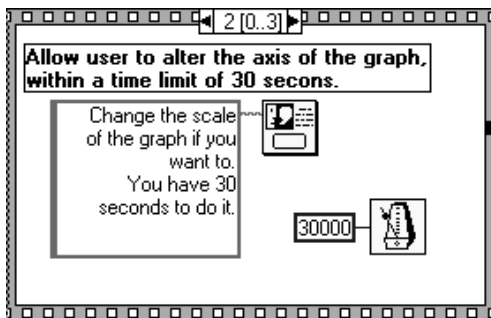
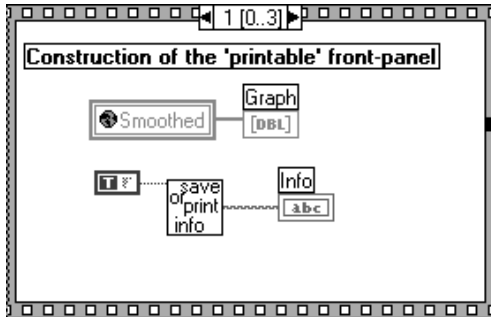
Controls and Indicators

Graph

Info

Block Diagram





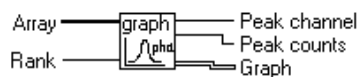
C.9 Smoothing and peak search.vi

Smoothing and Peak Search.vi

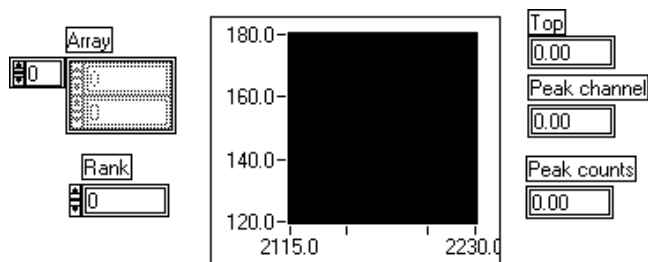
Smooths the raw data over the number of points specified by the rank.

Estimates the channel number of the highest peak in the spectrum.

Connector Pane



Front Panel



Controls and Indicators

[U32] Array

[U32]

[I32] Rank

[DBL] Top

[DBL] Counts

[DBL]

[DBL] Channel

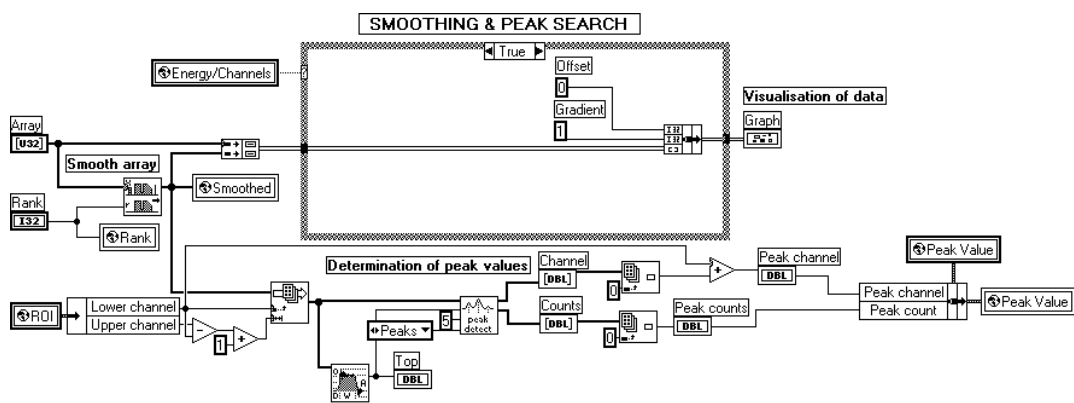
[DBL]

[G] Graph

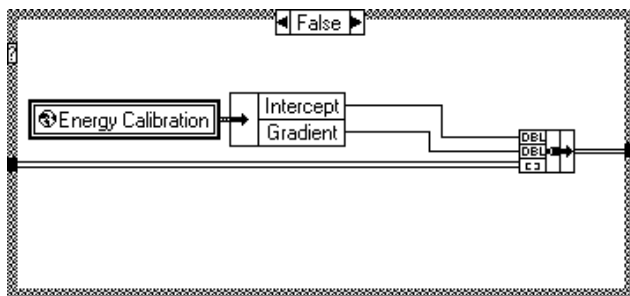
[DBL] Peak channel

[DBL] Peak counts

Block Diagram



The sub-vi, named 'Pulse Parameters.vi' analyse a pulse and determines the top. Usually the top value is lower than the actual peak value. The top value is utilized as the threshold for peak detection.



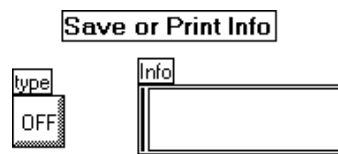
C.10 Save or print info.vi

Save or Print Info.vi

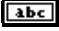

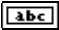
Connector Pane



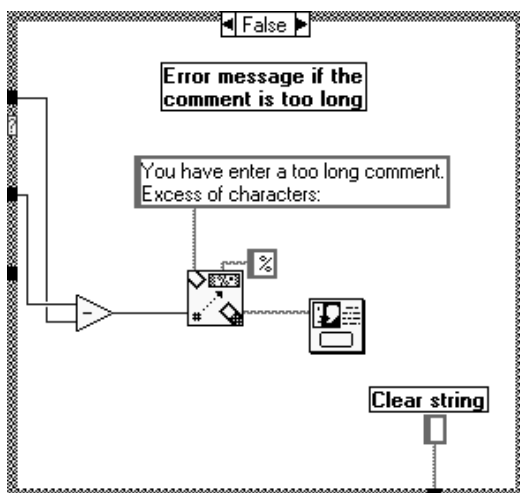
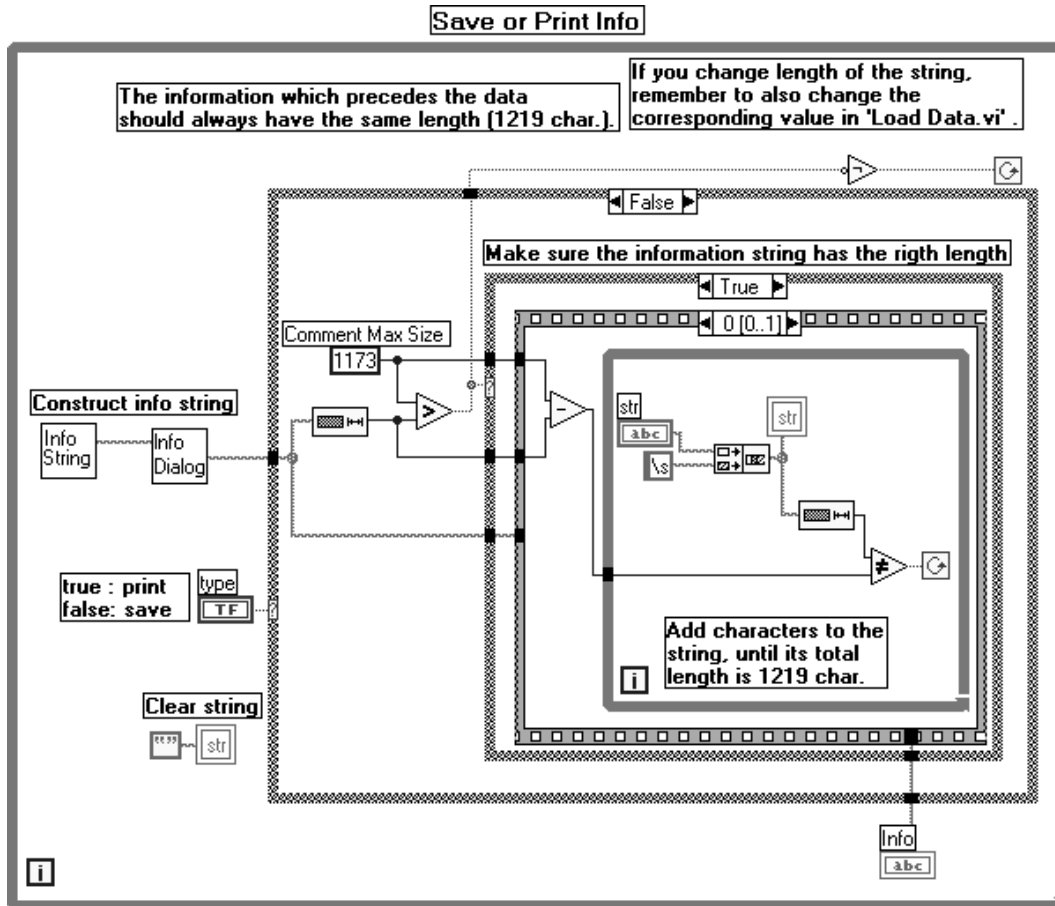
Front Panel

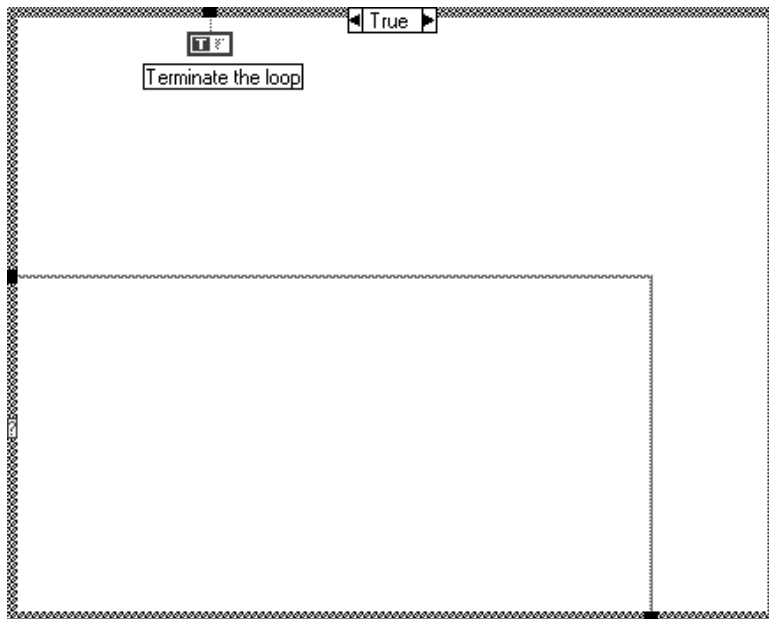
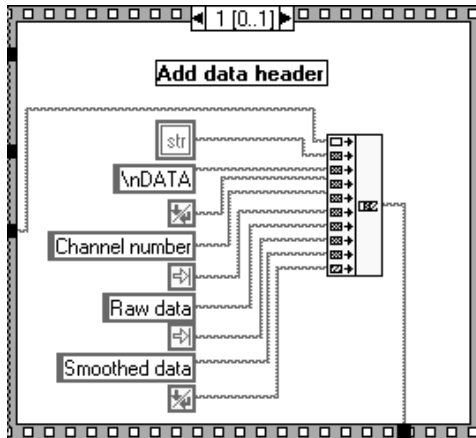


Controls and Indicators

-  str
 -  type
 -  Info
-

Block Diagram





C.11 Info string.vi

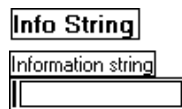
Info String.vi

Constructs a text string with information to accompany the spectrum data.

Connector Pane



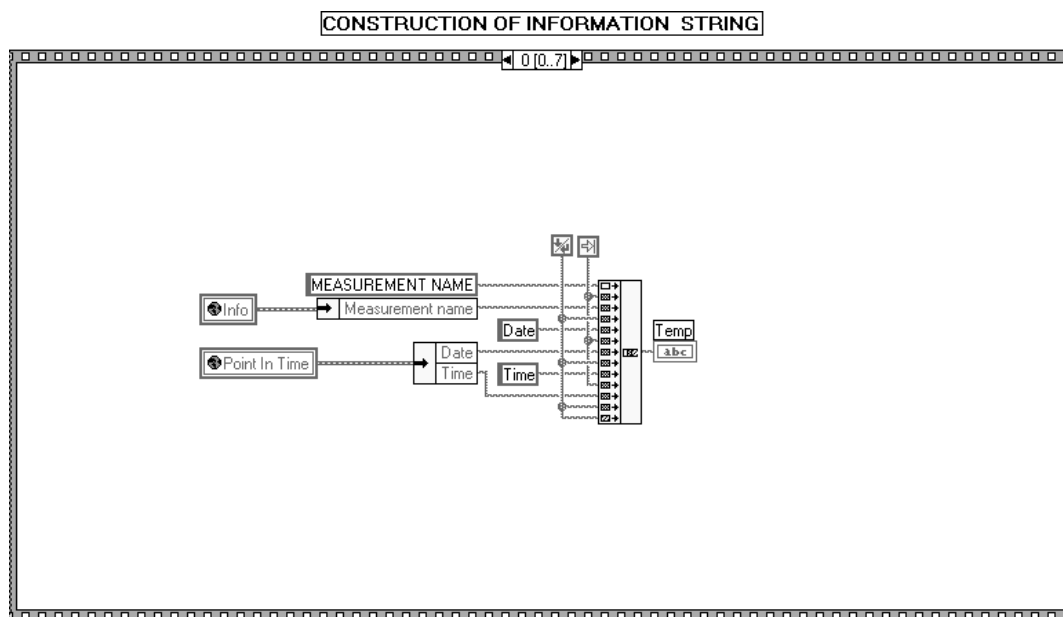
Front Panel

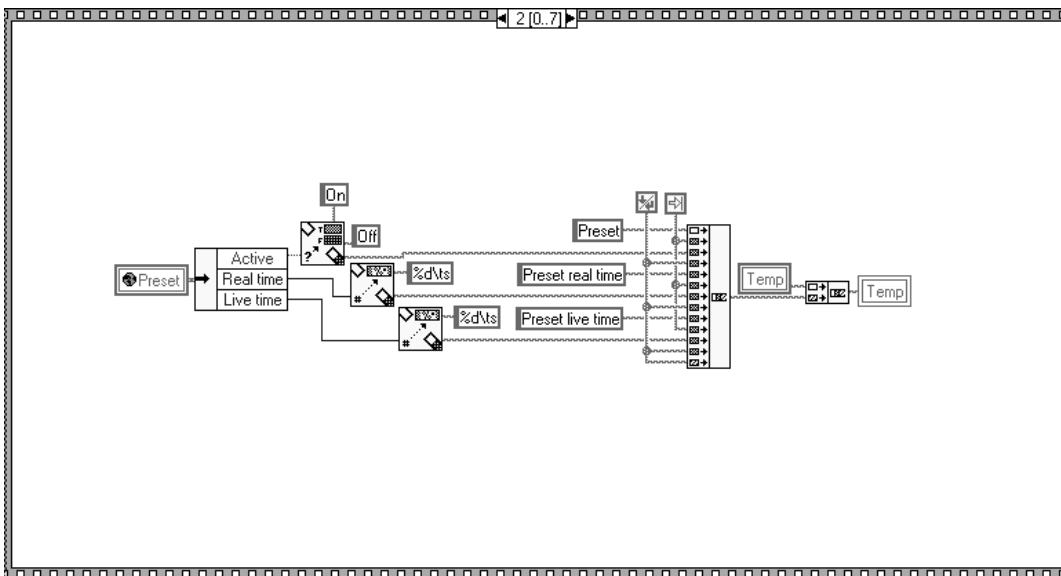
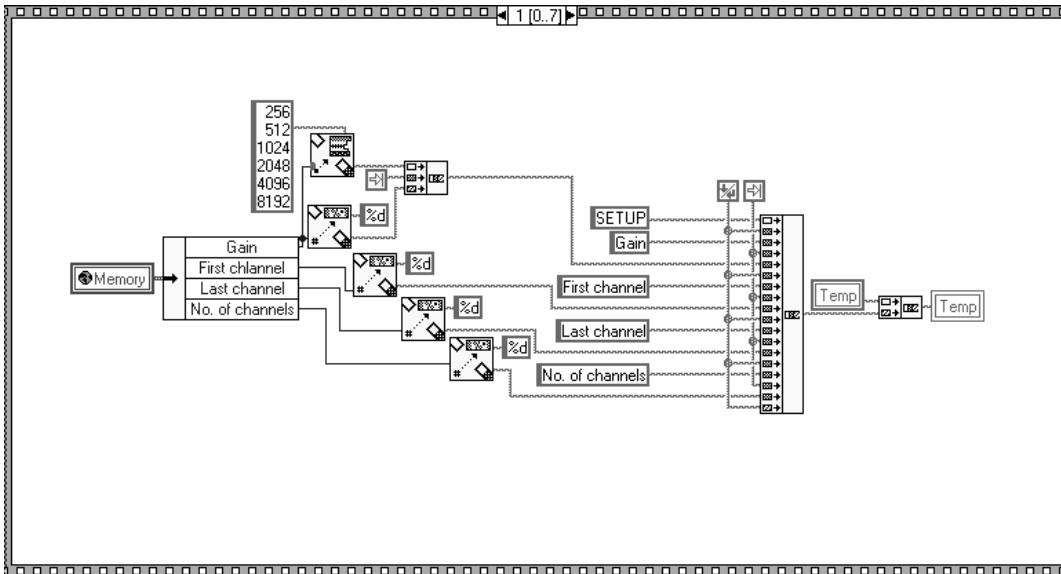


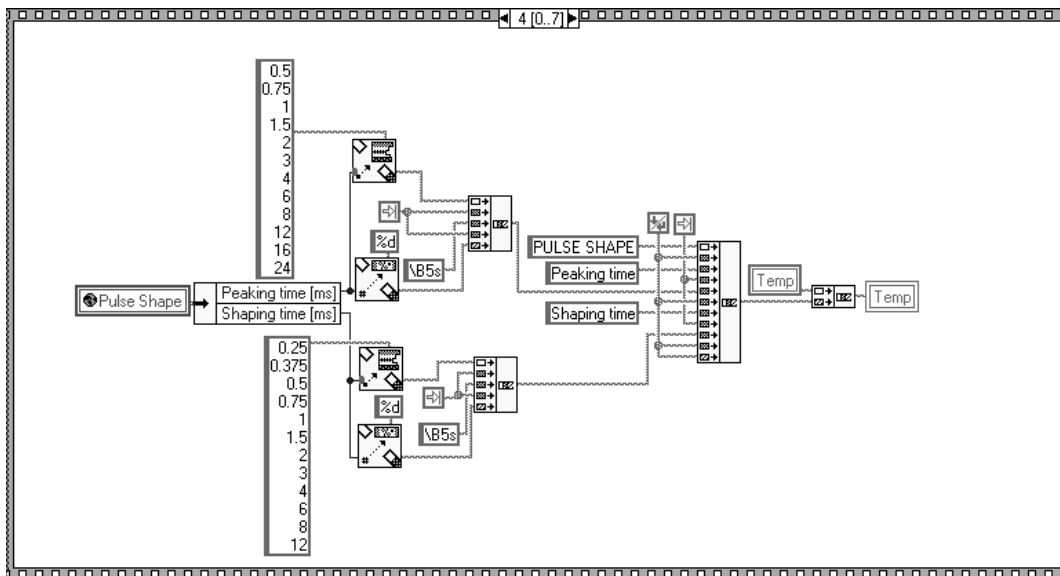
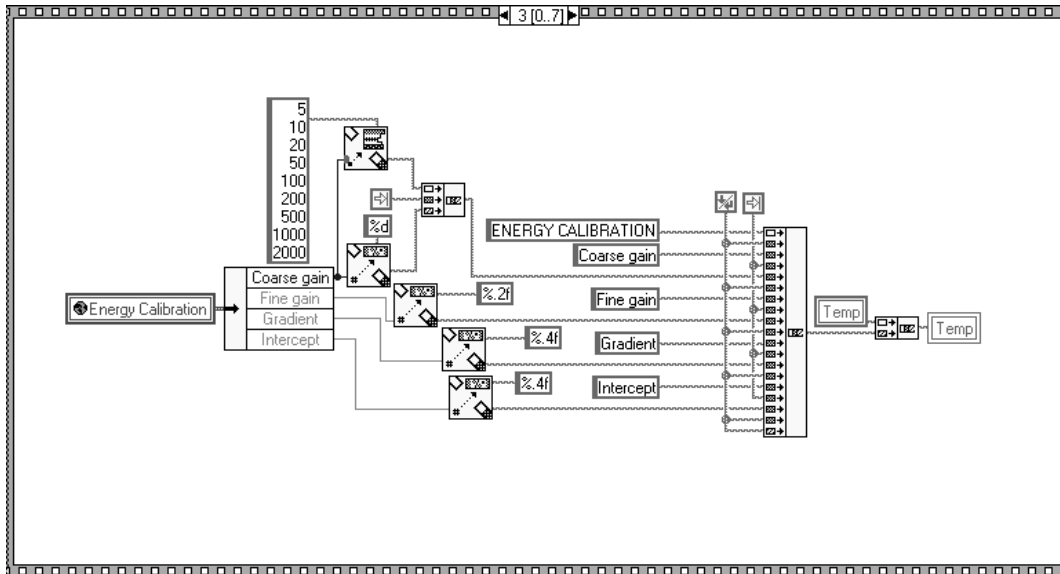
Controls and Indicators

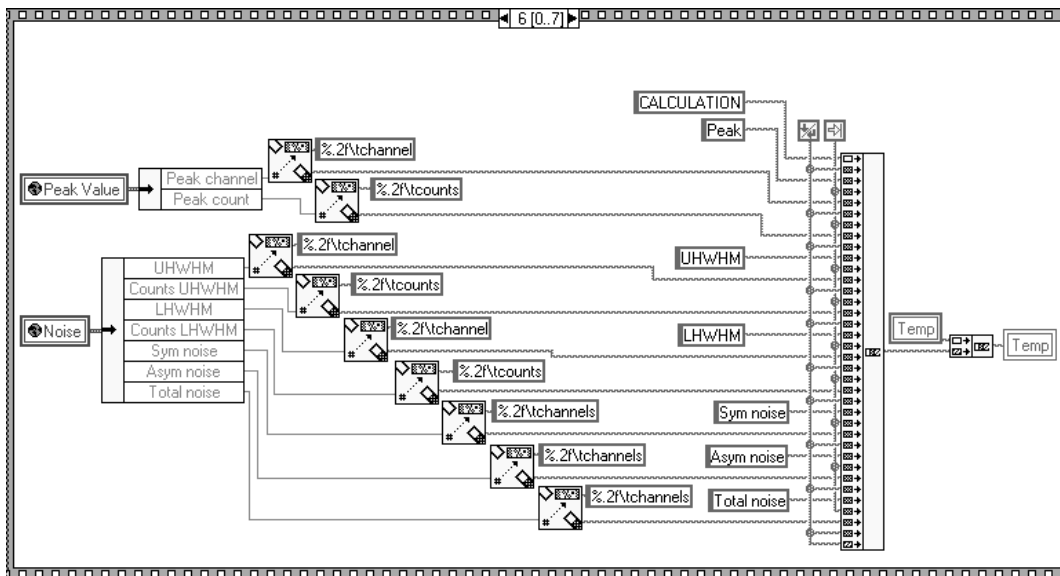
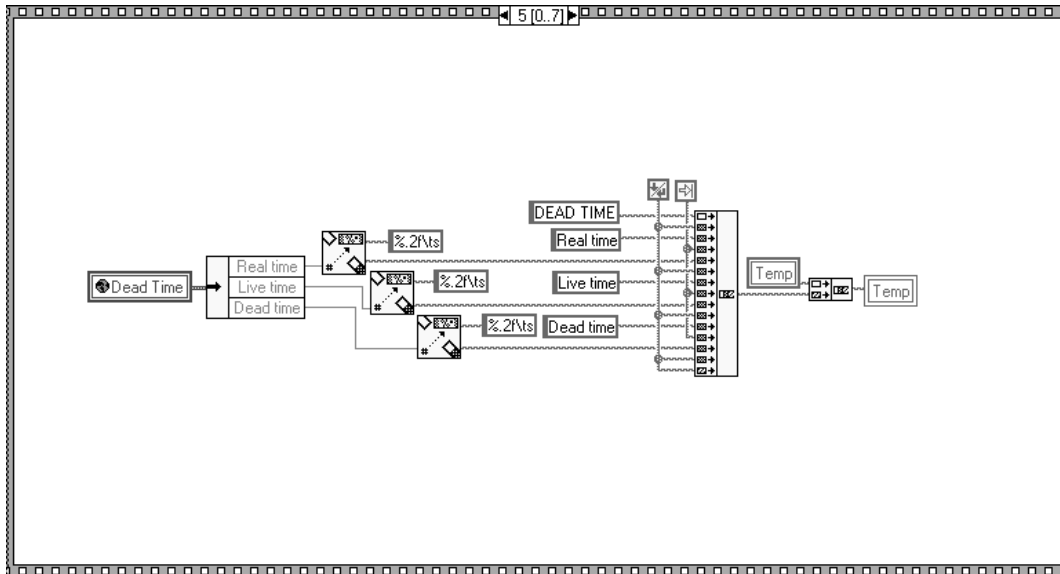


Block Diagram









C.12 Info dialogue.vi

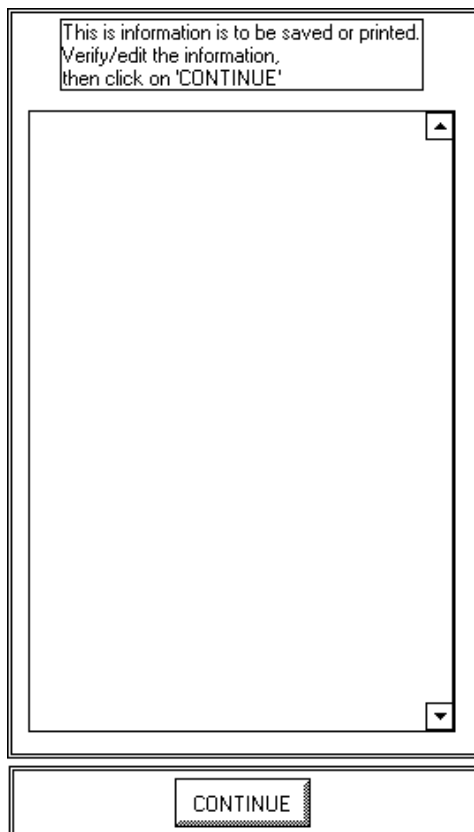
Info Dialogue.vi

Presents a dialog in order to let the user change the information string that accompanies the spectrum data.

Connector Pane



Front Panel



Controls and Indicators

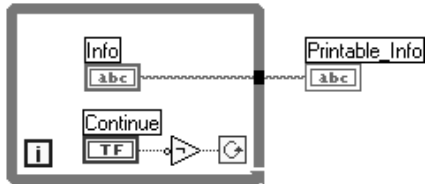
 Info

 Continue

abc Printable_Info

Block Diagram

INTERACTIVE WINDOW FOR INFO EDITING



C.13 Elapsed time.vi

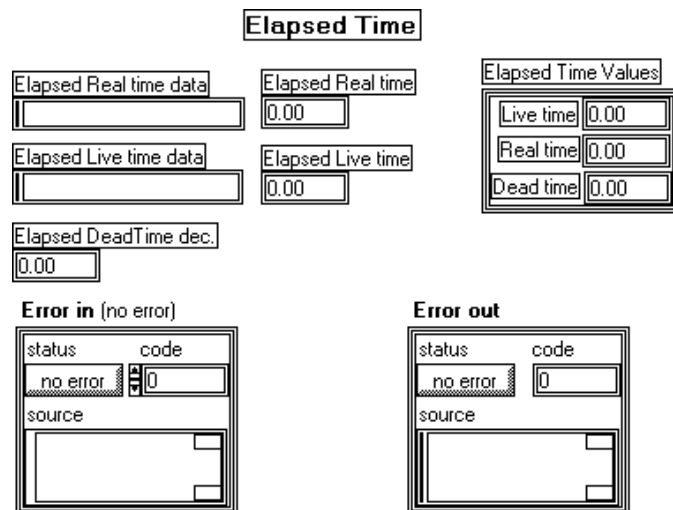
Elapsed Time.vi

Reads real and live time data from the PCA and calculates the dead time.

Connector Pane



Front Panel



Controls and Indicators

Error in (no error)

error in is a cluster that describes the error status before this VI executes. If error in indicates that an error occurred before this VI was called, this VI may choose not to execute its function, but just pass the error through to its error out cluster. If no error has occurred, then this VI executes normally and sets its own error status in error out. Use the error handler VIs to look up the error code and to display the corresponding error message. Using error in and error out clusters is a convenient way to check errors and to specify execution order by wiring the error output from one subVI to the error input of the next.

status

status is TRUE if an error occurred before this VI was called, or FALSE if not.

If status is TRUE, code is a non-zero error code. If status is FALSE, code can be zero or a warning code.

I32 **code**

code is the number identifying an error or warning. If status is TRUE, code is a non-zero error code. If status is FALSE, code can be zero or a warning code. Use the error handler VIs to look up the meaning of this code and to display the corresponding error message.

abc **source**

source is a string that indicates the origin of the error, if any. Usually source is the name of the VI in which the error occurred.

abc **Elapsed Real time data****abc** **Elapsed Live time data****DBL** **Elapsed Real time****DBL** **Elapsed Live time****DBL** **Elapsed DeadTime dec.****EO5** **Error out**

error out is a cluster that describes the error status after this VI executes. If an error occurred before this VI was called, error out is the same as error in. Otherwise, error out shows the error, if any, that occurred in this VI. Use the error handler VIs to look up the error code and to display the corresponding error message. Using error in and error out clusters is a convenient way to check errors and to specify execution order by wiring the error output from one subVI to the error input of the next.

TF **status**

status is TRUE if an error occurred, or FALSE if not. If status is TRUE, code is a non-zero error code. If status is FALSE, code can be zero or a warning code.

I32 **code**

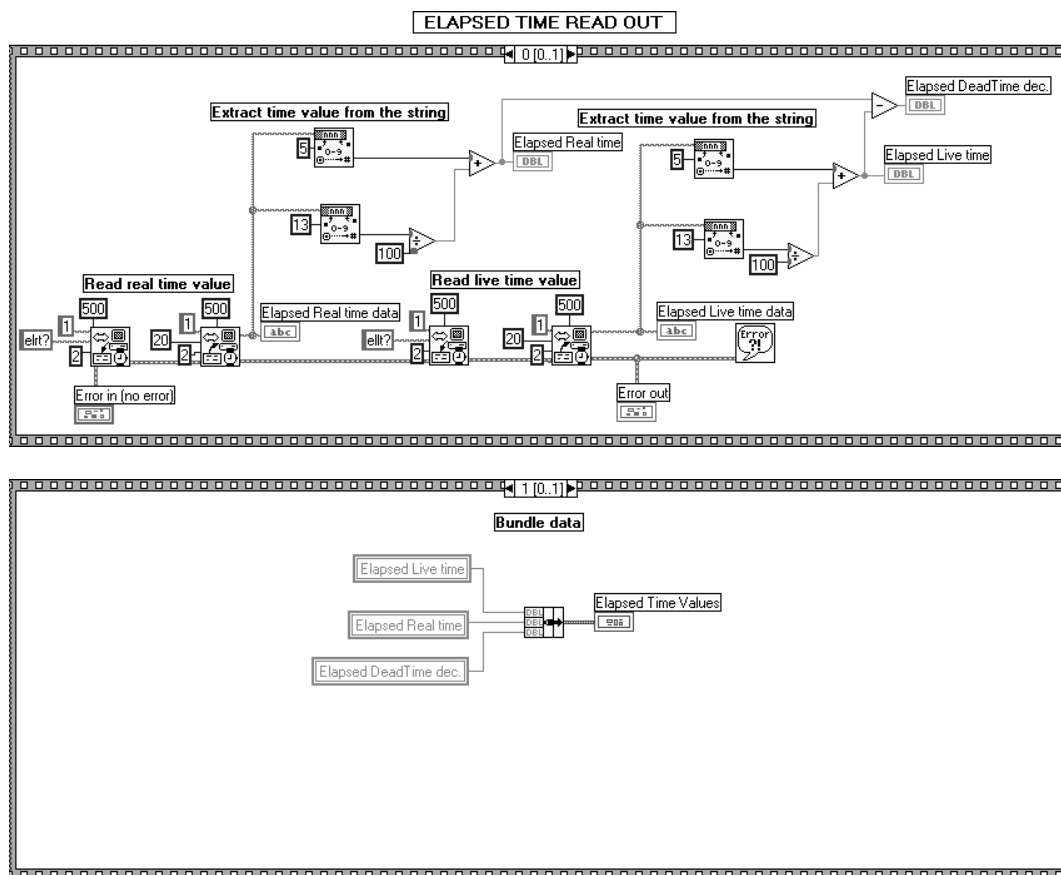
code is the number identifying an error or warning. If status is TRUE, code is a non-zero error code. If status is FALSE, code can be zero or a warning code. Use the error handler VIs to look up the meaning of this code and to display the corresponding error message.

abc **source**

source is a string that indicates the origin of the error, if any. Usually source is the name of the VI in which the error occurred.

EO5 **Elapsed Time Values****DBL** **Live time****DBL** **Real time****DBL** **Dead time**

Block Diagram

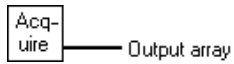


C.14 Acquisition.vi

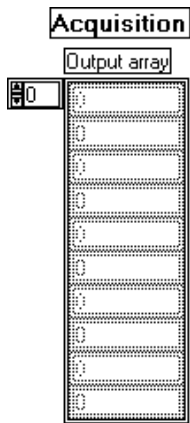
Acquisition.vi

Reads the spectrum data from the PCA.

Connector Pane



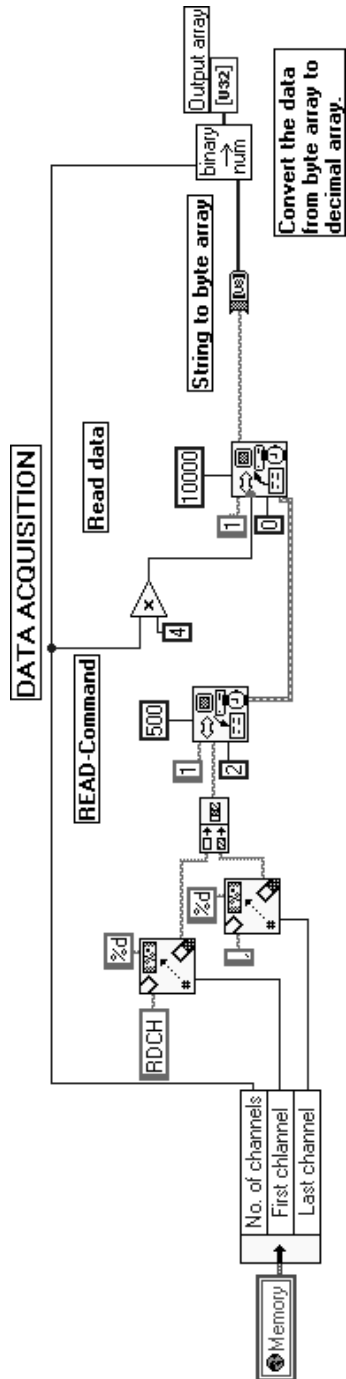
Front Panel



Controls and Indicators



Block Diagram

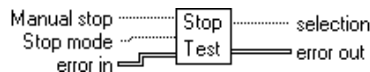


C.15 Stop test.vi

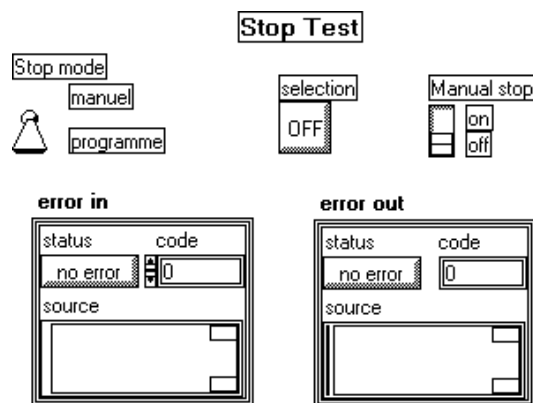
Stop Test.vi

Returns a boolean variable to indicate if data acquisition should stop based on either user request or preset time limits.

Connector Pane



Front Panel



Controls and Indicators

error in

error in is a cluster that describes the error status before this VI executes. If error in indicates that an error occurred before this VI was called, this VI may choose not to execute its function, but just pass the error through to its error out cluster. If no error has occurred, then this VI executes normally and sets its own error status in error out. Use the error handler VIs to look up the error code and to display the corresponding error message. Using error in and error out clusters is a convenient way to check errors and to specify execution order by wiring the error output from one subVI to the error input of the next.

status

status is TRUE if an error occurred before this VI was called, or FALSE if not. If status is TRUE, code is a non-zero error code. If status is FALSE, code can be zero or a warning code.

I32 code

code is the number identifying an error or warning. If status is TRUE, code is a non-zero error code. If status is FALSE, code can be zero or a warning code. Use the error handler VIs to look up the meaning of this code and to display the corresponding error message.

abc source

source is a string that indicates the origin of the error, if any. Usually source is the name of the VI in which the error occurred.

TF Manual stop**TF** Stop mode**FF** error out

error out is a cluster that describes the error status after this VI executes. If an error occurred before this VI was called, error out is the same as error in. Otherwise, error out shows the error, if any, that occurred in this VI. Use the error handler VIs to look up the error code and to display the corresponding error message. Using error in and error out clusters is a convenient way to check errors and to specify execution order by wiring the error output from one subVI to the error input of the next.

TF status

status is TRUE if an error occurred, or FALSE if not. If status is TRUE, code is a non-zero error code. If status is FALSE, code can be zero or a warning code.

I32 code

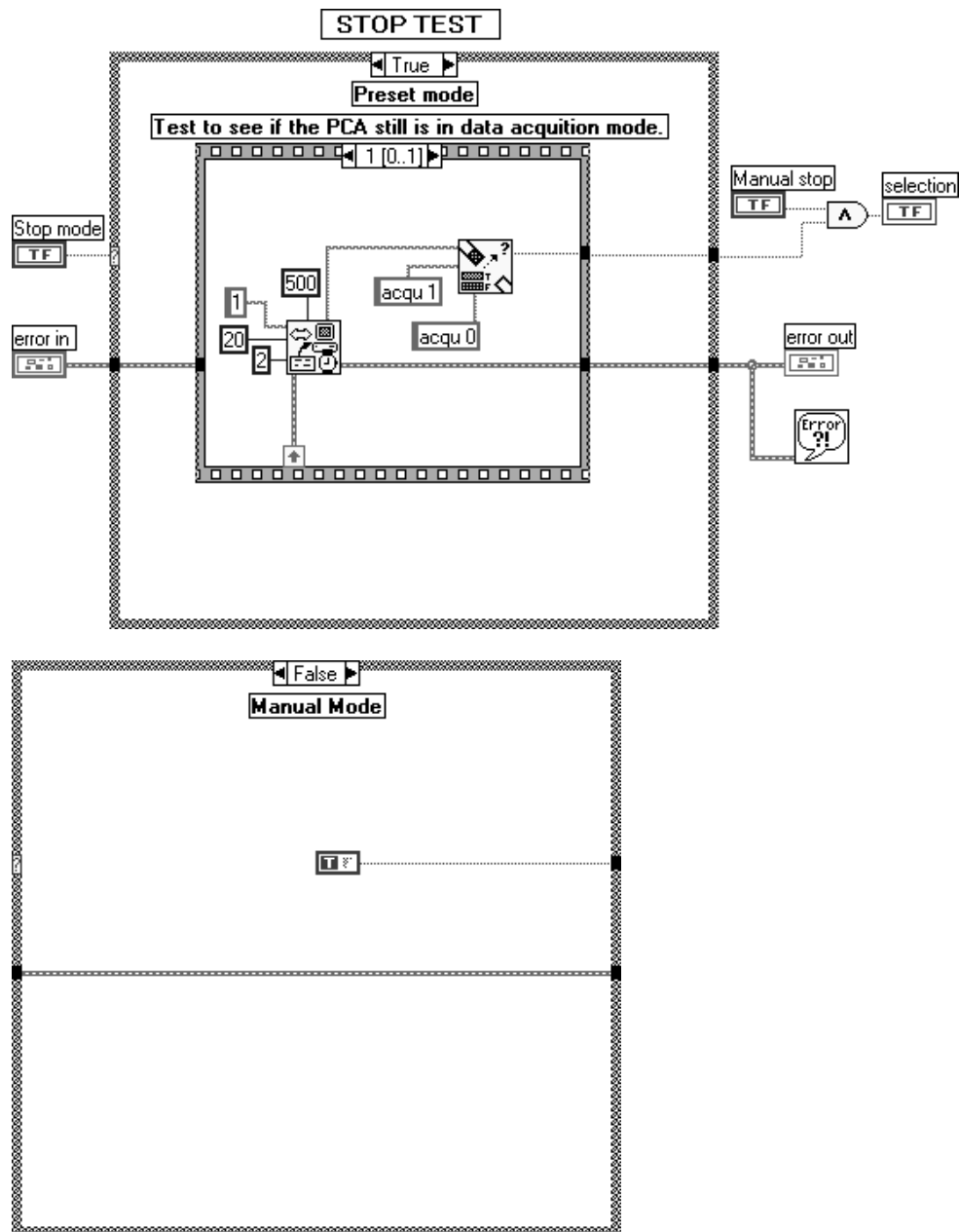
code is the number identifying an error or warning. If status is TRUE, code is a non-zero error code. If status is FALSE, code can be zero or a warning code. Use the error handler VIs to look up the meaning of this code and to display the corresponding error message.

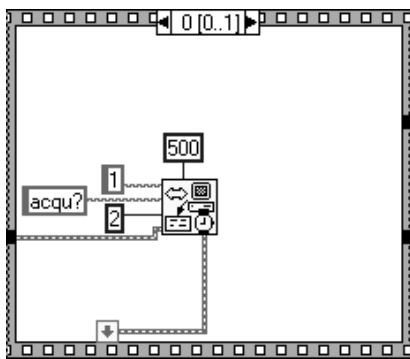
abc source

source is a string that indicates the origin of the error, if any. Usually source is the name of the VI in which the error occurred.

TF selection

Block Diagram



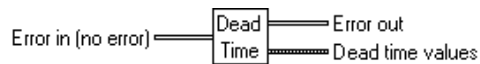


C.16 Dead time.vi

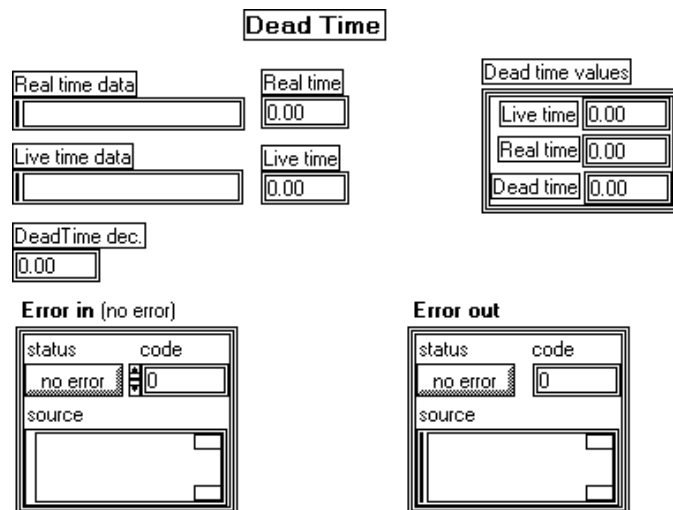
Dead Time.vi

Reads real and live time data from the PCA and calculates the dead time.

Connector Pane



Front Panel



Controls and Indicators

Error in (no error)

error in is a cluster that describes the error status before this VI executes. If error in indicates that an error occurred before this VI was called, this VI may choose not to execute its function, but just pass the error through to its error out cluster. If no error has occurred, then this VI executes normally and sets its own error status in error out. Use the error handler VIs to look up the error code and to display the corresponding error message. Using error in and error out clusters is a convenient way to check errors and to specify execution order by wiring the error output from one subVI to the error input of the next.

status

status is TRUE if an error occurred before this VI was called. or FALSE if not.

If status is TRUE, code is a non-zero error code. If status is FALSE, code can be zero or a warning code.

I32 code

code is the number identifying an error or warning. If status is TRUE, code is a non-zero error code. If status is FALSE, code can be zero or a warning code. Use the error handler VIs to look up the meaning of this code and to display the corresponding error message.

abc source

source is a string that indicates the origin of the error, if any. Usually source is the name of the VI in which the error occurred.

abc Real time data**abc** Live time data**DBL** Real time**DBL** Live time**DBL** DeadTime dec.**☐** Error out

error out is a cluster that describes the error status after this VI executes. If an error occurred before this VI was called, error out is the same as error in. Otherwise, error out shows the error, if any, that occurred in this VI. Use the error handler VIs to look up the error code and to display the corresponding error message. Using error in and error out clusters is a convenient way to check errors and to specify execution order by wiring the error output from one subVI to the error input of the next.

TF status

status is TRUE if an error occurred, or FALSE if not. If status is TRUE, code is a non-zero error code. If status is FALSE, code can be zero or a warning code.

I32 code

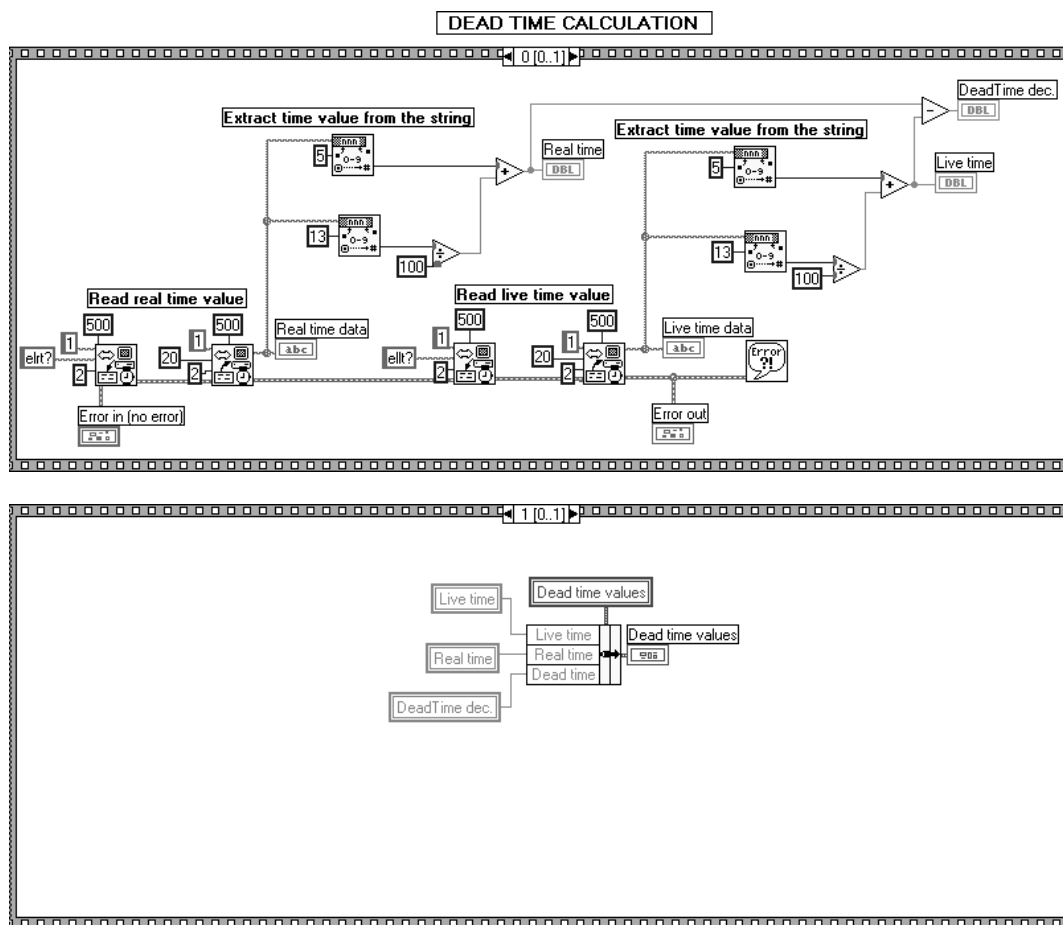
code is the number identifying an error or warning. If status is TRUE, code is a non-zero error code. If status is FALSE, code can be zero or a warning code. Use the error handler VIs to look up the meaning of this code and to display the corresponding error message.

abc source

source is a string that indicates the origin of the error, if any. Usually source is the name of the VI in which the error occurred.

☐ Dead time values**DBL** Live time**DBL** Real time**DBL** Dead time

Block Diagram



Appendix D

Radiation sources

D.1 ²⁴¹Am gamma sources

D.1.1 Disk source

Americium-241

γ and primary X-ray sources

Disc sources, stainless steel window

Americium-241 incorporated in a ceramic enamel sealed in a welded stainless steel capsule.

Sources codes AMC 62-66 are designed for backscatter applications, the active ceramic is recessed into a tungsten alloy insert.

Nominal content activity*	Capsule		Typical photon output in photons/sec per steradian 59.5keV	Code
	MBq	mCi		
37	1	X.10/2	8×10^5	AMC.62
111	3	X.10/2	2.5×10^6	AMC.63
370	10	X.10/2	8×10^6	AMC.64
1110	30	X.11	2.4×10^7	AMC.65
3700	100	X.11/1	5.3×10^7	AMC.66

*Tolerance ± 10%

Recommended working life: 15 years

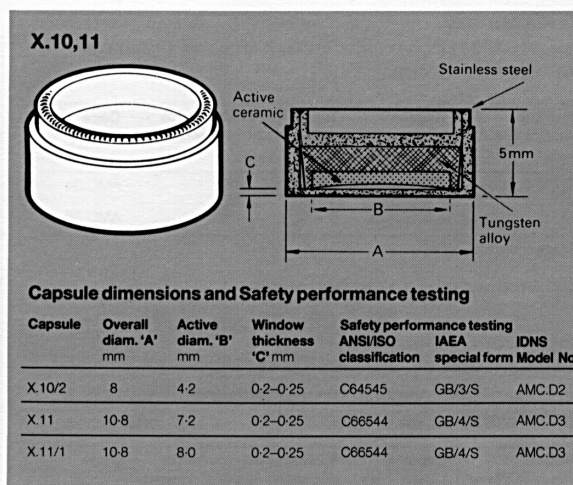


Figure D.1 ²⁴¹Am disk source data sheet. The AMC.65 disk source was used in this study.

D.1.2 Point source

Americium-241

γ and primary X-ray sources

Point sources

Americium-241 incorporated in a ceramic bead (AMC.21 to AMC.25) or cylindrical ceramic pellet (AMC.10236 and AMC.26), sealed in a welded stainless steel capsule.

Nominal content activity*	Capsule		Typical photon output in photons/sec per steradian 59.5keV	Code
	MBq	mCi		
74	2	X.100	1×10^6	AMC.21
518	14	X.101	7×10^6	AMC.24
1665	45	X.102	1.8×10^7	AMC.25
3700	100	X.102	2.2×10^7	AMC.10236
7400	200	X.108	5.5×10^7	AMC.26

* + 15%, - 10%

Recommended working life: 15 years

Quality Control

Wipe test A
Bubble test D
Immersion test L

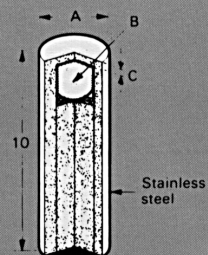
Photon emission and spectral purity checked using Si(Li) and Ge(Li) detectors.

Neutron emission

All Americium-241 sources emit $\sim 10^4$ n/sec per Ci due to (α , n) reactions with the low atomic number elements (for example, Si, Al, O) in the active material.

The use of beryllium windows does not increase this emission significantly.

X.100-102,108



Capsule dimensions and Safety performance testing

Capsule	Overall diam. 'A' mm	Active diam. 'B' mm	Window thickness 'C' mm	Safety performance testing		
				ANSI/ISO classification	IAEA special form	IDNS Model No.
X.100	2	1	0.2-0.25	C64444	GB/55/S	AMC.21
X.101	3	2	0.2-0.25	C64444	GB/56/S	AMC.24
X.102	4	3	0.2-0.25	C64444	GB/59/S	AMC.25/ AMC.P1
X.108	7	5	0.2-0.3	C64444	GB/167/S	AMC.26

Figure D.2 ^{241}Am point source data sheet. The AMC.24 point source was used in this study.